

ALTERNATING CURRENT THIN FILM ELECTROLUMINESCENCE IN THE  
NEAR INFRARED FROM ZINC SULFIDE DOPED WITH RARE EARTHS

By

AJAY KALE

A DISSERTATION PRESENTED TO THE GRADUATE SCHOOL  
OF THE UNIVERSITY OF FLORIDA IN PARTIAL FULFILLMENT  
OF THE REQUIREMENTS FOR THE DEGREE OF  
DOCTOR OF PHILOSOPHY

UNIVERSITY OF FLORIDA

2003

Copyright 2003

by

Ajay Kale

Dedicated to my parents

## ACKNOWLEDGMENTS

It would be impossible to thank all the people who have helped me both personally and with this work. However here are a few people to whom I owe my gratitude, and without their tremendous support, I could not have made this journey.

First of all I would like to thank my advisor, Dr. Paul Holloway. A lot of what I learned these past four years, not just academically but as a person, I owe to Dr. Holloway. His dedication to his work and more importantly to his students and his knowledge of science is truly unique. He was also a great source of motivation and I am lucky to have him as my mentor.

I would like to thank Dr. Nigel Shepherd, who always gave me advice and encouragement when I needed it the most. It was a pleasure to work with him not only as a research colleague but also as a really good friend. I would also like to thank Dr. Mark Davidson and Barbara at Microfabritech for their help, when I had difficulties with my research. Of course I could not forget Ludie, who has the best smile and taught me to be ever cheerful. I also appreciate all the members of Dr. Holloway's group (Bill and Dave in particular, Phil, Narada, Hannah, Jaehyun, Joohan, Heesun, Joonbo, Jie, Rob, etc.) for their help and warm friendship.

I would like to thank my father, mother and brother (Sachin), who always believed in me and have always been my biggest supporters.

Finally, I would like to thank my beautiful wife Ruta for always being on my side when I needed her the most, and I cannot express in words how much I love and care for

her. Her support for me has been tremendous and I could not possibly have been the person I am without her on my side.

## TABLE OF CONTENTS

	<u>page</u>
ACKNOWLEDGMENTS .....	iv
LIST OF TABLES .....	ix
LIST OF FIGURES .....	x
ABSTRACT .....	xiv
<b>CHAPTER</b>	
1 INTRODUCTION .....	1
2 LITERATURE REVIEW .....	3
2.1 Introduction.....	3
2.2 History of Electroluminescence.....	4
2.3 ACTFEL Device Structures.....	9
2.3.1 Monochrome Structures .....	9
2.3.2 Full Color Displays.....	11
2.4 ACTFEL Device Physics.....	14
2.4.1 Tunnel Injection.....	16
2.4.2 High Field Charge Transport.....	17
2.4.3 Impact Excitation/Ionization .....	20
2.4.4 Radiative Decay.....	21
2.4.5 Optical Outcoupling .....	22
2.5 ACTFELD Materials .....	23
2.5.1 Substrate Materials .....	24
2.5.2 Transparent Electrodes .....	25
2.5.3 Opaque Electrodes.....	26
2.5.4 Insulator Materials.....	27
2.5.5 Phosphor Layer.....	30
2.5.5.1 Host material (matrix) .....	30
2.5.5.2 Luminescent centers.....	32
2.5.5.3 Luminescent-center host-lattice systems.....	36
2.6 ACTFEL Device Characterization .....	38
2.6.1 Optical Characteristics.....	38
2.6.1.1 Luminance-voltage.....	40
2.6.1.2 CIE color coordinate scheme .....	43
2.6.2 Electrical Characteristics .....	44

2.6.2.1	Equivalent circuit models of ACTFEL devices .....	44
2.6.2.2	Electrical characterization .....	48
2.7	ZnS:NdF <sub>3</sub> and ZnS:ErF <sub>3</sub> as ACTFEL phosphors .....	56
3	EXPERIMENTAL PROCEDURE .....	60
3.1	Introduction.....	60
3.2	ACTFEL Device Fabrication.....	60
3.2.1	Substrate Materials .....	60
3.2.2	Thin Film Deposition .....	60
3.2.3	Post-Deposition Annealing.....	62
3.2.4	Electrode Deposition .....	63
3.3	Characterization.....	64
3.3.1	Thickness Measurement .....	64
3.3.2	Electroluminescence (EL) Measurement [46].....	64
3.3.3	Photoluminescence (PL) Measurement [112] .....	66
3.3.4	X-ray Diffraction (XRD).....	66
3.3.5	Transmission Electron Microscopy (TEM).....	67
3.3.6	Atomic Force Microscopy (AFM).....	69
3.3.7	Electron Probe Micro Analysis (EPMA).....	70
3.3.8	Electrical Characterization .....	71
4	RF MAGNETRON SPUTTER DEPOSITION OF ZINC SULFIDE DOPED WITH NEODYMIUM ACTFEL DEVICES.....	73
4.1	Introduction.....	73
4.2	ACTFEL Device Efficiency .....	73
4.2.1	Optical Outcoupling Efficiency.....	75
4.2.2	Excitation and Radiative Efficiency .....	76
4.3	The Amount of Conduction Charge .....	77
4.4	Experimental Procedure.....	77
4.4.1	Substrate Materials .....	78
4.4.2	Phosphor Layer Deposition .....	78
4.4.3	Device Completion.....	80
4.5	Results.....	80
4.5.1	Chemical and Structural Characterization.....	80
4.5.1.1	Thin film concentration.....	80
4.5.1.2	X-ray diffraction (XRD).....	81
4.5.1.3	Atomic force microscopy (AFM).....	82
4.5.1.4	Transmission electron microscopy (TEM).....	83
4.5.2	Optical Characterization.....	84
4.5.2.1	Brightness-voltage (B-V) plots .....	84
4.5.2.2	The effect of annealing on infrared electroluminescence of ZnS:NdF <sub>3</sub> thin film devices .....	87
4.5.2.3	Luminescence decay characterization (room temperature).....	90
4.5.3	Electrical Characterization .....	98
4.6	Summary.....	104

5	RF MAGNETRON SPUTTER DEPOSITION OF ZINC SULFIDE DOPED WITH ERBIUM ACTFEL DEVICES .....	106
5.1	Introduction.....	106
5.2	Experimental Procedure.....	106
5.2.1	Substrate Materials .....	107
5.2.2	Deposition of Phosphor Layer.....	107
5.2.3	Device Completion.....	109
5.3	Experimental Results .....	109
5.3.1	Structural and Chemical Characterization.....	109
5.3.1.1	Thin film concentration.....	109
5.3.1.2	X-ray diffraction (XRD).....	110
5.3.1.3	Atomic force microscopy (AFM).....	111
5.3.2	Optical Characterization.....	112
5.3.2.1	Brightness-voltage (B-V) plots .....	112
5.3.2.2	Effect of annealing on infrared electroluminescence of ZnS:ErF <sub>3</sub> thin film devices.....	114
5.3.2.3	Photoluminescence (PL) characterization (room temperature).....	116
5.3.2.4	Luminescence decay characterization (room temperature).....	119
5.3.3	Electrical Characterization .....	126
5.4	Summary of Results.....	131
6	DISCUSSIONS.....	133
6.1	Neodymium Fluoride (NdF <sub>3</sub> ) Doped Zinc Sulfide ACTFEL Devices .....	134
6.1.1	Wavelength Dependence with Temperature .....	134
6.1.2	Brightness and Efficiency Improvement with Annealing .....	135
6.1.2.1	Outcoupling efficiency.....	136
6.1.2.2	Radiative efficiency.....	137
6.1.2.3	Excitation efficiency .....	137
6.2	Erbium Fluoride (ErF <sub>3</sub> ) Doped Zinc Sulfide ACTFEL Devices .....	140
6.2.1	Wavelength Independence of Temperature.....	140
6.2.2	Brightness and Efficiency Improvement with Annealing .....	140
6.2.2.1	Outcoupling efficiency.....	141
6.2.2.2	Radiative efficiency.....	142
6.2.2.3	Excitation efficiency .....	142
7	CONCLUSIONS .....	145
	LIST OF REFERENCES.....	148
	BIOGRAPHICAL SKETCH .....	155

## LIST OF TABLES

<u>Table</u>		<u>page</u>
2.1	The development high-field electroluminescence in ZnS [11].	7
2.2	Typical insulator materials with relative dielectric constant, dielectric breakdown field, figure of merit, breakdown mode and deposition technique.	30
2.3	Properties of some common ACTFEL host compounds [11].	31
2.4	List of valence and ionic radius for cations commonly used in ACTFEL hosts, a well as common dopant ions [90].	37
2.5	Comparison of the visible characteristics of ZnS electroluminescent phosphors.	38
2.6	Relative luminosity as a function of wavelength	40
6.1	External and internal conduction charge versus voltage at $V_{40}$ for as deposited and annealed ZnS:NdF <sub>3</sub> thin films.	139
6.2	External and internal conduction charge versus voltage at $V_{40}$ for as deposited and annealed ZnS:ErF <sub>3</sub> thin films.	143

## LIST OF FIGURES

<u>Figure</u>	<u>page</u>
2.1	Schematic cross-section of (a) the standard double insulator structure, (b) inverted structure and (c) half-stack structure.....11
2.2	Schematic of conventional ACTFEL device.[11].....12
2.3	Hybrid stacked-substrate structure.....13
2.4	“Color-by-white” device structure [3]. .....14
2.5	Energy band diagram of ACTFEL device and schematic illustrations of the EL emission mechanism. ....15
2.6	Electron energy distribution as a function of energy for different phosphor fields using the nonparabolic band structure model [55].....19
2.7	Electron energy distribution as a function of energy for different phosphor fields using the full-band structure model [55].....19
2.8	Schematic representation of internal reflection in a ZnS:Mn ACTFEL device [11]. .....23
2.9	Transmission spectrum of 7059 glass [63]. .....24
2.10	The relative energy levels of the atomic orbitals in multi-electron atoms [82].. .....34
2.11	Schematic diagram of a RE <sup>+3</sup> ion showing the radial position of the outer orbitals.. .....34
2.12	Energy level scheme for different rare earths [84, 85]. .....35
2.13	Schematic illustration of V <sub>th</sub> and B <sub>40</sub> for brightness vs. voltage data. ....41
2.14	The <i>Commission Internationale de ‘Eclairage (CIE)</i> color coordinate system.....45
2.15	Equivalent circuit of an ACTFEL device [75].....46

2.16	Schematic diagram of circuit used to measure conduction current using a Sawyer-Tower bridge [46].	49
2.17	Schematic diagram of the voltage waveform used in ACTFEL device operation and characterization.	50
2.18	Schematic diagram of the Q-V characteristics of an ACTFEL device.	52
2.19	Schematic diagram of an idealized $Q_{\text{int}}-F_p$ plot.	54
2.20	Schematic diagram of a C-V plot for three different values of $V_{\text{max}}$ .	56
2.21	Schematic diagram of $Q_{\text{max}}-V_{\text{max}}$ plot for an ideal device.	56
2.22	Spectrum of ZnS:NdF <sub>3</sub> [30].	57
2.23	Spectrum of ZnS:ErF <sub>3</sub> [30].	59
3.1	Schematic of the sputtering system used for RF planar magnetron deposition of ZnS:Er/NdF <sub>3</sub> thin films.	62
3.2	Schematic of the “rapid thermal anneal” furnace showing lamps as heaters.	63
3.3	Typical commercial ACTFEL device driving waveform.	65
3.4	Optical bench setup for measuring EL and PL from ACTFEL.	65
3.5	XTEM sample preparation technique.	69
3.6	Schematic of an Atomic Force Microscope.	70
4.1	Schematic process flow diagram for ZnS:NdF <sub>3</sub> device fabrication.	78
4.2	Effect of annealing temperature on the FWHM of the 28.5° X-ray diffraction peak from the ZnS:NdF <sub>3</sub> film.	82
4.3	AFM surface morphologies of a) as-deposited and b) annealed at 425°C for 1 hr ZnS:NdF <sub>3</sub> thin films.	83
4.4	XTEM micrographs for ZnS:NdF <sub>3</sub> thin films.	86
4.5	Brightness vs. voltage behavior as a function of annealing treatment.	86
4.6	Diffuse reflectance values for as-deposited and annealed (425°C for 1 hr) ZnS:NdF <sub>3</sub> films.	87
4.7	Effect of annealing on the IR EL emission from ZnS:NdF <sub>3</sub> thin films.	89

4.8	Luminescence decay data measurement setup for ZnS:NdF <sub>3</sub> thin films. ....	92
4.9	Luminescence decay behavior for as deposited ZnS:NdF <sub>3</sub> thin film operated at V <sub>40</sub> , 2.5kHz frequency, 5μs pulse width. ....	93
4.10	Time resolved luminescence decay data for ZnS:NdF <sub>3</sub> as deposited thin film. ....	95
4.11	Luminescence decay behavior for annealed ZnS:NdF <sub>3</sub> thin film operated at V <sub>40</sub> , 2.5kHz frequency, 5μs pulse width. ....	96
4.12	Time resolved luminescence decay data for ZnS:NdF <sub>3</sub> annealed thin film. ....	98
4.13	External charge (Q <sub>ext</sub> ) versus applied voltage (V <sub>EL</sub> ) for Al (+) and Al (-) polarities at 40V above threshold for ZnS:NdF <sub>3</sub> thin film samples. ....	99
4.14	Capacitance (C) versus applied voltage (V <sub>EL</sub> ) for Al (+) polarity at 40V above threshold for ZnS:NdF <sub>3</sub> thin film samples. ....	100
4.15	Internal charge (Q <sub>int</sub> ) versus phosphor field (F <sub>p</sub> ) for Al (+) and Al (-) polarities at 40V above threshold for ZnS:NdF <sub>3</sub> thin film samples. ....	101
4.16	Determination of B <sub>max</sub> from L(t) data. Note the necessary extrapolation back to the end of the voltage pulse. ....	102
4.17	Excitation efficiency, (B <sub>max</sub> /Q <sub>int</sub> ) versus voltage plots. ....	103
5.1	Schematic process flow diagram for ZnS:ErF <sub>3</sub> device fabrication. ....	107
5.2	Effect of annealing temperature on the FWHM of the 28.5° X-ray diffraction peak from the ZnS:ErF <sub>3</sub> film. ....	110
5.3	AFM surface morphologies of a) as-deposited and b) annealed at 425°C for 1 hr ZnS:ErF <sub>3</sub> thin films. ....	111
5.4	Brightness vs. voltage behavior as a function of annealing treatment. ....	113
5.5	Diffuse reflectance values for as-deposited and annealed (425°C for 1 hr) ZnS:ErF <sub>3</sub> films. ....	113
5.6	Effect of annealing on the IR EL emission from ZnS:ErF <sub>3</sub> thin films. ....	115
5.7	Visible PL/PLE spectrum for annealed ZnS:ErF <sub>3</sub> thin film (a) PLE spectrum, and (b) PL spectrum. ....	117
5.8	Infrared PL/PLE spectrum for annealed ZnS:ErF <sub>3</sub> thin film (a) PLE spectrum, and (b) PL spectrum. ....	118

5.9	Luminescence decay behavior for as deposited ZnS:ErF <sub>3</sub> thin film operated at V <sub>40</sub> , 2.5kHz frequency, 5μs pulse width. ....	121
5.10	Time resolved luminescence decay data for ZnS:ErF <sub>3</sub> as deposited thin film.....	123
5.11	Luminescence decay behavior for annealed ZnS:ErF <sub>3</sub> thin film operated at V <sub>40</sub> , 2.5kHz frequency, 5μs pulse width. ....	124
5.12	Time resolved luminescence decay data for ZnS:ErF <sub>3</sub> annealed thin film.....	126
5.13	External charge (Q <sub>ext</sub> ) versus applied voltage (V <sub>EL</sub> ) for Al (+) and Al (-) polarities at 40V above threshold for ZnS:ErF <sub>3</sub> thin film samples.....	127
5.14	Capacitance (C) versus applied voltage (V <sub>EL</sub> ) for Al (+) polarity at 40V above threshold for ZnS:ErF <sub>3</sub> thin film samples. ....	128
5.15	Internal charge (Q <sub>int</sub> ) versus phosphor field (F <sub>p</sub> ) for Al (+) and Al (-) polarities at 40V above threshold for ZnS:ErF <sub>3</sub> thin film samples.....	129
5.16	Excitation efficiency, (B <sub>max</sub> /Q <sub>int</sub> ) versus voltage for the a) visible transition (545nm) and b) near infrared transition (1550nm). ....	130

Abstract of Dissertation Presented to the Graduate School  
of the University of Florida in Partial Fulfillment of the  
Requirements for the Degree of Doctor of Philosophy

ALTERNATING CURRENT THIN FILM ELECTROLUMINESCENCE IN THE  
NEAR INFRARED FROM ZINC SULFIDE DOPED WITH RARE EARTHS

By

Ajay Kale

December 2003

Chair: Dr. Paul H. Holloway

Major Department: Materials Science and Engineering

Near infrared emission (0.7-1.5  $\mu\text{m}$ ) of zinc sulfide (ZnS) doped with erbium (Er) or neodymium (Nd) has been studied in alternating current thin film electroluminescent devices (ACTFELDs). The electroluminescent (EL) thin film phosphors were radio frequency planar magnetron sputter deposited by co-sputtering an undoped ZnS target together with a ZnS: 1.5 mole%  $\text{ErF}_3$  or ZnS: 1.5 mole%  $\text{NdF}_3$  target. The ZnS: $\text{ErF}_3$  and ZnS: $\text{NdF}_3$  thin film phosphors were annealed for one hour in ultra high purity  $\text{N}_2$  at temperatures ranging from 350-475°C. Annealing at 425°C for 1 hour in nitrogen was the optimal post-deposition treatment for both the ZnS: $\text{ErF}_3$ , and ZnS: $\text{NdF}_3$  thin film phosphors, resulting in EL power densities of 7.5 and 28  $\mu\text{W}/\text{cm}^2$  for the 990nm and the 1550nm emission of ZnS: $\text{ErF}_3$ , respectively. The power densities were 7.5 (750%) and 28 (2800%) times larger than those from the as-deposited films, which exhibited a power density  $\sim 1\mu\text{W}/\text{cm}^2$  at both wavelengths. In the case of ZnS: $\text{NdF}_3$ , 26 and 15  $\mu\text{W}/\text{cm}^2$  was achieved at 910nm and at 1060nm, which was only 2 (100%) times larger than from as-

deposited samples. Post-deposition annealing resulted in a 8 and 1.5 times increase in total device efficiency to 0.42 W/W and 0.7 W/W) for ZnS:ErF<sub>3</sub> and ZnS:NdF<sub>3</sub>, respectively. This was attributed to a reduction in the concentration of shallow defects, which leads to a larger effective phosphor field and band bending, an increase in the conduction charge, and a reduction of inelastic scattering of ballistic electrons. While the peak emission wavelengths from Er were independent of annealing temperature, peak shifts were observed for Nd due to hybridization of the 5d-4f orbitals. At annealing temperatures <425°C, the density of shallow traps is high, and electrons from higher energy excited states of the luminescent ions to shallow, non-radiative defect levels pump the lower energy IR states. For annealing temperatures > 425°C, the shallow defect states are annealed out, leading to more efficient direct radiative relaxation from the higher lying excited states, and more intense visible luminescence is observed.

## CHAPTER 1 INTRODUCTION

Thin film electroluminescent display devices have been investigated for flat panel displays and visible light emitting displays like ZnS:Mn are commercially available [1-6]. While a lot of work has been done in the visible emission ACTEFEL displays, the infrared emission region has often been ignored. Infrared phosphors obviously do not have the marketability of their visible counterparts, but they have applications that are of considerable interest. Infrared emitters (IR) enjoy a wide market today with a variety of applications like commercial fiber optic based communication devices, night vision, friend/foe identification, industrial gas sensors and remote controls for televisions.

In this study ZnS doped rare earth fluoride thin films (namely NdF<sub>3</sub> and ErF<sub>3</sub>) in the conventional metal-insulator-semiconductor-insulator-metal (M-I-S-I-M) configuration are studied as a new source for IR radiation (namely the 1060nm transition in Nd and the 1550nm transition in Er).

Chapter 2 will present a background and literature review of ACTFEL devices. In chapter 3, the experimental methods characterization methods used for device study will be outlined. Chapter 4 will focus on ZnS:NdF<sub>3</sub> ACTFEL device fabrication and modification and various electro-optical characterization techniques will be presented. Chapter 5 will highlight ZnS:ErF<sub>3</sub> ACTFEL devices and similar device modification and characterization techniques will be displayed. Chapter 6 will support the results obtained in the preceding chapters and will provide detailed discussions to explain the various

trends that are observed in NdF<sub>3</sub> and ErF<sub>3</sub> doped devices. Finally, the conclusions will be presented in chapter 7.

## CHAPTER 2 LITERATURE REVIEW

### 2.1 Introduction

The term flat panel displays encompasses all the non-cathodo ray tube (CRT) direct-view-displays. The flat-panel-display (FPD) market is flourishing due to increased demand for portable computers, consumer electronic products and communication equipment. In all of these applications, the display is the integral and primary human interface that conveys the information. The flat-panel-displays can further be divided into liquid crystal displays (LCD) and emissive displays. LCDs hold almost 85% of market for small flat panel displays (<14") [7]. In demanding applications like the military environment, medical instruments and vehicles, the weaknesses of LCDs are severe, viz. small viewing angle, limited operation temperature, relatively low brightness and sensitivity for constant movement [8]. Hence considerable effort has been taken for the development of emissive flat panels, which incorporate longer lifetimes and ruggedness. Alternating current thin films electroluminescent displays (ACTFEL displays) have become the most reliable and longest lasting devices on today's market [3, 5, 9] and are solid-state analogs to cathodoluminescent vacuum tubes (CRT). Displays ranging from full-color, VGA down to headsets the size of a postage stamp have been produced [10]. Currently, thin film EL displays are the longest lasting, most reliable flat panel display technology available on the market. Display panels with lifetimes of over 50000h with less than 10% luminance change have been demonstrated [3, 10].

While a review is given here of electroluminescent materials and processes, several excellent reviews of electroluminescent technology are also available [11-13].

## 2.2 History of Electroluminescence

Electroluminescence is defined as the generation of light by the application of an electric field [11]. The first observations were made by Gudden and Pohl in 1929, where they reported the effect of electrical field on photoluminescence of ZnS:Cu phosphor [14]. In 1936, the French scientist Destriau observed light emission upon application of a high field to a suspension consisting of ZnS:Cu:oil in a device that resembles a modern powder EL cell [15]. His work is cited as the first published report on the phenomenon of electroluminescence. The development of ZnO<sub>2</sub> in 1950 triggered worldwide EL research and development. At the time, these efforts focused mainly on powder phosphors for general lighting applications. Indeed, GTE Sylvania obtained a patent for an ac EL powder lamp in 1952 [12]. However, it was soon realized that so-called cold lamps had very limited lifetimes, which strongly depended on the drive level and light output required [6]. Simply put, they were unable to provide adequate sustained brightness over the minimum (500hr) commercially acceptable lifetimes. As a result, interest in the area diminished.

There was resurgence in EL research in the 1960s and focus was on display technologies. The late 1960s saw rejuvenated interest in EL research and development and though Vecht demonstrated the first dc powder EL panel in 1968 [16], the majority of development efforts focused on thin-film EL. The optically active layer in Vecht's device consisted of ZnS powder particles coated with copper ions, which were then embedded into a binder. In 1968 Kahng [17] employed an ac driven device using Lumocen (luminescence from molecular centers) and proposed that impact excitation of

luminescent centers by hot electrons was the EL emission mechanism. Here the optically active layer consisted of thin-film ZnS doped with rare-earth fluorides (as molecular centers). In the sixties Soxman and Ketchpel [18] also obtained TFEL devices with acceptable lifetimes and multiplexing capabilities, though dependability remained unacceptable. These early successes would not have been realized without the developments in thin-film processing, and advances in materials science and physical electronics that took place in the sixties.

The insulating layer/phosphor/insulating layer sandwich structure first proposed by Russ and Kennedy [19] in 1967 was a major milestone in the development of TFEL display technology, though its benefit was not immediately realized by researchers in the area. Utilizing this double-insulating ac driven thin-film structure with a ZnS:Mn phosphor layer, Inoguchi *et al.* [20] from Sharp Central Research Labs reported stable, high-luminance EL panels which had excellent lifetimes. The work of Inoguchi *et al.* described the basic phenomena and is often cited as the birth of current TFEL technology. Since then, ac thin-film EL devices (ACTFELDs) have been the most intensely investigated devices because they have the highest possibility for successful practical application. As a result of these efforts, TFEL is now one of the three main flat panel display technologies. Uede *et al.* [21] and Takeda *et al.* [22-23] and their coworkers reported on the production of practical EL ZnS:Mn display units in 1981 and in 1983 Sharp introduced the first commercial ZnS:Mn thin-film display [20, 24]. By the mid-80s, ZnS:Mn thin-film displays were also introduced by Planar Systems and Finlux [5], and a variety of EL products began appearing on the market. Zinc sulfide doped with manganese is yellow light emitting. As a result, early thin-film products were

monochrome, yellow emitting. At present, both Sharp and Planar utilize color filtering of red and green from yellow in order to manufacture multicolor displays based on ZnS:Mn. There is also considerable effort toward developing ZnS doped with rare earth ions, thin-film phosphors that emit the three primary colors i.e., red, green and blue for full-color displays [25, 26]. Rare earth doped semiconductors have received world wide attention because of possible applications in optoelectronics. These systems exhibit a temperature dependent luminescence wavelength which is nearly independent of the specific semiconductor host. The continuing interest in rare earth doped semiconductors arises from the prospect of developing novel electroluminescent devices which combine the electronic properties of semiconductors with the unique luminescence features of the rare earth ions [27-29]. Work in this area was pioneered by Kahng [17] and Chase *et al.* [30] in the late sixties. EL phosphors containing rare earth ions have been reviewed by several authors [1, 5, 11, 13, 31-34]. Commercial production of full-color thin film displays began in 1994. These were based on the work by Barrow and his coworkers [35]. They used a stacked structure with the red and green phosphors on one substrate, and blue emitting cerium doped calcium thiogallate phosphor on a separate substrate. The details regarding the physics and structure of this and other EL devices will be addressed in later sections. Table 2.1 provides the major milestones in the development of ZnS based EL.

Table 2.1 The development high-field electroluminescence in ZnS [11].

---

1936	High-field electroluminescence from ZnS discovered by Destriau.
1950	Transparent electrically conductive zinc oxide developed.
1950s	Development and basic studies of ac powder EL devices. GTE Sylvania obtains a patent for powder EL lamp. Problems include low brightness, short lifetimes, poor contrast, and high operating voltage among others. Research and commercial interest eventually fades.
1960	Electroluminescence in thin-film ZnS:Mn described by Vlasenko and Popkov.
1960s	Thin-film EL research by Soxman and Ketchpel. Reported in 1972.
1967	Breakthrough double-insulating-layer ac thin-film device structure proposed by Russ and Kennedy.
1968	Pioneering work by Kahng reported high luminance EL from ZnS:TbF <sub>3</sub> thin-film phosphors, and described impact excitation. He called it luminescence from molecular centers (Lumocen).
1968	Vecht demonstrates the first dc-driven powder EL panel.
1974	Inoguchi and his coworkers reports first ZnS:Mn high-luminance, long-lifetime ac thin-film EL panels. Device structure was proposed earlier by Russ and Kennedy.
1974	Mito <i>et al.</i> showed that thin-film EL panels could be used as a TV imaging system.
1981	Uede, Takeda and their coworkers reported on the production of practical ZnS:Mn ac thin-film EL display units.
1983	Sharp introduces the first commercial ZnS:Mn ac thin-film monochrome display.
1988	Prototype full-color thin-film EL display demonstrated by Barrow and coworkers.
1990s	Alternating-current powder EL devices developed for specialty lighting.
1993	First commercial multicolor (red/green/yellow) ZnS:Mn ac thin-film EL display introduced by Cramer <i>et al.</i>
1994	First commercial full-color ac thin-film EL display panel.

---

Today ZnS and other EL phosphors continue to be extensively researched. Most of this effort is geared toward developing more efficient full-color (red, green, blue) ac thin-film EL displays. Advances in TFEL technology is occurring rapidly due to an increasing knowledge base coupled with the interplay of developments in materials, deposition techniques and device structures.

While a lot of work has been done in the visible emission ACTEFEL displays, the infrared emission region has often been ignored. Infrared phosphors obviously do not have the marketability of their visible counterparts, but they have applications that are of

considerable interest. The industry can use these devices for absorption based gas sensing [36] as well as developing night vision equipment like helmet mounted cameras or goggles for friend/foe identification. They also find applications in transmitting signals for fiber optic communication and handheld remote controls in consumer electronics. There are several sources of infrared light other than thin film devices, namely light emitting diodes (LEDs), lasers, and thermal emitters. Infrared LEDs are the analog of the common visible light LEDs. One of the possible drawbacks with LEDs is that they are limited to a fairly large size compared to the possible pixel size of an EL thin film. Rare earth phosphors can be used in LEDs by depositing the phosphor on a blue emitting semiconductor chip and using the blue light to photo-excite the phosphor. A major drawback of such a design is a loss of efficiency [37]. Gas sensors need stable light sources to function properly. Infrared lasers can have problems with long-term stability due to amplitude variations when wavelength modulated [38]; also they are unstable at temperatures above 150°C. Thermal (globars) emitters are similar to the filament of an incandescent light bulb or heating rods in your kitchen ovens. The main differences are the material used and the temperature of the glower. Globars are silicon carbide bars that are heated to a desired temperature. The emission of the globar approximates that of a blackbody at the same temperature [39]. Two of the drawbacks of thermal emitters are that they must be heated to elevated temperatures and they do not emit at distinct wavelengths but instead over a wide spectrum. Owing to the drawbacks of these IR light sources, ACTFELDs promise to make a huge impact in IR light emitting devices.

## 2.3 ACTFEL Device Structures

### 2.3.1 Monochrome Structures

The most common structure used for ACTFEL devices is known as the “standard,” MISIM (metal-insulator-semiconductor-insulator-metal), or “full stack” structure [31], shown schematically in Figure 2.1(a). This device uses a transparent substrate, normally glass, and a transparent bottom electrode that is deposited onto the glass. This is followed by deposition of a transparent insulator, the phosphor layer, a second insulator, and finally an opaque electrode. Light is transmitted through the glass in the direction of the viewer. The rear electrode can be made reflective to increase the brightness of the device, and a dark layer can be used behind the phosphor to enhance contrast. This type of structure has several advantages. It allows the use of glass substrates, which are inexpensive and widely available in most sizes. It also allows for “self-healing” of pinhole defects when aluminum is used with a proper top insulator. “Self healing” means that when microscopic shorts occur in the phosphor they do not propagate and lead to a catastrophic breakdown. Instead, the breakdown failure is limited to a localized region due to the rapid fusing of the aluminum electrode film by the sudden current flow to a short circuit.

Another common device structure is known as the “inverted” structure, because in this case the substrate is normally (but not necessarily) opaque and the top insulator transparent [11, 40]. This structure allows use of opaque substrates as is the case in active matrix EL devices and thick film dielectric hybrid EL devices [41, 42]. The light leaves the top of the device toward the viewer. In this structure (Figure 2.1(b)) the substrate acts as both the support structure and the dielectric layer [43]. In this case the substrate is normally a high dielectric constant material such as BaTiO<sub>3</sub>. The bottom electrode is

deposited on the opposite side of the substrate as the phosphor, and thus the substrate is part of the device.

The inverted structure has several advantages relative to the standard structure shown in Figure 2.1(a). Without the requirement for a transparent substrate, a substrate material such as a ceramic may be chosen that allows higher temperature processing than does a glass substrate. This is often beneficial in optimizing the microstructure and subsequent performance of the phosphor layer. Another benefit of the inverted structure involves full or multi-color display applications when filters are used. Simple organic filters may be added after any high temperature processing steps, as opposed to the standard structure which requires that the filters be deposited before the phosphor layer. One of the drawbacks of the inverted structure is the loss of the self-healing failure mechanism exhibited by Al contacts, since a transparent conductor must be used as the top electrode, rather than a metal.

The final type of device, shown in Figure 2.1(c), is normally used only for device testing. This device is known as the “half stack” structure. This type of device can be similar to either the standard or the inverted structure, but lacks one of the two insulating layers. Normally it lacks the top insulator, which saves an additional processing step. This type of structure has the advantage of ease of processing and therefore more rapid results. However it normally has poorer performance in terms of brightness and stability than the dual insulating structures, and is primarily used for research purposes.

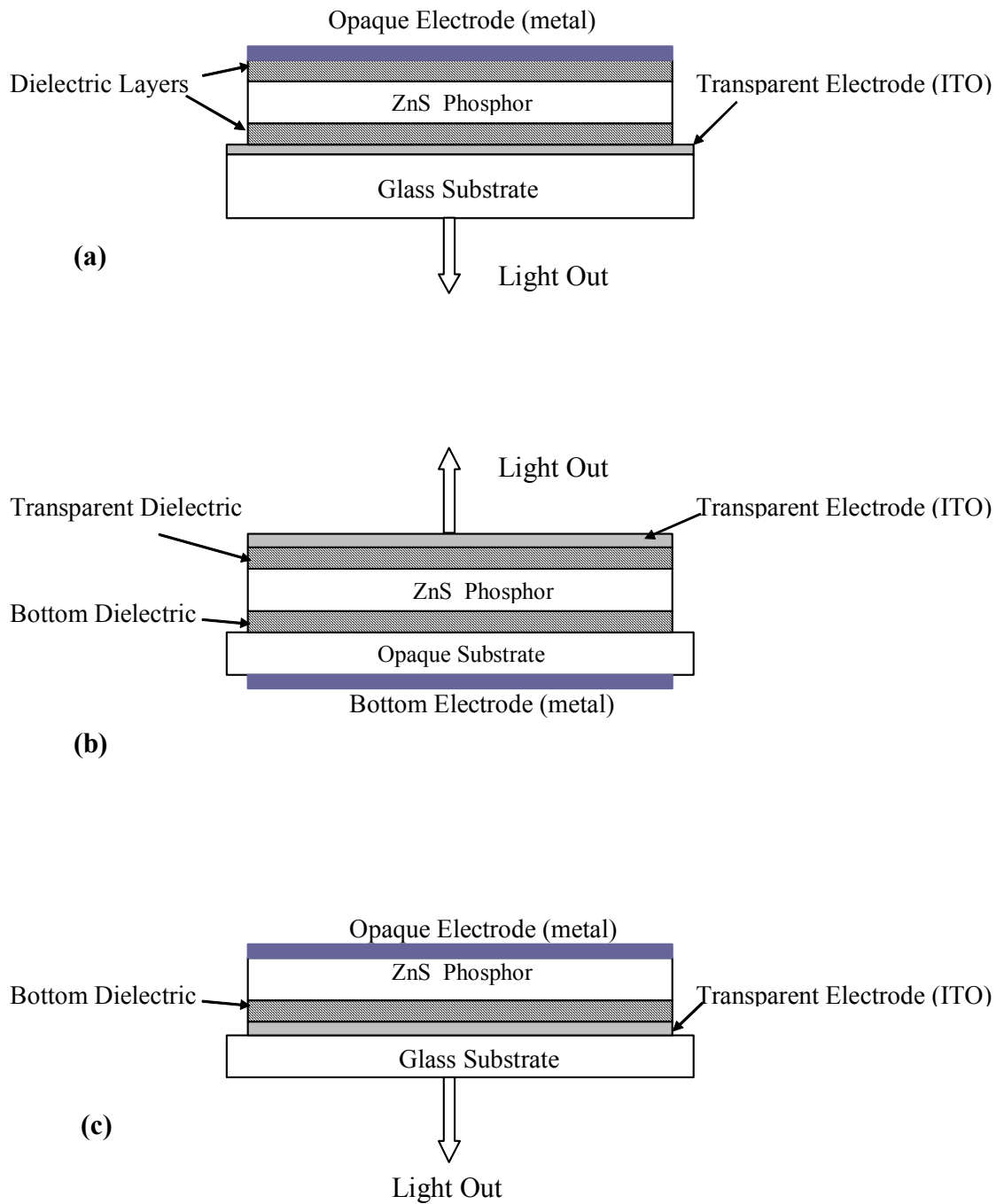


Figure 2.1 Schematic cross-section of (a) the standard double insulator structure, (b) inverted structure and (c) half-stack structure.

### 2.3.2 Full Color Displays

Full-color displays may be produced with a variety of structures. They may consist of a conventional structure, hybrid stacked-substrate, or “color-by-white” design. In a

conventional device (figure 2.2), the red, green, and blue (RGB) phosphors are patterned into pixels, and voltages applied to a matrix of row and column electrodes determine whether a given pixel is active.

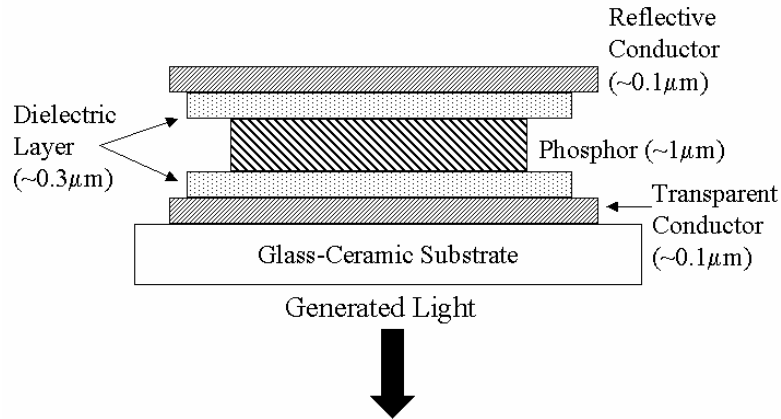


Figure 2.2 Schematic of conventional ACTFEL device.[11]

All approaches to a full-color display were hampered by the lack of a bright, saturated blue EL phosphor [44] until the recent success of SrS:Cu with co-dopants [45]. A schematic of the complex hybrid stacked substrate device is shown in Figure 2.3. In this case, two (red/green) primary color phosphors are patterned on one substrate, and one (blue) phosphor is on another. The substrates are then stacked together, requiring that the red-green substrate and top electrode be transparent, and the blue device be made using the inverted structure [3]. The advantage of this hybrid structure is that the processing and driving conditions may be optimized for each stack. The consequence is increased manufacturing costs due to double the number of substrates and electrode processes.

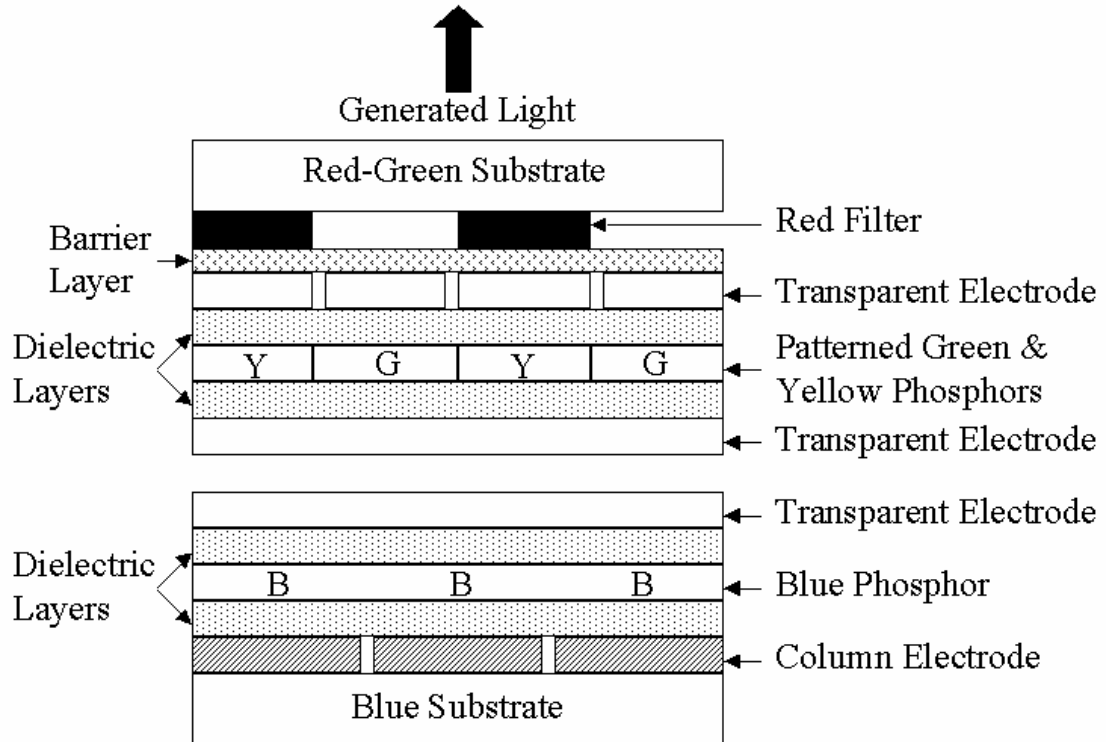


Figure 2.3 Hybrid stacked-substrate structure.

A filtered white structure, also known as “color-by-white,” is shown in Figure 2.4. This inverted structure passes white emission from a broadband single- or multi-layer phosphor through a set of RGB color filters. Note that the area of the filter and transparent electrodes are varied in order to achieve color balance [46].

The color by filtered white emission technique has been used to demonstrate color VGA active-matrix EL (AMEL) displays on silicon IC wafers with 2.5 cm diagonals [47, 48]. These will be used in consumer applications such as computer and entertainment displays, as well as military helmet-mounted displays.

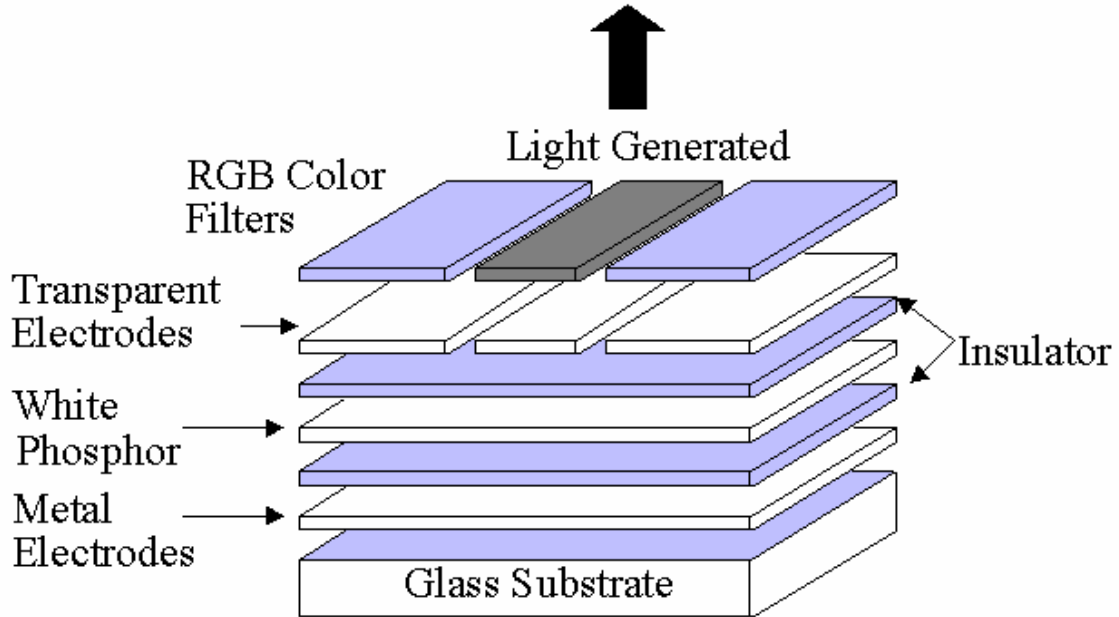


Figure 2.4 “Color-by-white” device structure [3].

#### 2.4 ACTFEL Device Physics

In this section we are mainly concerned with the basic physical processes and their interrelations which lead to high-field electroluminescence in zinc sulfide devices. A basic requirement for electroluminescence to occur is that an electric field be applied to a luminescent material with sufficient strength to generate charge carriers which can impact excite or impact ionize a luminescent center. Impact excitation and impact ionization are differentiated by the valence state of the impurity after impact [49]. Impact excitation does not change the valence of the impurity but rather rearranges the electrons to a higher energy configuration. Impact ionization of defects results from delocalization of a valence electron into a continuum state, such as the conduction band, and leaves an ionized center. This center is then free to recombine with a free electron. For example, in ZnS a  $Mn^{2+}$  ion is typically excited by direct impact, while in CaS a  $Eu^{2+}$  ion is thought to be ionized and then later brought back to its ground state after a radiative recombination with a free electron [49]. Impact ionization of the lattice can also occur resulting in

generation of an electron-hole pair. Figure 2.5 below shows a simple illustration of the six primary physical processes involved in the operation of an ACTFEL device. To observe electroluminescence:

1. electrons are injected from interface states by tunneling into the phosphor conduction band
2. electrons are accelerated to ballistic energies during high electric field transport across the phosphor; impact scattering can result in electron-hole production and electron multiplication in the host lattice
3. luminescent centers are impact excited
4. radiative de-excitation of the impact-excited luminescent center results in emission of light (6) and
5. electrons are trapped at the anode interface, resulting in a counter field that stops current flow [46]

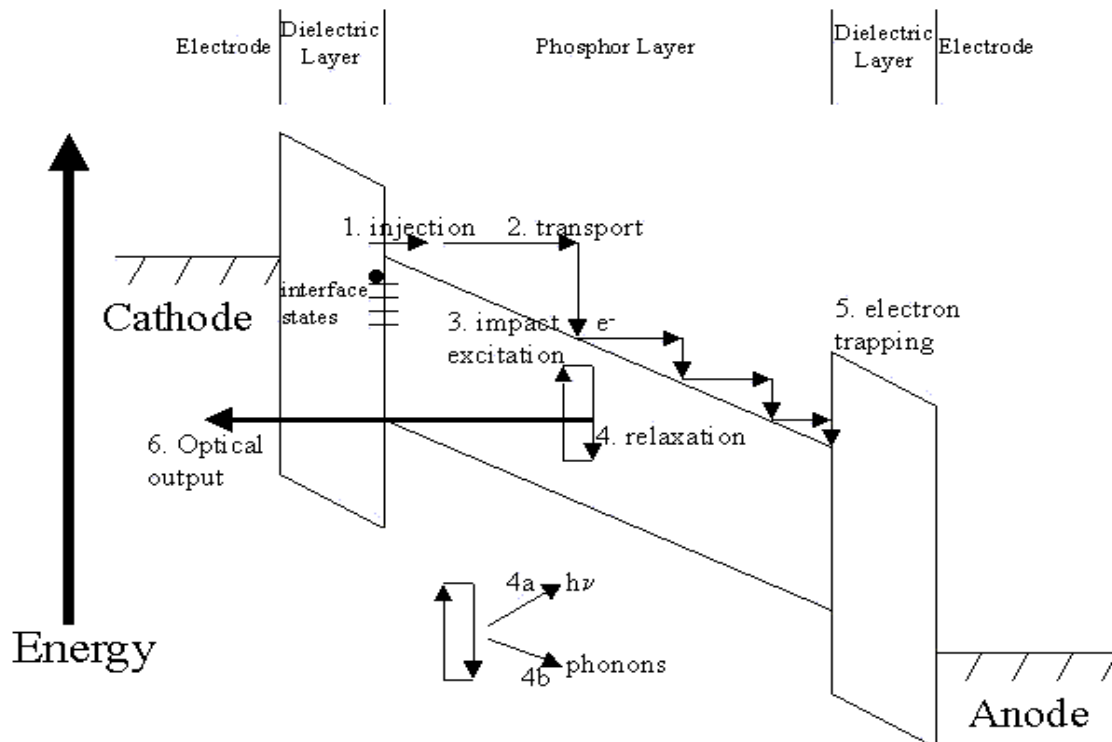


Figure 2.5 Energy band diagram of ACTFEL device and schematic illustrations of the EL emission mechanism.

### 2.4.1 Tunnel Injection

In general there are two mechanisms which are responsible for carrier injection, namely (1) thermionic emission, and (2) field emission or tunneling [50]. Several experiments support the fact the electrons trapped at the phosphor/insulator interface are the carrier source and that thermally assisted electron tunneling is the main mechanism. Typically, commercial ACTFEL displays are driven at 60 Hz with 30 microsecond pulses and an 8 microsecond rise and fall time. When the voltage applied to the device reaches a critical value (called the threshold voltage), the electric field at the phosphor becomes sufficiently large ( $\sim 1\text{-}2 \text{ MVcm}^{-1}$ ) and the energy bands are bent enough so that electrons trapped at interface states (or deep states distributed throughout the thin film) may tunnel into the phosphor conduction band. The tunneling emission current ( $J$ ) for Schottky barriers is given by [51]

$$J \approx E^2 \exp \left[ \frac{-8\pi\sqrt{2m^*} (q\phi B)^{3/2}}{3qhE} \right] \quad (2.1)$$

where  $E$  is the electric field,  $m^*$  is the effective electron mass,  $q$  is the charge of an electron,  $\phi B$  is the barrier height, and  $h$  is Planck's constant. For this equation to apply to electron trap state emission, the barrier height term is replaced by a term that represents the interface trap depth. The ideal electron trap depth is shallow enough to avoid excessively high fields for electron injection, but sufficiently deep so that injection fields will result in acceptable acceleration of the electrons. From this description it becomes apparent that, unlike in other semiconductor devices, a high density of interface states and deep bulk states is desirable in order to inject enough current to excite EL emission.

Several groups have attempted to increase the density of occupied states through modification of the phosphor/insulator interface. Kobayashi et al.[47], Ohwaki et al. [48], and Rack et al. [13] have added thin interfacial layers (SiO<sub>2</sub>, Ge, In) between the phosphor and insulator. In all cases, the interfacial layers were found to enhance the electron injection current, presumably through an increased density of trapped electrons. The other additional mechanism suggested for charge injection is thermionic emission. The expression relating the thermionic current,  $J_e$ , to temperature is the Richard-Dushman equation [52]:

$$J_e = \left( \frac{(kT)^2 m q}{2\pi^2 \hbar^3} \right) e^{-\phi/kT} \quad (2.2)$$

where,  $J_e$  is the electronic charge flux,  $m$  is mass of electron,  $k$  is Boltzmann's constant,  $\hbar$  is Planck's constant ( $h$ ) divided by  $2\pi$ ,  $\phi$  is the work function, and  $T$  is temperature. This equation must be modified to take the phosphor's electron affinity into account, as it is valid for the metal-vacuum interface.

#### 2.4.2 High Field Charge Transport

The mechanism of high field electron transport in ACTFEL devices has always been a matter of intense debate. Simulations of high-field electron transport in ACTFEL devices have been investigated by several groups using Monte Carlo techniques. Initially, Brennan [53] used a full-band ZnS structure to calculate the electron energy distribution for electric fields up to 1 MV/cm. For this electric field region, he concluded that very few electrons obtained sufficient energy to excite Mn luminescent centers. Later, a simple parabolic-band model [54] was used to simulate the high field transport properties in ZnS in which the conduction band was described by a single parabolic band. In addition, this parabolic band model assumed that the electron scattering was dominated by polar optical

phonon scattering. These calculations suggested that the electrons in ZnS experienced nearly loss free transport, which is referred to as electron runaway, and resulted in a very energetic electron energy distribution. Later, a nonparabolic conduction band was implemented by Bhattacharyya et al. [55], where they included scattering due to polar optical phonons, acoustic phonons, intervalley scattering, and ionized and neutral impurities. In this case, electron runaway was no longer observed and the electron energy distribution became stable. It was determined that nonpolar interactions and conduction-band nonparabolicity stabilized the electron distribution by increasing the electron-phonon scattering rates.

Figure 2.6 shows the electron energy distribution ( $n(E)$ ) as a function of electron energy for different phosphor fields, and the impact excitation rate for  $\text{Mn}^{+2}$  as a function of energy obtained from the nonparabolic band model [55]. The electron energy distribution ( $n(E)$ ) as a function of electron energy using the full-band model is shown in Figure 2.7. The  $\text{Mn}^{+2}$  impact excitation cross-section as a function of electron energy is also shown here. The data indicate that a majority of electrons are able to attain energies of around 2.12 eV, the minimum energy required to excite  $\text{Mn}^{+2}$ .

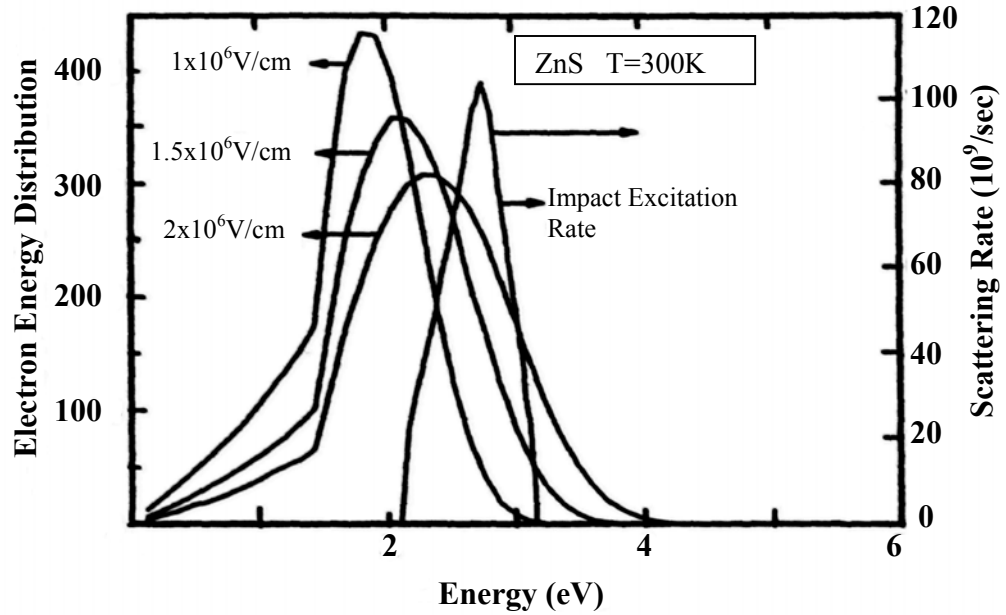


Figure 2.6 Electron energy distribution as a function of energy for different phosphor fields using the nonparabolic band structure model [55]. The impact excitation rate as a function of energy is also included.

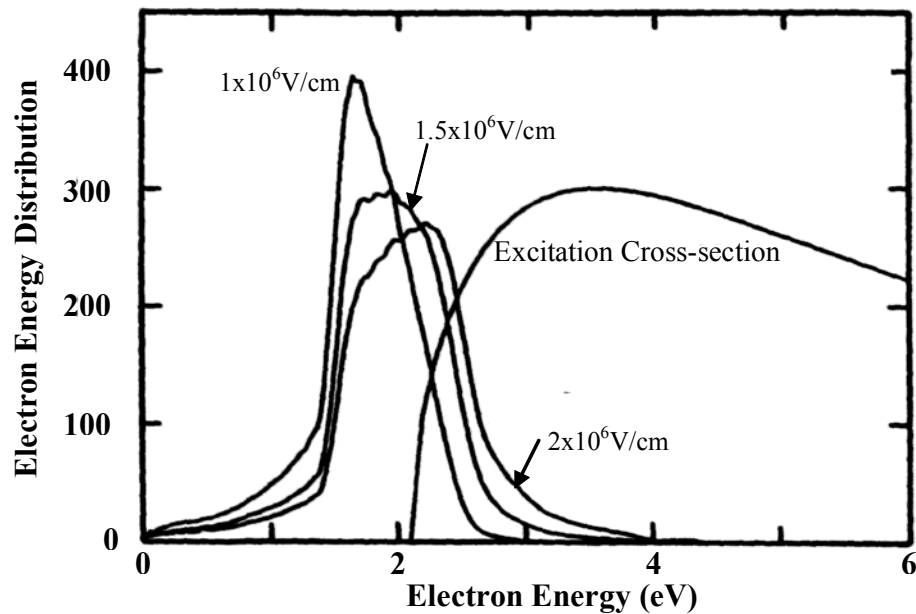


Figure 2.7 Electron energy distribution as a function of energy for different phosphor fields using the full-band structure model [55]. The impact excitation cross-section as a function of energy is also included.

A simpler approach was taken by Bringuier [56], who employed a lucky-drift approach. He made the argument that the full-band Monte Carlo approach may be more accurate, but given the lack of certainty in some physical parameters of II-VI compounds and the poor crystallinity in ACTFEL devices, the lucky-drift approach should be adequate to highlight the important factors in device operation. The lucky-drift approach is an extension of the original theory given by Baraff [57]. In this theory two transport modes are considered. One is ballistic transport, which is collision-free. The other is the drift mode, which occurs after the electron has had one collision, which increases the probability of subsequent collisions.

#### 2.4.3 Impact Excitation/Ionization

As the hot electrons travel through the phosphor matrix, a fraction may interact with the luminescent centers (activators), resulting in either impact excitation or impact ionization. The electron-luminescent interaction probability is related to the luminescent center radiative cross-section. Impact excitation is the case when an electron in the ground state of the luminescent center is excited to a higher electronic state localized on the activator ion core. De-excitation from the excited state may occur either radiatively or non-radiatively. Radiative relaxation paths result in the emission of a photon whose wavelength corresponds to the difference in energy between the excited and lower energy states. Non-radiative relaxation results in phonon emission, which will dissipate the potential energy of the excited luminescent center in the form of heat without resulting in luminescence. The delay time between excitation and relaxation can be long (ms) or short (a fraction of a  $\mu\text{s}$ ), depending on the spin and parity selection rules applied to the excited and ground states [46]. If the ballistic electron ionizes the ground state electron of the

luminescent center by impact scattering an electron into the phosphor conduction band, this process is called impact ionization. Once ionized, the activator ion core may trap either an electron or a hole and subsequently capture a carrier of the opposite charge to result in electron-hole recombination, with subsequent light emission. In high fields, the electrons are accelerated to such high energies that the cross section of capture and radiative relaxation is significantly reduced. In addition, at high fields the residence time of a trapped carrier may be so short that recombination is unlikely (i.e. the carrier may be field stripped from the center) [58]. At high fields, electron multiplication also occurs where one electron elastically scatters off of valence electrons creating two electrons and another hole. These two electrons may accelerate and scatter creating more electrons and holes, with the result known as avalanche breakdown. Because of these complications upon ionization, impact excitation is typically considered to be the dominant mechanism for generating light in ACTFELDs [33, 50]. Eventually, the ballistic electrons on reaching the anodic phosphor/insulator interface become trapped in interface states, causing a field of opposite polarity that influences current injection and transport during a large part of the voltage pulse in ACTFELDs.

#### 2.4.4 Radiative Decay

When an impurity center is in an excited state, that energy will eventually have to be dissipated. The relaxation process can occur by either a) emission of a photon, b) non-radiative relaxation or c) transfer of energy from one ion to another. For display applications, it is desirable to maximize the first process and to minimize the others.

For a two-level system, the rate of population state decrease to the ground state is given by

$$\frac{dN_e}{dt} = -N_e P_{eg} \quad (2.3)$$

where  $N_e$  is the number of luminescent ions in the excited state,  $t$  is the time, and  $P_{eg}$  is the probability for spontaneous emission from the excited to the ground state. Upon integration

$$N_e(t) = N_e(0) \exp\left(\frac{-t}{\tau_R}\right) \quad (2.4)$$

where  $\tau_R (=P_{eg}^{-1})$  is the radiative decay time [58].

The lifetime of the excited state depends on whether the emission is allowed or forbidden. For strongly forbidden emissions the lifetime can be in the range of microseconds to milliseconds, whereas for allowed transitions it may be microseconds or less [58].

#### 2.4.5 Optical Outcoupling

An important parameter to be considered is the direction in which the light must escape through the device; hence internal reflection becomes an important issue. In conventional EL devices light generated within the phosphor layer sees several interfaces as shown in Figure 2.8. The phosphor layer typically has the highest index of refraction in the stack, and all layers have a higher index of refraction than air. Hence when light travels from the phosphor layer through the insulators, we define critical angle for internal reflection ( $\theta_c$ ) as

$$\theta_c = \text{Sin}^{-1}(n_2 / n_1) \quad (2.5)$$

where  $n_1$  and  $n_2$  are refractive indices for each media. The extent of internal reflection can be estimated [11, 59] by assuming just the phosphor layer (for ZnS  $n=2.3$ ), and that light is reflected from the metal electrode by

$$\eta_{\text{opt}} = \int_0^{\arcsin\left(\frac{1}{2.4}\right)} \sin \theta d\theta = 1 - \left(1 - \left(\frac{1}{2.4}\right)^2\right)^{0.5} \approx 0.1 \quad (2.6)$$

The optical outcoupling efficiency can be improved by more than an order of magnitude by increasing the surface roughness and thereby reducing internal reflection [60]. However, too rough a surface can reduce contrast because of increased diffuse scattering [11].

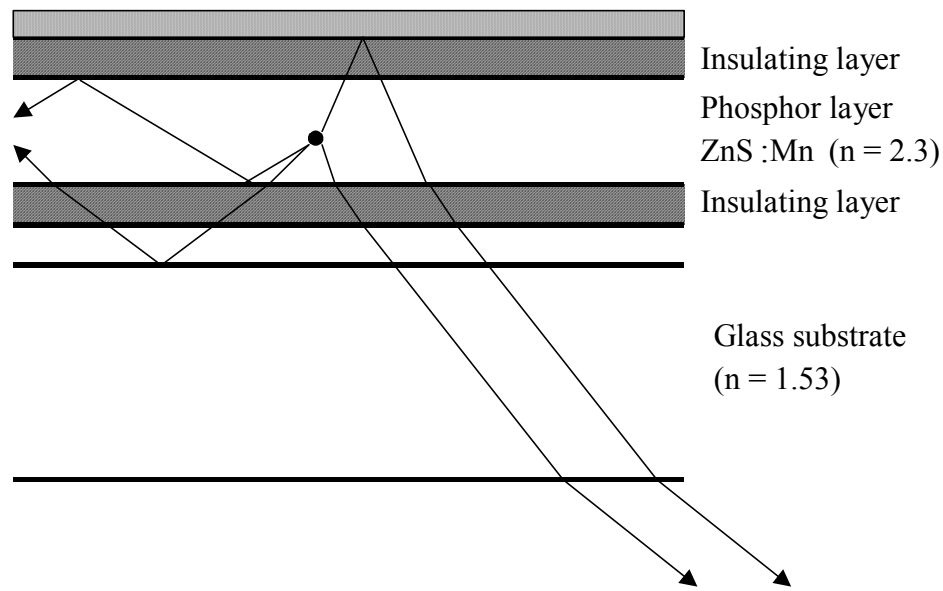


Figure 2.8 Schematic representation of internal reflection in a ZnS:Mn ACTFEL device [11].

## 2.5 ACTFELD Materials

The requirements and critical characteristics for the materials used in ACTFEL devices are discussed below.

### 2.5.1 Substrate Materials

The primary requirements for the substrates for the standard device structure are low cost and easy availability, high transmission coefficient, a thermal coefficient of expansion that is close to that of the deposited films and low alkali metal content (diffusion of metal ions from the glass into the phosphor layer results in deteriorated performance). The most common substrate material is Corning 7059 soda-lime-silicate glass. This is an alkali-free, barium borosilicate glass often used for LCD substrates [61]. It has a softening temperature of  $\sim 598^{\circ}\text{C}$  and large panels can undergo rapid thermal anneals (RTA's) of up to  $650^{\circ}\text{C}$  without significant damage or warping [62]. Soda lime glass has been used which poses a diffusion barrier to alkali metals [11]. Figure 2.9 is the transmission spectrum of this glass.

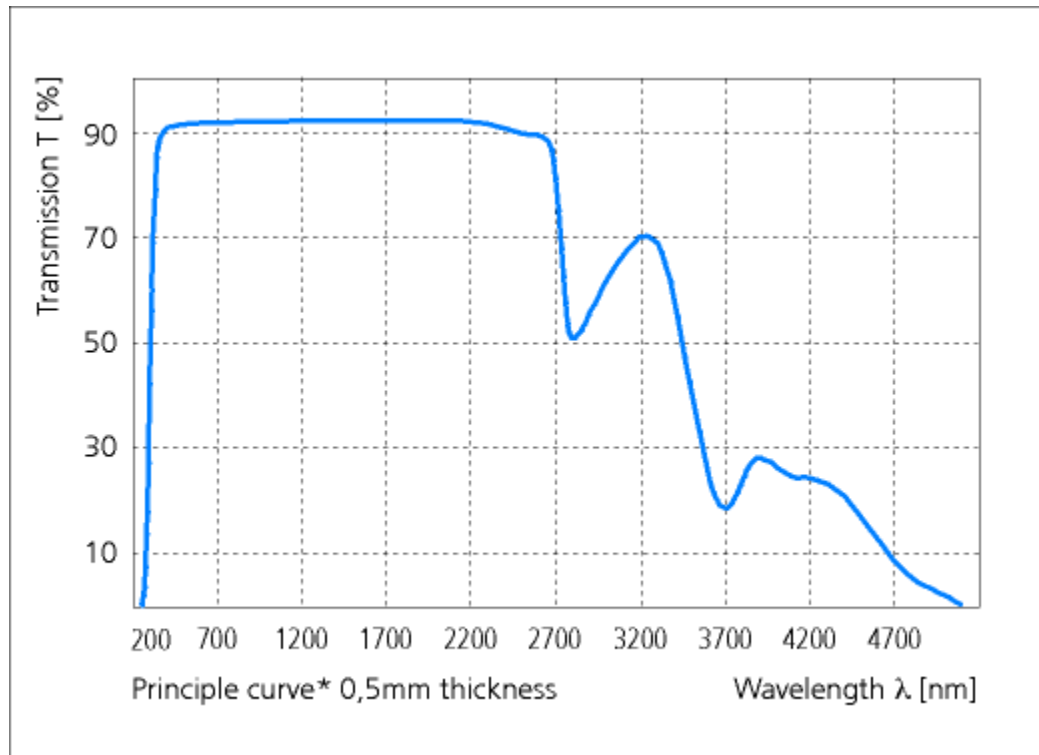


Figure 2.9 Transmission spectrum of 7059 glass [63].

For higher temperatures glass-ceramics substrates may be used which meet the substrate requirements, but these materials are expensive and not economically viable substrate materials for commercial applications. A cheaper alternative to these expensive substrates is silicon, which is readily available and can be used extensively for visible ACTEFEL devices in the inverted structure format or infrared light emitting ACTFEL devices in the standard structure format. These substrates can withstand high temperature heat treatments of post-deposition annealing.

For the inverted structure devices, the requirements are a smooth surface and the ability to meet the thermal considerations for processing of subsequent layers. For the inverted structure in Figure 2.1(b), the substrate acts as part of the device, comprising the bottom insulator, and electrical properties must be considered. These are discussed in the following section.

### 2.5.2 Transparent Electrodes

For the standard device structure the first layer deposited onto the glass substrate is the transparent conductor. The critical materials requirements of this layer are; it must be sufficiently conductive to not affect the RC time constant of the device, it must be as transparent as possible in the interested spectral region of emission to minimize absorption and/or color perturbation and finally it must withstand the thermal processing of subsequent layers. The material predominantly used is indium-tin-oxide (ITO) [11]. This is normally an alloy of 90 wt%  $\text{In}_2\text{O}_3$  and 5-10 wt%  $\text{SnO}_2$ . ITO can be deposited by a number of deposition techniques, namely pulsed-laser deposition, e-beam evaporation, DC magnetron sputtering, RF magnetron sputtering, plasma ion-assisted deposition, chemical vapor deposition and atomic layer deposition [11, 64-73]. ITO thicknesses of 200 nm are typical, and good transparency (>90%) can be obtained in the visible region

of the spectrum with a resistivity of  $\sim 1 \times 10^{-4} \Omega\text{-cm}$ , providing a sheet resistance of  $\sim 5 \Omega/\square$ . In addition, ITO is easily patterned with standard photolithography and wet or dry etching.

Though optically transparent, ITO is a degenerately doped n-type semiconductor. The n-type conductivity of ITO is due to the thermal ionization of shallow donors which arise from the substitution of  $\text{Sn}^{+4}$  onto  $\text{In}^{+3}$  lattice sites, and oxygen vacancies [74]. Zinc-oxide (ZnO) and zinc-oxide doped Al, In or Ga thin films are also used as transparent conducting electrodes. In the undoped material n-type conductivity is due shallow donor levels due to oxygen vacancies while in the doped system, the +3 valence state of Al, In or Ga substituting on  $\text{Zn}^{+2}$  lattice sites creates shallow donor levels [74]. It is also of importance to choose neighboring layers (substrate and bottom insulator) that do not interact significantly with the ITO layer during subsequent thermal processing. One thing to keep in mind is that, since ITO lacks transparency for wavelengths  $>$  plasma wavelength (1.6-2  $\mu\text{m}$ ), it is only useful for the near infrared light emitting devices. But for mid IR and far IR, ITO would be ineffective and in those circumstances it is wise to choose the inverted configuration ACTFEL device and use Si as a substrate.

### 2.5.3 Opaque Electrodes

For the standard structure, the requirements for the opaque electrode are not stringent because it is the last layer deposited. The top metal electrode is typically 100-300nm thick and is the last layer to be deposited during device fabrication. It must have a low resistivity, be resistant to electromigration (metal-ion migration) at high fields, have good adhesiveness to the insulating layers and must possess some ability to prevent breakdown spread when dielectric breakdown of the insulator (full stack structure) or

phosphor (half-stack) layers occurs. Aluminum is the best metal that satisfies these requirements. Aluminum also exhibits desirable wetting characteristics to many common insulator materials, and this provides the possibility for self-healing breakdown by fusing of the metal surrounding a short. The main drawback of Al is its high reflectivity, which leads to higher brightness but lower contrast. Mirror-type reflections occur when external light penetrates the devices and this negatively affects the display contrast. Filters are often used to suppress this back reflection so that only light generated by the device is observed by the viewer. The problem has also been effectively dealt with by adding either a dark layer above the phosphor or by adding a circular polarizer, which eliminates specular reflection [11].

For inverted structures, in which the electrode is deposited on the bottom of the substrate, aluminum is again commonly used since conductivity, cost, and ease of processing are the major concerns. However for the other type of inverted structure in which the opaque electrode is deposited below the rest of the EL device, the additional requirement for thermal stability is added. Au, Mo, Ta, and W are candidates for this type of structure.

#### 2.5.4 Insulator Materials

In the full stack structure, the dc path is blocked. The insulator thickness is usually in the 250nm range, which is too thick for electrons to tunnel through from the metal under cathodic bias. The device is therefore only capacitively coupled to the externally applied field. The main function of the insulator layers is to protect the ZnS phosphor from electrical breakdown (runaway avalanche breakdown eventually leading to destructive breakdown) at high fields (greater than 2MV/cm). The properties of the

insulator layers are therefore critical to device performance. The most important requirements [11, 75-80] of these layers are

1. High dielectric constant
2. High dielectric breakdown electric field strength
3. Must provide interface states at the insulator-phosphor interface, from which electrons can tunnel into the phosphor conduction-band under the influence of an applied field above a certain threshold value
4. A small number of pinholes and defects. Pinholes and defects offer sites for local field enhancement and consequent premature dielectric breakdown
5. Good mechanical adhesion and stress accommodation over process temperatures which range up to 600°C (the coefficients of thermal expansion varies widely for the (different layers))
6. Must act as a barrier to metal-ion diffusion into the phosphor layer

As we will discuss in detail shortly, above a certain applied threshold voltage carrier injection in to the phosphor layer conduction-band occurs due to field emission from interface states. Below the threshold field, the double insulator device structure is a perfect capacitor. Maxwell's equations then apply, and impose the following boundary conditions at the insulator-phosphor interfaces:

$$\epsilon_i^{t,b} E_i^{t,b} = \epsilon_p E_p \quad (2.7)$$

where  $\epsilon$  is the dielectric constant at the frequency of operation,  $E$  is the electric field, the subscripts  $i$  and  $p$  refer to the insulator and phosphor respectively, and the superscripts  $t$  and  $b$  refer to the top and bottom insulator. The total applied voltage is divided between each layer according to the following:

$$V_{\text{app}}^{\text{tot}} = E_i^{t,b} d_i^{t,b} + E_p d_p \quad (2.8)$$

where  $d_i$  and  $d_p$  are the thicknesses of the insulator and phosphor layers respectively.

From equations 2.7 and 2.8, the fraction of the total applied voltage that appears across the phosphor layer can be calculated as [11]

$$V_p = E_p d_p = \frac{\epsilon_i d_p}{\epsilon_i d_p + \epsilon_p d_i} \times V_{\text{app}}^{\text{tot}} \quad (2.9)$$

As equation 2.9 shows, the dielectric constant of the insulating layer ( $\epsilon_i$ ) must be as large as possible and its thickness ( $d_i$ ) as small as device reliability will permit, in order to maximize the voltage drop across the EL phosphor layer. Another advantage of insulators with a high dielectric constant is better device reliability due to lower operating voltages, because a proportionally smaller voltage will appear across the insulator layers. The threshold field for tunnel emission from interface traps in ZnS is  $\sim 1.8 \times 10^6$  V/cm [11]. According to equation 2.9, the minimum field that the insulator layer must sustain without breakdown in order to perform its function properly is

$$E_i^{\text{t,b}} = \frac{\epsilon_p E_p}{\epsilon_i^{\text{t,b}}} = \frac{8.3 \times 1.5 \times 10^6 \text{ V/cm}}{\epsilon_i^{\text{t,b}}} \quad (2.10)$$

where  $\epsilon_p$  (ZnS) is taken as 8.3. This equation shows that high breakdown field and high dielectric constant are inversely proportional, and this has been verified experimentally for several insulators. As high dielectric constant and high breakdown field are difficult to satisfy simultaneously, a figure of merit introduced by Howard [79] is used to rate insulators for ACTFEL devices. It is simply the product of the dielectric constant and the electrical breakdown field ( $E_{\text{DB}}$ ), and is a measure of the maximum trapped charge ( $\mu\text{C}/\text{cm}^2$ ) density at the insulator-phosphor interface. Table 2.2 presents a comparison of the important properties of several insulators. Unfortunately the insulators with the

highest figures of merit exhibit propagating breakdown, which when initiated, spreads catastrophically and eventually destroys the device.

Table 2.2 Typical insulator materials with relative dielectric constant, dielectric breakdown field, figure of merit (maximum trapped charge density at insulator- phosphor interface), breakdown mode and deposition technique. SHB= self healing breakdown; PB= propagating breakdown; PECVD=plasma enhanced chemical vapor deposition; ALE= atomic layer epitaxy; EBE= electron beam evaporation [11].

Material	Dielectric Constant ( $\epsilon_i$ )	Breakdown Field $E_{DB}$ (MV/cm)	Figure of Merit $\epsilon_i * E_{DB}$ ( $\mu\text{C}/\text{cm}^2$ )	Breakdown Mode	Deposition Method
SiO <sub>2</sub>	4	6	2	SHB	Sputtering
SiON	6	7	4	SHB	Sputtering/PCVD
Al <sub>2</sub> O <sub>3</sub>	8	5	3.5	SHB	Sputtering
Al <sub>2</sub> O <sub>3</sub>	8	8	6	SHB	ALE
Si <sub>3</sub> N <sub>4</sub>	8	6-8	4-6	SHB	Sputtering
Y <sub>2</sub> O <sub>3</sub>	12	3-5	3-5	SHB	Sputtering/EBE
Ta <sub>2</sub> O <sub>5</sub>	23-25	1.5-3	3-7	SHB	Sputtering
BaTiO <sub>3</sub>	14	3.3	4	SHB	Sputtering
BaTa <sub>2</sub> O <sub>6</sub>	22	3.5	7	SHB	Sputtering
PbTiO <sub>3</sub>	150	0.5	7	PB	Sputtering
TiO <sub>2</sub>	60	0.2	1	PB	ALE
SrTiO <sub>3</sub>	140	1.5-2	19-25	PB	Sputtering
Sr(Zr,Ti)O <sub>3</sub>	100	3	26	PB	Sputtering

### 2.5.5 Phosphor Layer

The phosphor layer materials consists of a host material and a luminescent center, each discussed below.

#### 2.5.5.1 Host material (matrix)

All phosphors consist of a host material, and a luminescent center or light-emitting dopant. Before proceeding with a detailed look at the ZnS host system, it is worth reviewing the properties that are desirable of all high-field electroluminescence hosts.

Namely:

1. The band-gap must be large sufficiently large, such that light emitted from the luminescent center will not be absorbed (the host should be transparent in the range of the electromagnetic spectrum that is of interest). Complete visible transmission requires a band-gap of at least  $\sim 3.1$  eV (400 nm). The equation for converting between energy, wavelength, and wavenumbers is

$$\lambda = 1240/E, \lambda = 1/\omega \text{ where } \lambda = [\text{nm}], E = [\text{eV}] \quad (2.11)$$

2. Hosts must be non-conducting below the EL threshold. This is required for a voltage drop and subsequent high electrical field across the phosphor, and leads to a capacitive sub-threshold behavior
3. The host must have a high breakdown strength to allow for efficient acceleration of electrons. The breakdown field of the host must be at least 1MV/cm
4. The host must have excellent crystallinity and a low phonon-coupling constant in order to minimize electron scattering. To maintain good crystallinity at the dopant levels ( $\sim 1$  at %) typically used in EL phosphors, it is desirable to match the geometric size as well as the valence of the host cation with that of the luminescent center [81]
5. The host must provide a substitutional lattice site of appropriate symmetry for the luminescent center

These requirements have historically been met best by sulfur-based compounds, especially ZnS, SrS, CaS, SrGa<sub>2</sub>S<sub>4</sub>, and CaGa<sub>2</sub>S<sub>4</sub> [1, 2, 5, 13] and thiogallates. Examples of the former group are ZnS, CaS, and SrS, while examples of the latter group are CaGa<sub>2</sub>S<sub>4</sub>, SrGa<sub>2</sub>S<sub>4</sub> and BaGa<sub>2</sub>S<sub>4</sub>. Table 2.3 summarizes the important physical properties of the sulfide based II-VI semiconductor hosts.

Table 2.3 Properties of some common ACTFEL host compounds [11].

Property	IIb-VIb compound	IIa-VIb compound	
Compound	ZnS	CaS	SrS
Melting Pt. (°C)	180-1900	2400	>2000
Band Gap (eV)	3.6	4.4	4.3
Transition Type	Direct	Indirect	Indirect
Crystal Structure*	ZB,W	Rock salt	Rock salt
Lattice constant (Å)	5.409	5.697	6.019
Dielectric const.	8.3	9.3	9.4
Ionicity	0.623	>0.785	>0.785

\*ZB = zinc blende; W = wurtzite; Orth. = orthorhombic

### 2.5.5.2 Luminescent centers

The activator impurity (dopant) in the phosphor influences the spectral properties, and to a large extent the temporal properties of optical emission. In many lamp and CRT phosphors, luminescence results from recombination of electrons and holes trapped in deep donor and deep acceptor levels, respectively. The most common examples of this type of phosphor are based on a ZnS host, with some combination of Ag, Cu, Au, Al, and Cl added as the acceptor and donor impurities to tailor the spectral properties and efficiency. This class of luminescent center is not used in ACTFEL devices because the electron-hole pairs are unstable under high fields and the luminescence is effectively quenched [11, 12].

The second type of center is a localized transition between electronic states of an isolated dopant ion. This dopant ion is typically either a transition metal such as  $\text{Mn}^{2+}$ ,  $\text{Cr}^{2+}$ ,  $\text{Ti}^{4+}$ ,  $\text{Cu}^+$ ,  $\text{Ag}^+$ , a rare earth ion such as  $\text{Eu}^{3+}$ ,  $\text{Er}^{3+}$ ,  $\text{Nd}^{3+}$ ,  $\text{Eu}^{2+}$ ,  $\text{Ce}^{3+}$ ,  $\text{Tb}^{3+}$ , or  $\text{Tm}^{3+}$ , or an  $s^2$  configuration ion such as  $\text{Pb}^{2+}$ , or  $\text{Bi}^{3+}$  [11, 58].

Without going into a detailed discussion of the underlying physics, the general emission characteristics of these ions can be separated into several categories based on the electronic configuration of the ground and excited states. One characteristic of importance in terms of both understanding the luminescent process and for application to displays is the radiative decay time. The mathematical description of decay behavior for a two-level system was described in Section 2.4.4. The decay time is determined primarily by two selection rules related to the electronic configuration of the ground and excited states, as well as the surroundings of the ion [58]. One of these selection rules is referred to as the parity selection rule, which forbids transitions between levels of the same parity, i.e. transitions within the  $d$  shell, within the  $f$  shell, or between the  $d$  shell and  $s$  shell are

forbidden. The other selection rule is the spin selection rule, which forbids transitions between configurations with different spin states. Forbidden transitions have longer decay times [58].

The transition metal ions mentioned above all have a  $d^n$  valence configuration, and emission spectra are all characteristic of intra-shell  $d-d$  transitions. They are therefore all forbidden by the parity selection rule [58], and their emission is usually broad band (although  $\text{Cr}^{3+}$  can exhibit line emission in some instances). Therefore decay times for the transition metals can be in the range of 100  $\mu\text{s}$  to several ms, depending on the spin selection rule and symmetry. Another general characteristic of the transition metal activators is that because the transitions originate in the valence  $d$ -shell, they are strongly influenced by the crystal field and ligand fields of the host.

Rare-earth (RE) or lanthanide ions are the second type of luminescent centers that are employed in zinc sulfide phosphors. These are typically used as  $\text{RE}^{+3}$ , which in general, except for  $\text{Ce}^{+3}$ , exhibit parity forbidden, long-lived  $4f-4f$  transitions. Rare-earth ions have an electron configuration of  $1s^2 2s^2 2p^6 3s^2 3p^6 4s^2 3d^{10} 4p^6 5s^2 4d^{10} 5p^6 6s^2 4f^x$ , and the energy levels of the atomic orbitals fill up in order of increasing energy as is shown in Figure 2.10. Thus, the  $5s, 5p$  and  $6s$  orbitals fill up before the  $4f$  orbital, even though the radial probability distribution of the  $4f$  orbital has its maxima closer to the nucleus. As a result, the emission spectra of transitions which arise from the  $4f^n$  configuration appear as narrow lines because the  $4f$  electrons are well shielded from their environment by the  $5s$  and  $5p$  electrons. Figure 2.11 is a schematic representation of this shielding effect in  $\text{RE}^{+3}$  ions.

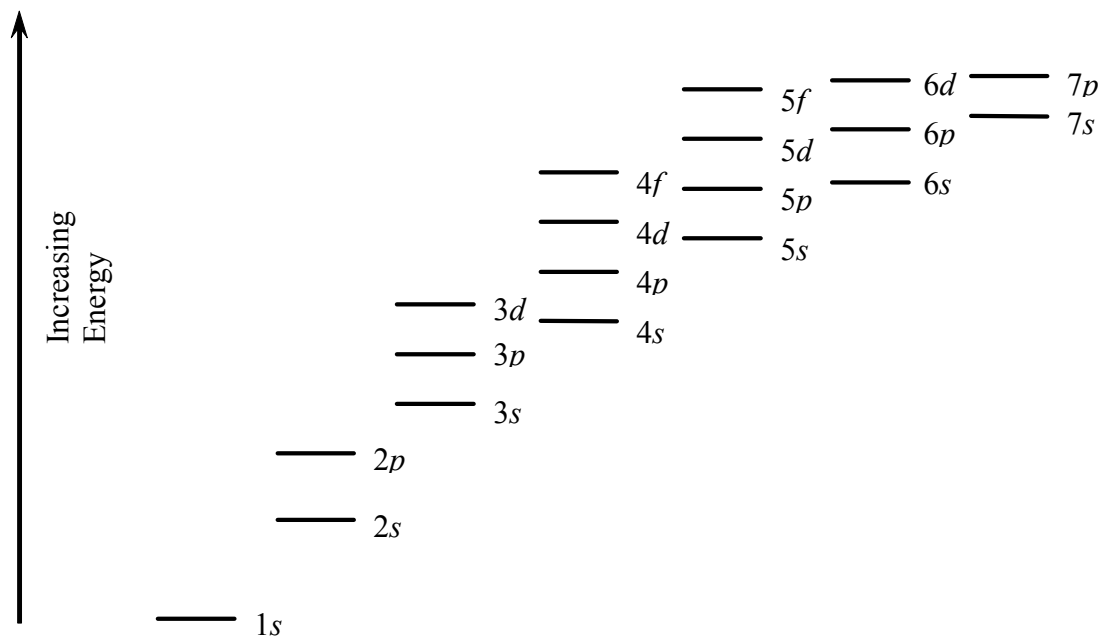


Figure 2.10 The relative energy levels of the atomic orbitals in multi-electron atoms [82]. Orbitals fill up in order of increasing energy as shown above.

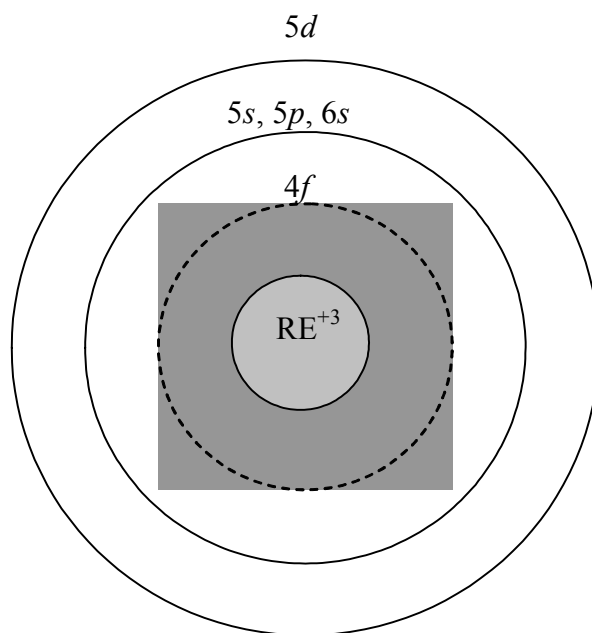


Figure 2.11 Schematic diagram of a  $\text{RE}^{+3}$  ion showing the radial position of the outer orbitals. Note that  $4f$  electrons are shielded, but  $5d$  electrons are exposed to the environment.

In cases where emission is a result of  $5d-4f$  transitions (e.g.  $\text{Ce}^{+3}$ ,  $\text{Eu}^{+2}$  and  $\text{Nd}^{3+}$ ) the emission spectra are broader because the  $5d$  electrons are unshielded and are therefore influenced by their surroundings i.e. the excited state is influenced by the crystal field, the nephelauxetic effect and other luminescent center-host lattice interactions. Since  $5d-4f$  transitions are parity allowed, they are faster than the parity forbidden  $4f-4f$  transitions. The book by Blasse and Grabmaier [58] provides excellent details of these effects on luminescent ions. Figure 2.12 shows the partial energy level diagram for several rare-earth ions. Among these are blue emitting  $\text{Tm}^{+3}$ , green emitting  $\text{Er}^{3+}$  and the orange emitting  $\text{Nd}^{3+}$  in ZnS. All these ions also have significant emission lines in the infrared region. We shall elaborate on these and other ZnS phosphors in the device section of this article. The infra-red properties of rare-earth ions are being actively researched for several applications including optical telecommunications, optoelectronic electronic integrated circuitry, lasers and sensors to name a few [83].

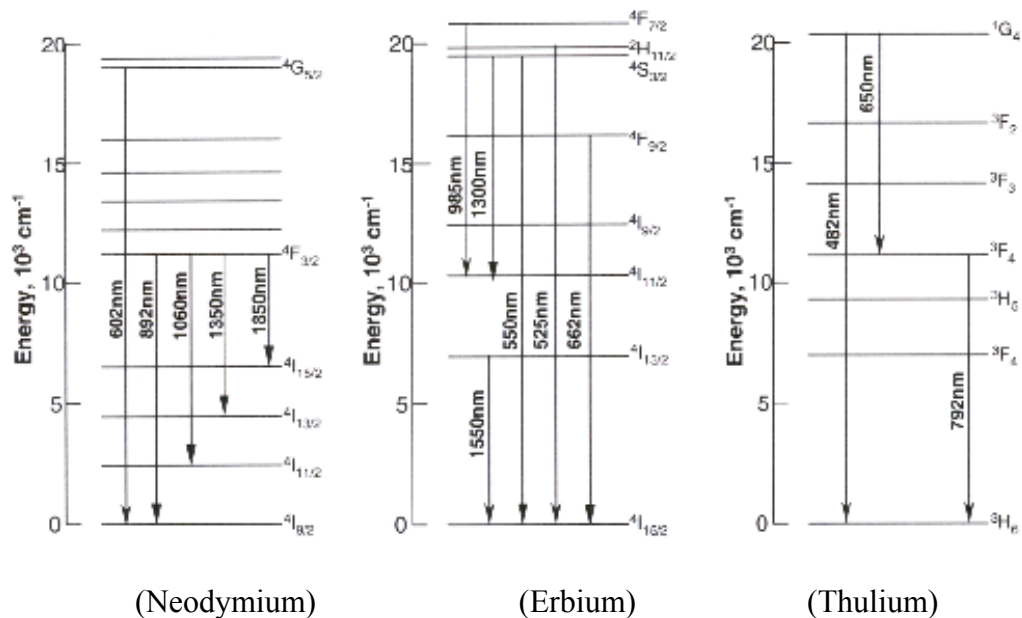


Figure 2.12 Energy level scheme for different rare earths [84, 85].

The second type of rare earth transition is an intra-shell  $4f-4f$  transition [58, 86]. This type of transition is seen in  $\text{Er}^{3+}$ ,  $\text{Tm}^{3+}$ , and most other trivalent rare earths. The transitions are all parity forbidden and may have decay times typically of several ms. The spectra are characterized by line transitions, and are insensitive to the surroundings and symmetry of the ion since the  $4f$  electrons are shielded by the  $6s$  orbital.

The excitation cross-section of the luminescent center,  $\sigma$ , is discussed frequently in the literature [6, 11, 13, 49, 56, 59, 87, 88]. This value relates the concentration of the centers to the mean free path for excitation through the simple relation,

$$l_i^{-1} = \sigma N \quad (2.12)$$

where  $N$  is the concentration of centers and  $l_i$  is the impact length. Some groups have directly measured the value for  $\sigma$  of  $\text{Mn}^{2+}$  in ZnS by measuring the efficiency and calculating the value from other known parameters [59]. The resulting value was similar to the physical ionic cross section. However, other efforts to predict impact cross sections for  $\text{Mn}^{2+}$  and other ions have shown that this is an extremely difficult task and accurate values are elusive [89], thereby impeding the ability to predict device efficiency. It is reported in the literature that it is desirable to have a large luminescent center impact cross section for good device efficiency, however there is not much practical value to this statement as the cross section has only been determined by measuring efficiency, and it is an intrinsic property of the atom.

#### 2.5.5.3 Luminescent-center host-lattice systems

In addition to considering the electrical properties and processing conditions of the host and the luminescent properties of the center, one must consider the compatibility and interrelationships between the two. The size mismatch of the activator on the cation site

is important, as is the valence match (or mismatch). Listed in Table 2.4 are the valence and ionic radius of common ACTFEL host cations and dopants. Minimizing the size and valence mismatch allows the incorporation of the dopant with the least concentration of induced defects.

Table 2.4 List of valence and ionic radius for cations commonly used in ACTFEL hosts, a well as common dopant ions [90].

Ion	Radius [ $\text{\AA}$ ]	Ion	Radius ( $\text{\AA}$ )	Ion	Radius ( $\text{\AA}$ )
Zn <sup>2+</sup>	0.74	Mn <sup>2+</sup>	0.80	Tm <sup>3+</sup>	0.88
Ca <sup>2+</sup>	0.99	Ce <sup>3+</sup>	1.03	Er <sup>3+</sup>	0.95
Sr <sup>2+</sup>	1.13	Tb <sup>3+</sup>	0.92	Ho <sup>3+</sup>	1.17
		Dy <sup>3+</sup>	0.62	Nd <sup>3+</sup>	1.123

The most commonly used and best performing visible EL phosphor system is Mn-doped ZnS. This phosphor can be filtered to obtain both green and red emission. To complete a full color display, there has been a tremendous amount of effort devoted to the development of a sufficiently bright and stable, saturated blue phosphor. Promising results were obtained for SrS:Ce. However the blue-green chromaticity and low luminance when filters are used were the primary limitations for this phosphor [13]. Nevertheless full color displays were developed based on this material. Promising results were also obtained for (Sr,Ca)Ga<sub>2</sub>S<sub>4</sub>:Ce, which had superior chromaticity, but lower brightness and greater difficulty in deposition and processing [13]. Recently excellent performance has been demonstrated for blue-emitting SrS:Cu,Ag [91, 92]. A list of results obtained for sulfide-based phosphors is given in Table 2.5. More details regarding these phosphor systems are available in the literature [13].

Table 2.5 Comparison of the visible characteristics of ZnS electroluminescent phosphors.

Phosphor Material	Emission Color	CIE Coordinates	Subpixel Luminance at 60 Hz (cd/m <sup>2</sup> )	Luminous Efficiency (lm/W)
ZnS:Mn	Yellow	x=0.5, y=0.5	600	5
ZnS:Mn/filter	Red	x=0.65, y=0.35	75	0.8
ZnS:Mn/filter	Yellow-green	x=0.45, y=0.55	80	
ZnS:TbOF				
ZnS: Tb, F	Green	x=0.30, y=0.60	125	1.3
	Green	x=0.30, y=0.60	90	0.5-1
ZnS: Sm, Cl				
ZnS: Sm, F	Red	x=0.64, y=0.35	12	0.08
	Orange-red	x=0.60, y=0.38	8	0.05
ZnS: Tm, F				
	Blue	x=0.15, y=0.15	<1	<0.01
ZnS:Mn/ SrS:Ce	White	x=0.42, y=0.48	450	1.6
SrS: Ce, Eu	White	x=0.41, y=0.39	36	0.2
CaS: Eu	Red	x=0.68, y=0.31	12	0.05
CaS: Ce	Green	x=0.27, y=0.52	10	0.1
CaGa <sub>2</sub> S <sub>4</sub> : Ce	Blue	x=0.15, y=0.19	13	0.04

## 2.6 ACTFEL Device Characterization

To understand the result of the current study, previous studies of some optical and electrical characteristics are reviewed. The interested reader is also referred to the critical review article on this subject by Wager *et al.* [46]

### 2.6.1 Optical Characteristics

For practical applications, the optical output of EL devices is a critical parameter. Two systems units for quantifying optical output are used. Radiometric units are optical power units and can be used to quantify all electromagnetic radiation. These units

quantify the photon flux density (radiant flux density) at a given wavelength. Optical power or *irradiance* is measured in  $W/cm^2.nm$ .

Photometric units can be used to quantify light only in the visible part of the spectrum. The photometric system takes into account the spectral response of the human eye. This response curve is called the *luminosity curve for the standard observer* (also known as the *CIE curve*). A brightness scale is the basic measuring element of the standard observer curve. That is, human observers were asked to rank by brightness various wavelengths of light of known flux density. The response curve can be interpreted as follows: A wavelength of 555 nm will appear brighter than any other wavelength of the same radiometric power. A source that can emit the same radiometric energy at 555 nm and 610 nm will appear only half as bright when operated at 610 nm as it does when operated at 555 nm. This relative brightness is known as the relative luminosity. Brightness is formally referred to as luminance. Table 2.6 shows the relative luminosity as a function of wavelength. A plot of the relative luminosity versus wavelength yields *the luminosity curve for the standard observer* or *CIE curve*. Notice that at 555 nm the relative luminosity is equal to unity i.e., the human eye is most sensitive to this wavelength.

Table 2.6 Relative luminosity as a function of wavelength that is the basis of the *CIE* or standard observer curve which, accounts for the spectral response of the human eye.

Wavelength (nm)	Relative Luminosity ( $\eta$ )
410	0.001
420	0.004
430	0.012
440	0.023
450	0.038
460	0.060
470	0.091
480	0.139
490	0.208
500	0.323
510	0.503
520	0.710
530	0.862
540	0.954
550	0.995
555	1
560	0.995
570	0.952
580	0.870
590	0.757
600	0.631
610	0.503
620	0.381
630	0.265
640	0.175
650	0.107
660	0.061
670	0.032
680	0.017
690	0.008
700	0.004
710	0.002
720	0.001

#### 2.6.1.1 Luminance-voltage

The most important aspect of light generation is the response to an electrical stimulus. Hence most investigators characterize ACTFEL devices by the brightness

versus voltage (B-V) data. A variable ac voltage source drives the device (typically with a trapezoidal pulse with frequency of 60Hz or 2.5kHz) and a suitable spectrometer is used to record the brightness data. The resulting plot is illustrated below in Figure 2.13.

A critical parameter for device performance is the threshold voltage,  $V_{th}$ . In terms of device physics, this is the voltage at which electrons are accelerated to sufficiently high energies to excite the luminescent centers and result in light emission. One definition of the threshold is the voltage at which the brightness level reaches  $1 \text{ cd/m}^2$ . Another definition is the intersection on voltage axis of the extrapolation of the

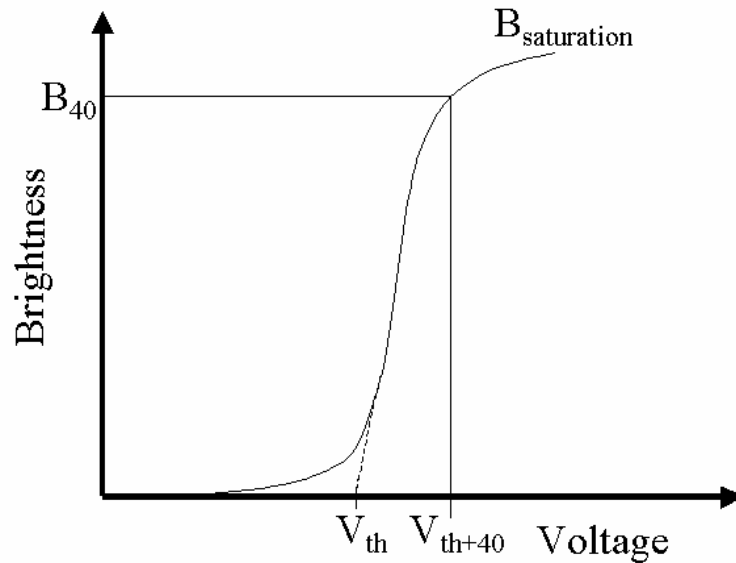


Figure 2.13 Schematic illustration of  $V_{th}$  and  $B_{40}$  for brightness vs. voltage data.

maximum linear slope of the B-V curve. While  $V_{th}$  is the voltage at which EL is detected, the applied voltage ( $V$ ) drops across the dielectric layers in addition to the phosphor according to the equation:

$$V = E_i^t d_i^t + E_p d_p + E_i^b d_i^b \quad (2.13)$$

where  $E_i^t d_i^t$  and  $E_i^b d_i^b$  are the products of the electric field and layer thickness in the top and bottom dielectrics, respectively, and  $E_p d_p$  is the product of the electric field and layer

thickness of the phosphor. Therefore the threshold voltage is influenced by the properties of both the phosphor and the insulators. This fact is important in multicolor displays, since matched threshold voltages for different phosphors greatly simplify the drive electronics.

Above the threshold, brightness typically increases linearly with the increasing field until either the device saturates or the phosphor undergoes dielectric breakdown. The brightness in this linear portion of the B-V plot can be approximated by the equation [4]

$$\begin{aligned} B(V) &= 2f\eta_p V_{th} Q \\ &= 2f\eta_p \left[ \frac{(C_i)^2}{C_i + C_s} \right] V_{th} (V - V_{th}) \end{aligned} \quad (2.14)$$

where  $f$  = drive frequency,  $\eta_p$  = photometric efficiency,  $C_i$  and  $C_s$  are capacitances of the insulator and phosphor layers, respectively,  $V$  = applied voltage, and  $V_{th}$  = threshold voltage. Another useful value on the B-V plot is  $B_{40}$ , which is the brightness at 40 V above the threshold voltage. This is a typical value at which ACTFEL devices may be driven, and it has been adopted as a standard measure of phosphor performance. To reliably compare  $B_{40}$  values requires a constant phosphor layer thickness and standard voltage frequency. In the case of thicker films, more luminescent centers may be excited, which would result in a larger number of excitation/de-excitation (light-emitting) processes per unit time. To a first approximation, the brightness is nearly linear with respect to phosphor thickness and frequency of excitation. These facts are often used to compare data taken at different frequencies or thickness.

The efficiency of light generation is another critical parameter for ACTFEL devices. This efficiency,  $\eta$  (lumens per watt or lum/W), can be approximated by the simple formula [13]

$$\eta = \frac{B}{P} \pi \quad (2.15)$$

where  $B$  = photometric brightness or luminance ( $\text{cd/m}^2$ ) and  $P$  = power density ( $\text{W/m}^2$ ), assuming an ideally diffuse (Lambertian) emission surface. This efficiency is commonly determined by obtaining  $B_{40}$  and dividing by power at 40 V above threshold from charge-voltage data (see Section 2.6.6.2).

While this is true for measuring the visible light efficiency, the infrared light efficiency is measured in a slightly different manner. We have to use the power units ( $\mu\text{W/cm}^2$ ), for calculating efficiency of a particular transition and summate the total area under the curves for all the transitions to get an approximate value of the total device efficiency. The efficiency is then calculated by

$$\eta = \frac{P_{in}}{P_{out}} \times 100 \quad (2.16)$$

where  $P_{in}$  is the product of  $V_{el}$  (voltage across the device) and  $I$  (device current), whereas  $P_{out}$  is calculated from the emission spectrum of the device.

#### 2.6.1.2 CIE color coordinate scheme

Any color can be obtained by appropriate combination of the three primary colors i.e., red, green and blue. The standard for colorimetry is the *Commission Internationale de 'Eclairage (CIE)* system which employs a three-dimensional diagram to represent the attributes of color. The *CIE* color coordinates are defined as the ratios:

$$\begin{aligned}
 x &= \frac{X}{X + Y + Z}, \\
 y &= \frac{Y}{X + Y + Z}, \\
 z &= \frac{Z}{X + Y + Z}
 \end{aligned}
 \tag{2.17}$$

where  $X$ ,  $Y$  and  $Z$  are the integrated tristimulus values over the entire blue, green and red regions of the electromagnetic spectrum, i.e., over the entire visible spectrum. The green spectrum used in this scheme corresponds to the photopic response of the eye and peaks at 555nm as discussed in the preceding subsection. Since the sum of the components  $x$ ,  $y$  and  $z$  equals unity, it is sufficient to specify  $x$  and  $y$  only in order to define a color. Figure 2.14 is a representation of the two dimensional *CIE* color coordinate system.

## 2.6.2 Electrical Characteristics

### 2.6.2.1 Equivalent circuit models of ACTFEL devices

To understand the electrical characteristics of an ACTFEL device it is necessary to interpret its equivalent electrical model. An ACTFEL device has a double insulating layer structure in which the insulating layers sandwich the phosphor layer. The ideal electrical behavior of ACTFEL devices is often modeled as a capacitor in parallel with a non-linear resistor as shown in Figure 2.15(a). The other model treats the two insulating layers as perfect capacitors and the phosphor layer as a capacitor shunted by two back-to-back Zener diodes as shown in Figure 2.15(c).

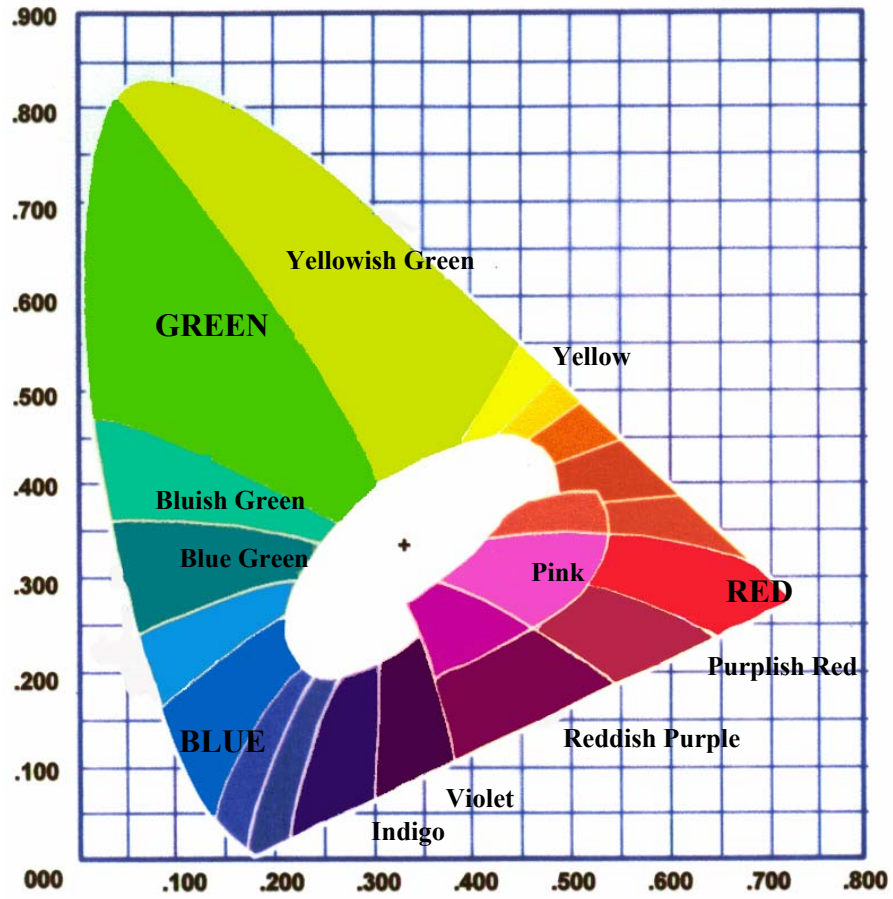


Figure 2.14 The *Commission Internationale de 'Eclairage (CIE)* color coordinate system.

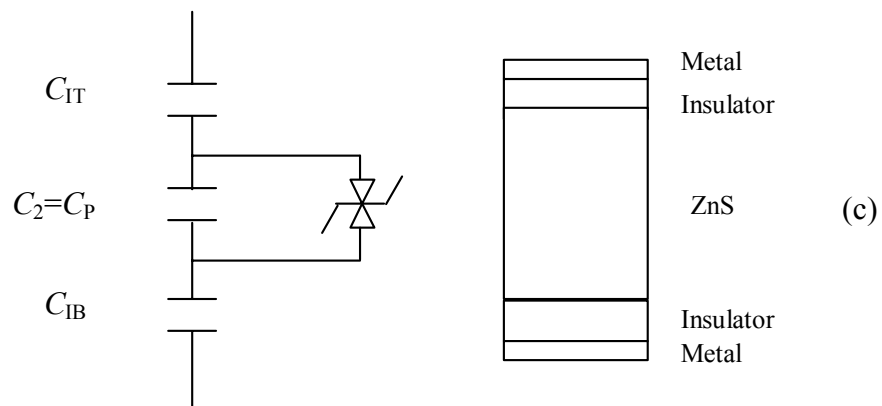
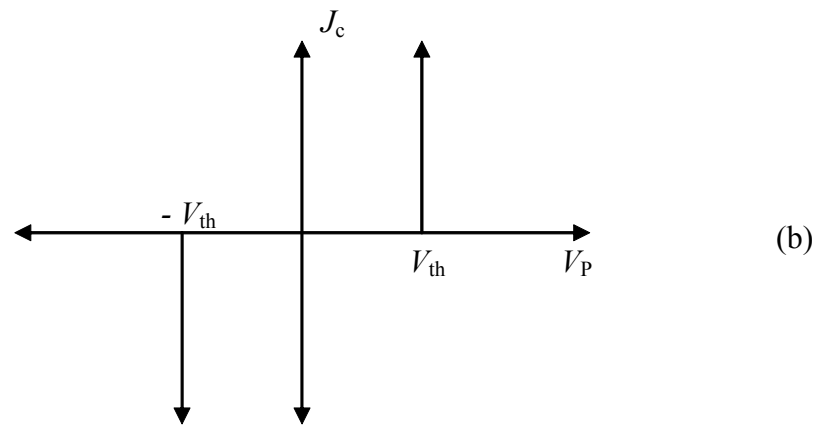
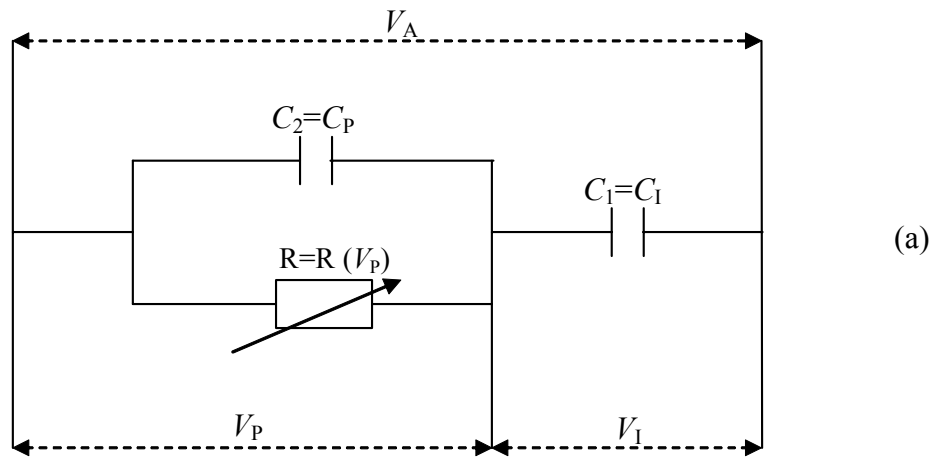


Figure 2.15 (a) The equivalent circuit of an ACTFEL device modeled as a capacitor in parallel with a non-linear resistor (b) ideal quasi-static current-voltage characteristic of the non-linear resistor and (c) equivalent circuit of an ACTFEL device modeled as two back-to-back Zener diodes[75].

As shown from Figure 2.15(a), the total applied voltage on the device ( $V_a$ ) is equal to the voltage across the phosphor layer ( $V_p$ ) plus the voltage across the insulating layers ( $V_I$ ) and is given by

$$V_a = V_p + V_I \quad (2.18)$$

The derivation of the following characteristics is given in more detail by Ono [11], but results of the circuit analysis are presented here. Below threshold, the applied voltage is capacitively divided by the phosphor and the insulators giving

$$V_p = \frac{C_I}{C_I + C_P} V_a \quad (2.19)$$

$$V_I = \frac{C_P}{C_I + C_P} V_a \quad (2.20)$$

where  $V_a$  is the applied voltage and  $V_I$  and  $V_p$  are the voltages across the insulators and the phosphor layer, respectively.  $C_I$  and  $C_P$  are the insulator and phosphor capacitance, respectively.

Above threshold, the resistive portion of the phosphor circuit allows current to flow (conduction current) until the voltage across the phosphor returns to threshold. At the same time the conduction current must be balanced by capacitive current which will charge the insulating capacitors to maintain the overall voltage across the device. So the final voltages above threshold are

$$V_{P,f} = V_{P,th} = \frac{C_I}{C_I + C_P} V_{th} \quad (2.21)$$

$$V_{I,f} = V_a - V_{P,f} = \frac{C_P}{C_I + C_P} V_{th} \quad (2.22)$$

Here the concept of field clamping is apparent. The phosphor layer in this simple equivalent circuit model is maintained at the threshold voltage regardless of the applied voltage.

From Figure 2.15(c), Ono [11] summarized that relation between the capacitance and the applied voltage as follows. Here the top and bottom insulating layers are assumed to be perfect capacitors, whose total effective capacitance is given by

$$C_I = \frac{C_{IT} C_{IB}}{C_{IT} + C_{IB}} \quad (2.23)$$

where  $C_{IT}$  and  $C_{IB}$  are the capacitance of the top and bottom insulators, respectively.

Below the threshold voltage, the phosphor also acts as a capacitor. Above threshold, however, a dissipative current flows through this layer and results in light emission. The brightness of the device is proportional to the power consumed by the resistive branch of the circuit.

#### 2.6.2.2 Electrical characterization

Since the ACTFEL device is an optoelectronic device it is necessary to measure certain properties in terms of parameters such as charge-voltage (Q-V), capacitance-voltage (C-V), internal charge-phosphor field ( $Q_{int}$ - $F_P$ ) and maximum charge-maximum voltage ( $Q_{max}$ - $V_{max}$ ). Wager employed a circuit that is employed for two-terminal electrical characterization [11, 93-95] and is shown in Figure 2.16. This technique involves using standard trapezoidal waveforms (as well as other arbitrary waveforms). This technique uses the instantaneous values for external voltage and current or charge and, assuming the phosphor and insulator to be ideal electrical components, uses simple circuit equations to calculate the conduction current and the conduction charge. Some of the basic relationships are given below.

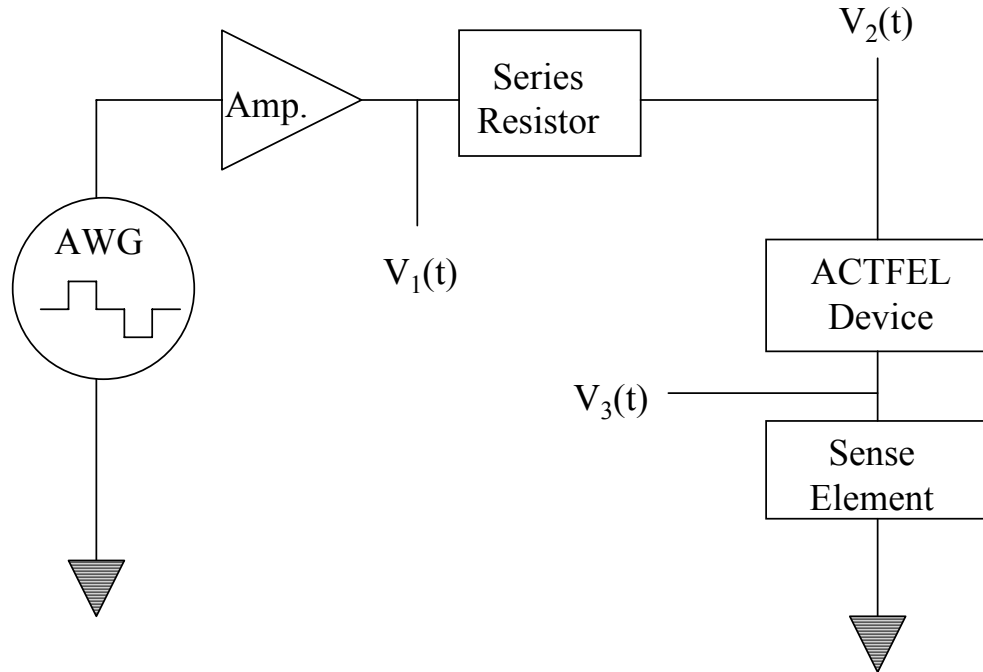


Figure 2.16 Schematic diagram of circuit used to measure conduction current using a Sawyer-Tower bridge [46].

The applied waveform is presented in Figure 2.17 using a labeling scheme common in the literature [46]. The waveform is trapezoidal, typically with a  $5 \mu\text{s}$  rise,  $30 \mu\text{s}$  dwell, and  $5 \mu\text{s}$  fall. The importance of all labeled points in Figure 2.17 are self-explanatory, with the exception of points B and G, which correspond to the voltage at which conduction charge becomes significant.

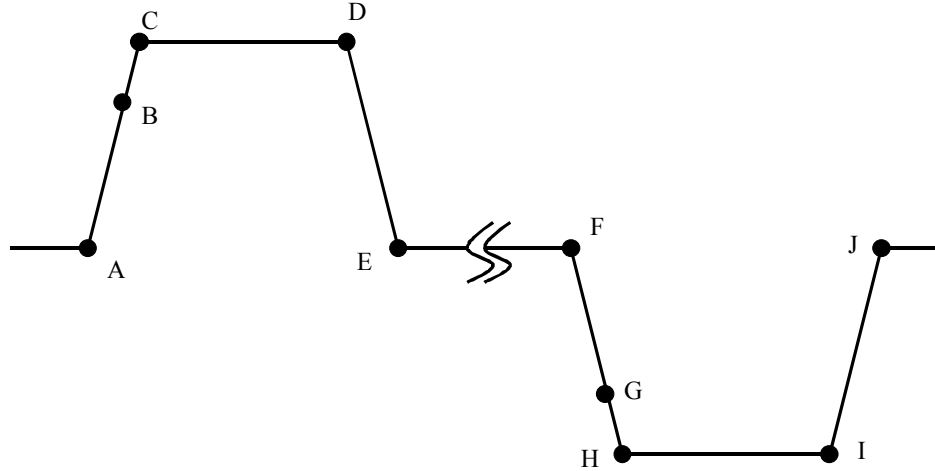


Figure 2.17 Schematic diagram of the voltage waveform used in ACTFEL device operation and characterization. Important features are labeled and discussed in the text.

The applied voltage is found by

$$V_{ap}(t) = V_2(t) - V_3(t) \quad (2.24)$$

When using a sense resistor, the external charge is simply the time integrated current,

such that

$$i(t) = \frac{V_1(t) - V_2(t)}{R_{series}} \quad (2.25)$$

$$q_{ext}(t) = \int_0^t i(t) dt \quad (2.26)$$

where  $R_{series}$  is the series resistance.

If using a sense capacitor, these values are determined by

$$q_{ext}(t) = C_s V_3(t) \quad (2.27)$$

$$i(t) = \frac{dq_{ext}(t)}{dt} \quad (2.28)$$

where  $C_s$  is the sense capacitance. Both  $V_{ap}(t)$  and either  $i(t)$  or  $q_{ext}(t)$  data are normally centered around the y-axis before further analysis. The procedure and significance of this adjustment is discussed in the literature [96, 97].

One of the common analytical techniques for the characterization of ACTFEL devices which uses the above information is known as external charge-applied voltage, or Q-V, analysis. Figure 2.18 shows schematically the behavior typical of a ZnS:Mn device, sometimes referred to as an “ideal” device. The A-J labeling scheme from Figure 2.17 is included in Figure 2.18. The conduction charge and polarization charge, discussed for the simplified device, are still seen in Figure 2.17. The two new features are the relaxation charge and leakage charge. Relaxation charge occurs when the applied voltage reaches its maximum value (or near maximum value in a real case) and reflects current which flows during the dwell, or C-D portion of the waveform [98]. The name refers to the fact that at a constant applied voltage, conduction charge creates an opposing electric field that relaxes the field across the phosphor layer. Along the falling edge of the voltage pulse, the charge decreases linearly (segment DE). There is a leakage charge ( $Q_{\text{leak}}$ ) transported during the period when the voltage is zero between the pulses of opposite polarity (segment EF). This is typically assigned to electrons escaping from shallow interface states. Assuming a symmetric device, the features on the Q-V loop from F to J are equivalent to those described above from A to F, except the voltage pulse is of the opposite polarity. The final undefined term from figure 2.18 is  $Q_{\text{cond}}$ , the conduction charge transferred across the phosphor at voltages above threshold. This charge is responsible for light emission from impact excitation of the luminescent centers [55]. The power dissipated in a device, which is proportional to the area inside the curve, can be used as expressed above to define the power efficiency of the device. Obviously, low power and high power efficiency are both highly desirable traits for commercial applications.

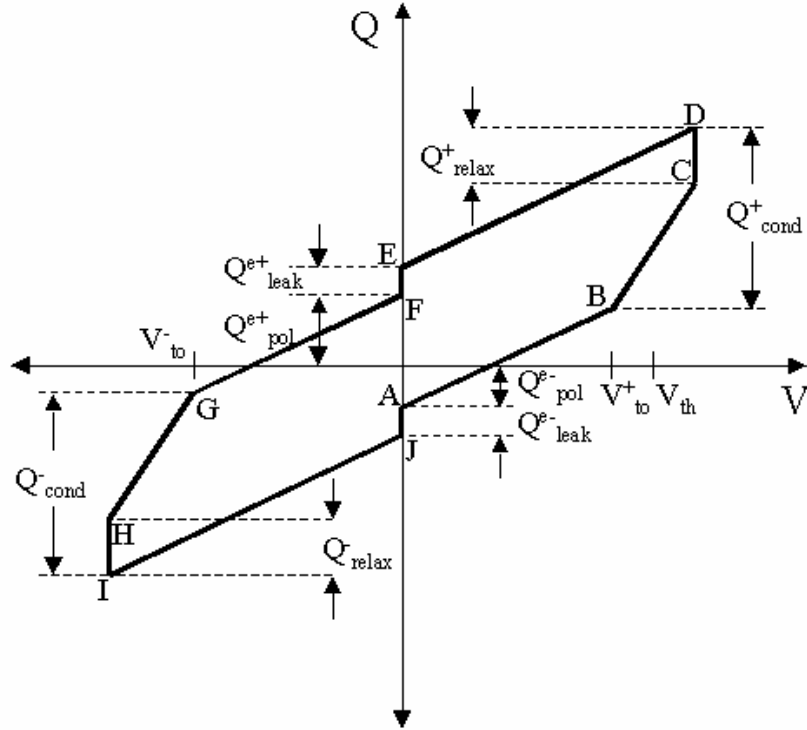


Figure 2.18 Schematic diagram of the Q-V characteristics of an ACTFEL device ( $V_{to}$ : electrical turn-on voltage,  $Q_{cond}$ : conduction charge,  $Q_{pol}$ : polarization charge,  $Q_{leak}$ : leakage charge,  $Q_{relax}$ : relaxation charge). Letters refer to the labeling scheme in Figure 2.17.

As mentioned previously, the value of interest is often the internal or conduction charge and/or current. This value is denoted  $q_{int}(t)$ , or just  $q(t)$ , and is found from

$$q(t) = \frac{(C_i + C_p)}{C_i} C_s v_3(t) - C_p [v_2(t) - v_3(t)] \quad (2.29)$$

where  $C_i$  and  $C_p$  are the phosphor and insulator capacitances, respectively. It is important to note that (1) this assumes accurate values for  $C_i$  and  $C_p$  are known, and (2) this analysis (as well as data obtained using the balanced bridge circuit) assumes that the device capacitance does not change above threshold.

Another value of interest is the phosphor field,  $f_p$ , rather than just the applied voltage. This is also found using the transferred charge and applied voltage data by the relation

$$f_p(t) = \frac{1}{d_p} \left\{ \frac{C_s v_3(t)}{C_i} - [v_2(t) - v_3(t)] \right\} \quad (2.30)$$

where  $d_p$  is the phosphor thickness. Note that the determination of this value requires the knowledge of accurate values for the phosphor thickness and insulator capacitance.

The internal charge plotted against phosphor field, or  $Q_{\text{int}}-F_p$ , can be used to examine various properties of the device such as extent of field clamping and field relaxation. A schematic  $Q_{\text{int}}-F_p$  diagram is given in Figure 2.19, which shows some of the values that can be obtained from this type of plot. Note that unlike a Q-V plot, the  $Q_{\text{int}}-F_p$  plot occurs in a counterclockwise fashion. Also, the values of the insulator and phosphor capacitance are often used as parameters to obtain the most “ideal” shape, meaning vertical slopes for the B-C and G-H portions of the curve and horizontal slopes for the D-E and I-J portions of the curve. One interpretation of the capacitance adjustment has been that a larger capacitance value used for the  $Q_{\text{int}}-F_p$  plot compared to the physical value, which is calculated from the layer thickness and dielectric constant, refers to a larger amount of space charge [99].

Another type of electrical analysis commonly used to characterize ACTFEL devices is called a dynamic capacitance-voltage, or C-V plot [100, 101]. Using the same  $q^{\text{ext}}(t)$  or  $i^{\text{ext}}(t)$  data and  $V_{ap}(t)$  data collected under steady state excitation, the dynamic capacitance is found from the charge or current data by

$$c(v) = \frac{dq_{ext}(t)}{dv(t)} \quad (2.31)$$

or

$$c(v) = \frac{i(t)}{\left(\frac{dv(t)}{dt}\right)} \quad (2.32)$$

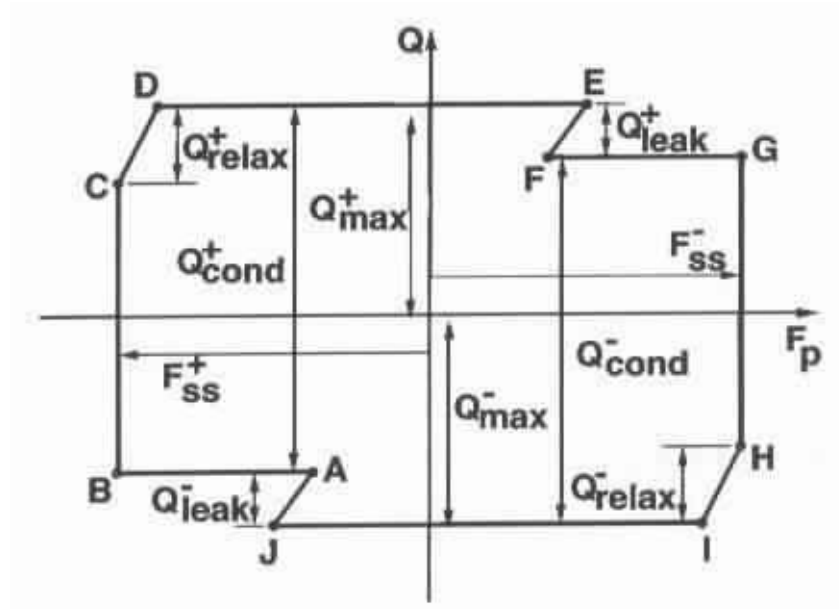


Figure 2.19 Schematic diagram of an idealized  $Q_{int}$ - $F_p$  plot ( $F_{ss}$  : steady state phosphor,  $Q_{cond}$  : conduction charge,  $Q_{pol}$  : polarization charge,  $Q_{leak}$  : leakage charge,  $Q_{relax}$  : relaxation charge). Letters refer to the labeling in Figure 2.17.

A schematic set of C-V curves is shown in Figure 2.20, representing 3 different values of  $V_{max}$ . Below threshold the capacitance value represents the total device capacitance and there is usually good agreement with the physical value calculated from the layer thicknesses and dielectric constants [46]. In the simple device model discussed in Section 2.6.2 and shown in figure 2.15, the above threshold capacitance would equal that of the insulators, while in reality there are three possible cases. If there is insufficient charge to shunt the phosphor capacitance, then the above threshold capacitance value will be below that of the insulator capacitance. If there is sufficient charge available and no

dynamic space charge, then the dynamic capacitance will be approximately equal to the insulator capacitance. However, if there is dynamic space charge, the above threshold C-V behavior will saturate to a value above the insulator capacitance. This is sometimes seen by a rapid increase in capacitance to a large value followed by a decrease to a value greater than the insulator capacitance.

Another useful tool to characterize the electrical properties of an ACTFEL device is a maximum charge-maximum voltage analysis, also known as a  $Q_{\max}$ - $V_{\max}$  or transferred charge capacitance plot. The last name alludes to the fact that the units for the slope of a  $Q_{\max}$ - $V_{\max}$  plot are Farads, and therefore can be analyzed in the context of the capacitive nature of the device. This type of plot is obtained by measuring the transferred charge in a device for a range of applied maximum voltages. The internal charge is then determined from the external values by any of the means discussed previously and plotted vs. maximum voltage. The behavior of the ideal circuit in Section 2.6.2 is shown schematically in Figure 2.21. The critical issues in a  $Q_{\max}$ - $V_{\max}$  plot are similar to the C-V plot in that the above threshold capacitance should equal the insulator capacitance for an ideal device. For a case in which there is insufficient conduction charge, the slope is less than the insulator capacitance. More often there is an above threshold capacitance overshoot. In evaporated ZnS:Mn there is a higher slope just above threshold, which then saturates to the approximately the insulator capacitance. On the other hand in SrS:Ce the above threshold slope is consistently larger than the insulator capacitance, as demonstrated by Wager and Keir [46].

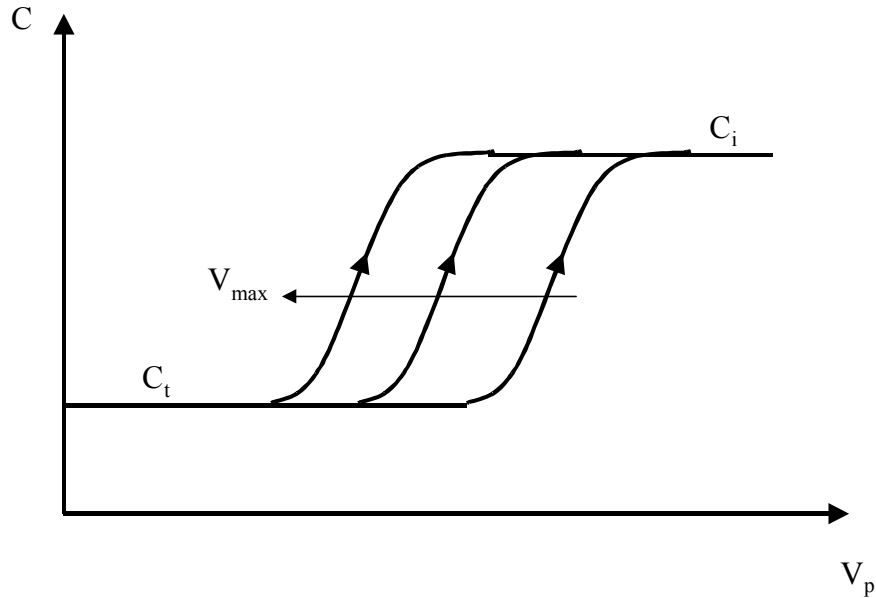


Figure 2.20 Schematic diagram of a C-V plot for three different values of  $V_{\max}$ .

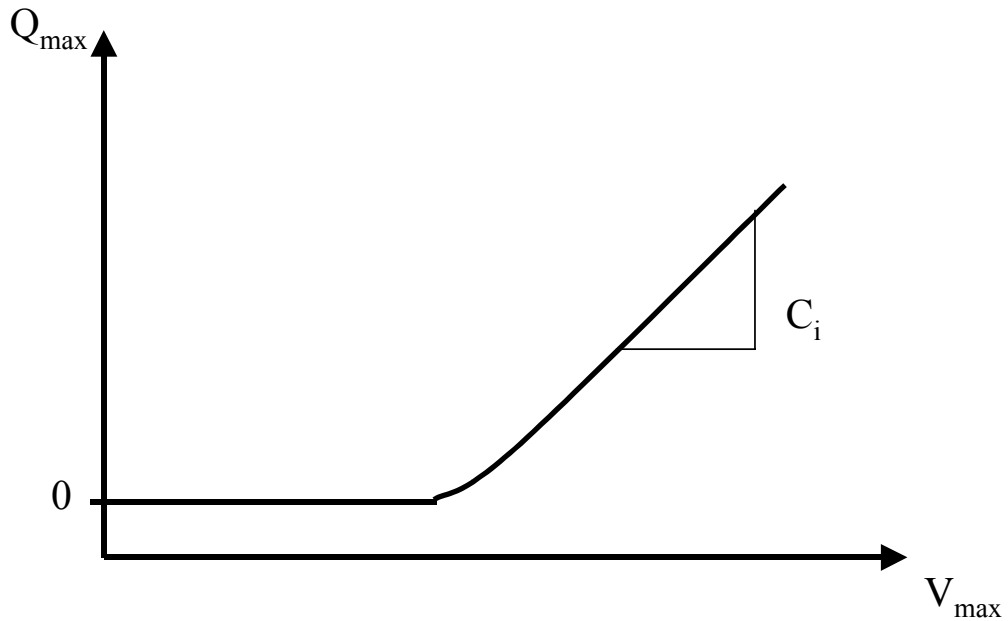


Figure 2.21 Schematic diagram of  $Q_{\max}$ - $V_{\max}$  plot for an ideal device.

### 2.7 ZnS:NdF<sub>3</sub> and ZnS:ErF<sub>3</sub> as ACTFEL phosphors

ZnS:Nd<sub>3</sub> has orange emission at 602 nm ( ${}^4G_{5/2} \rightarrow {}^4I_{9/2}$ ) and infrared emissions at 892 nm ( ${}^4F_{3/2} \rightarrow {}^4I_{9/2}$ ) as shown in Figure 2.22 [30]. It also has infrared transitions at 1060 nm ( ${}^4F_{3/2} \rightarrow {}^4I_{11/2}$ ), 1340 nm ( ${}^4F_{3/2} \rightarrow {}^4I_{13/2}$ ) and 1800 nm ( ${}^4F_{3/2} \rightarrow {}^4I_{15/2}$ ) [84]. Of all the rare earth

phosphors, Nd has the most intense infrared signal. This starting lower energy state ( $^4F_{3/2}$ ) should be more heavily excited in a host like ZnS because of the scattering of hot electrons by the low-lying states in ZnS [102].

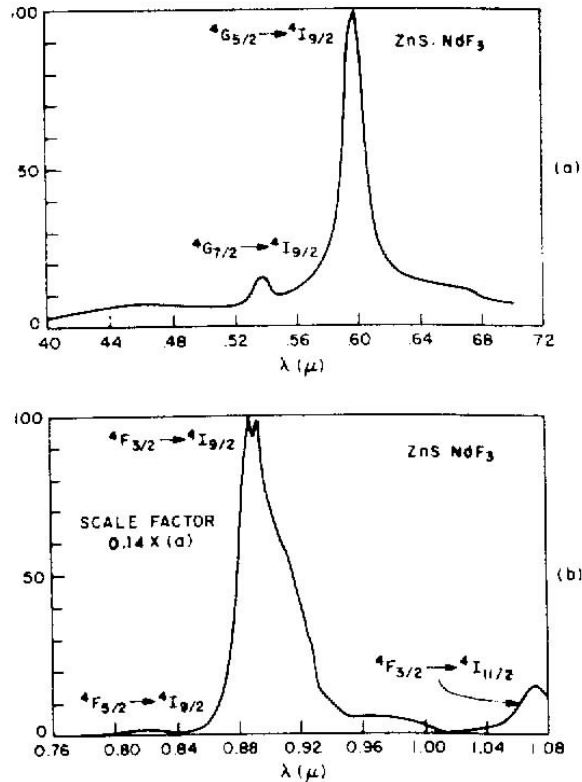


Figure 2.22 Spectrum of ZnS:NdF<sub>3</sub> [30].

Zn:Er<sub>3</sub> has green emission at 525 nm ( $^2H_{11/2} \rightarrow ^4I_{15/2}$ ) and 548 nm ( $^4S_{3/2} \rightarrow ^4I_{15/2}$ ), red emission at 662 nm ( $^4F_{9/2} \rightarrow ^4I_{15/2}$ ) and a near infrared emission at 985 nm ( $^2F_{7/2} \rightarrow ^4I_{11/2}$ ) as shown in Figure 2.23 [30]. It is well known that Er<sup>3+</sup> ions exhibit atomic-like, temperature stable luminescence at 1.54 $\mu$ m due to the intra-4f-shell Er<sup>3+</sup> transition ( $^4I_{13/2} \rightarrow ^4I_{15/2}$ ). Since the 1.54 $\mu$ m emission from Er<sup>3+</sup> overlaps the minimum absorption region of silica based optical fibres [103], Er doped semiconductors are suitable light sources for applications in optical communications. Recent studies have indicated that the Er<sup>3+</sup> luminescence intensity at room temperature is strongly influenced by the band gap of the semiconductor host. It was found that semiconductors with larger band gap, exhibit less

temperature quenching of  $\text{Er}^{3+}$  luminescence[104]. Consequently, research efforts have shifted towards  $\text{Er}^{3+}$  doped wide band gap semiconductors[28, 29, 104-106]. Dielectric thin films of different Er-doped materials can be used to fabricate planar optical amplifiers or lasers that can be integrated with communication systems [107-109]. The ratio of the visible and IR emission intensities depend on the host material type and Er concentration [110].

Keir *et al.* [102] have studied the differences between ZnS and SrS as host materials and reached a conclusion that SrS appears to be a superior high-field electron transport materials as compared to ZnS. Hence, ZnS does not appear to be a viable ACTFEL phosphor for blue color applications since its hot electron distribution appears to be inadequately heated to efficiently excite short wavelength impurities and that proves to be beneficial for good infrared emission. Georgobiani *et al.* [85] have investigated infrared emission for  $\text{Er}^{3+}$  in thiogallates and seen intense  $1.54\mu\text{m}$  emission from these materials. Polman [111] has suggested that in oxides, because of their large phonon energy, the multiphonon relaxation of the excited electrons to the lower levels gives rise usually to infrared and red emission.

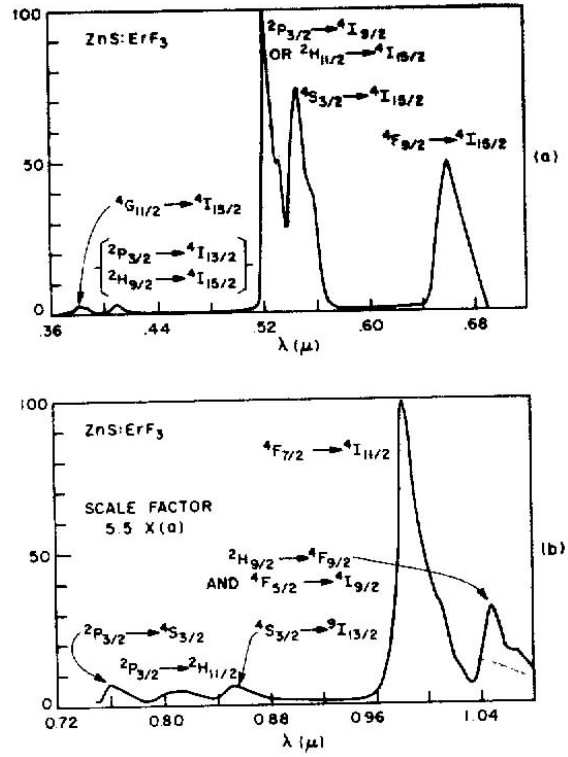


Figure 2.23 Spectrum of ZnS:ErF<sub>3</sub>[30].

## CHAPTER 3 EXPERIMENTAL PROCEDURE

### 3.1 Introduction

In this section, the conditions and procedures for sputter deposition of ZnS:LnF<sub>3</sub> (Ln: Nd,Er) thin films and characterization will be discussed. Methods to characterize optical, microstructural, compositional, and electrical properties are used in this study.

### 3.2 ACTFEL Device Fabrication

#### 3.2.1 Substrate Materials

Corning 7059 glass substrates, 0.04 inch thick, coated with 360nm indium tin oxide (90wt%In<sub>2</sub>O<sub>3</sub> + 10wt% of Sn<sub>2</sub>O<sub>3</sub>(ITO)) as a transparent conducting electrode and 160nm aluminum titanium oxide (Al<sub>2</sub>O<sub>3</sub>/TiO<sub>2</sub>(ATO)) as bottom insulator layer, were supplied by Planar Systems. The bottom dielectric layer (ATO) was deposited using atomic layer deposition (ALD) to ensure a good quality insulator. The ITO is crystalline in nature whereas the ATO is amorphous. Each substrate is cleaned by using ultraviolet (UV) photons in air (which generates ozone) for approximately 6 minutes before deposition to get rid of any hydrocarbon contamination on the substrate surface.

#### 3.2.2 Thin Film Deposition

ZnS:LnF<sub>3</sub> thin films (where Ln = Nd, Er) were deposited onto the ATO/ITO/7059glass substrates by R.F. planar magnetron sputtering to a layer thickness of 1μm ±10%. Figure 3.1 shows a schematic of the sputter deposition system. The sputter deposition system houses 3 RF-magnetron sputter guns, which enable co-sputter deposition of additional doping elements from separate targets. Three different targets

were used for this study, namely pure ZnS, ZnS doped with NdF<sub>3</sub> and ZnS doped with ErF<sub>3</sub>. All sputter targets are 2” in diameter and ¼” thick. The thin film composition can be changed by altering the duty cycles of the power applied to each target. The duty cycles vary between 0 – 100% on each target. The substrate holder has the capacity to hold four 2 × 2” substrates or eight 1 × 2” substrates. The substrate holder rotates at a constant speed driven by a stepping motor and in this study, the rotation speed is held constant at 8s/revolution. The substrates may be heated to a temperature of 300°C utilizing carbon fiber heater elements. Samples to be coated are introduced into the deposition system through a load lock which is pumped down to 10mTorr by a wet rotary vane pump (Leybold Trivac D65B) through a right angle valve. The main chamber is evacuated using a turbomolecular pump (Leybold Mag1600) backed by the rotary vane roughing pump. An ultimate pressure  $< 1 \times 10^{-6}$  Torr can be achieved in this chamber for deposition. The system is capable of using ultra high purity O<sub>2</sub> as well as ultra high purity Ar gas as sputtering media. For this study we used only Ar gas. The sputtering gas pressure is controlled by the gas flow rate and a throttle valve, which is installed between the main chamber and the turbomolecular pump. A number of gauges installed on the system allow us to monitor the pressure in various regions of the system. Thermocouple gauges are used to measure pressures in the foreline and the loadlock, whereas an ionization gauge measures the pressure in the main chamber. The capacitance manometer (Baratron gauge) monitors the Ar gas pressure during deposition and is kept at a value of 20mTorr for this study. The target to substrate distance is about 5cm.

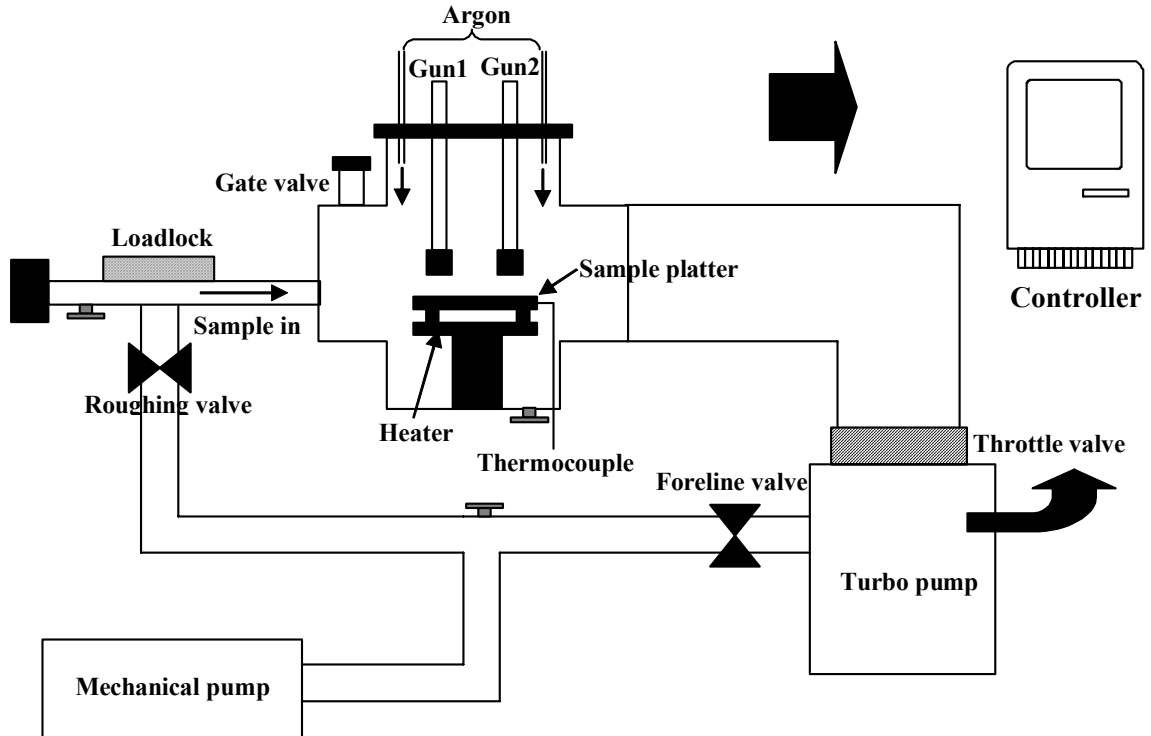


Figure 3.1 Schematic of the sputtering system used for RF planar magnetron deposition of ZnS:Er/NdF<sub>3</sub> thin films.

### 3.2.3 Post-Deposition Annealing

Sputter deposited films are annealed using halogen lamps, which are cooled by nitrogen and water. A schematic of the annealing furnace is shown in Figure 3.2. Halogen lamps located above and below a quartz tube provide the necessary heat. The quartz tube is purged with ultra high purity (99.9999%) N<sub>2</sub> gas for approximately 45 minutes before the lamps are turned on. Typical annealing temperatures used in this study range from 300° - 475°C and the annealing time is 60minutes. The N<sub>2</sub> purge continues during the annealing treatment and cool down period of 30 min after the anneal. The samples are either placed in a graphite susceptor or on a silicon wafer, which are placed in the middle of the quartz tube. A thermocouple is placed on a dummy glass sample or on the underlying silicon to measure the actual sample temperature during annealing. The annealing cycle is controlled by a Micristar controller which allows selection of a suitable

ramp up and down profile. A typical ramping time to 425°C is 90 seconds and the cooling time to 300C is ~60 sec but cooling to <80°C requires ~ 30 minutes.

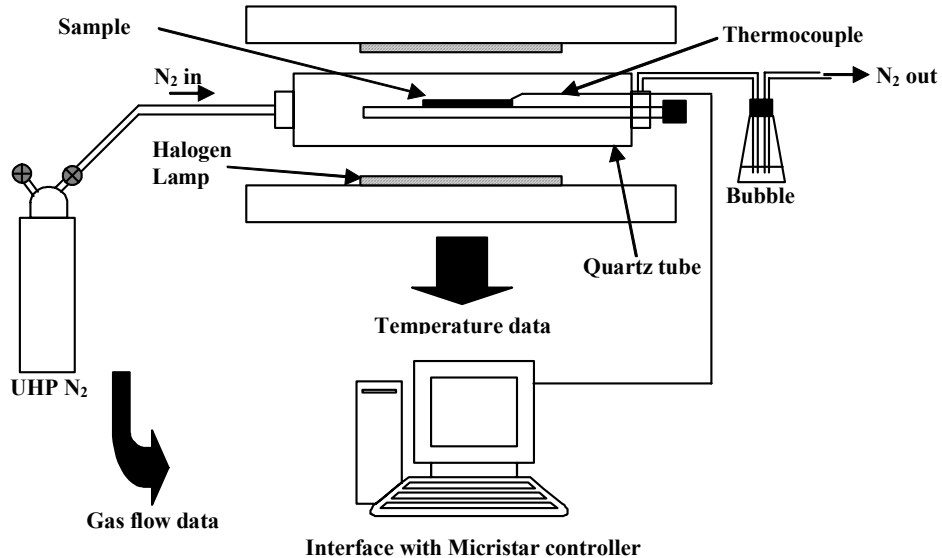


Figure 3.2 Schematic of the “rapid thermal anneal” furnace showing lamps as heaters.

### 3.2.4 Electrode Deposition

Electrodes are required on either sides of the phosphor to apply an electric field across the device. The bottom electrode (ITO) is already deposited on the as received substrates. The top electrode (Al) is deposited by thermal evaporation through a circular shadow mask that has a diameter of 2.5 mm and a typical thickness is 230nm. Electrical contact to the ITO is achieved by scratching through the ATO layer with a diamond scribe and then melting pure indium onto the scratched surface. The molten indium wets the bottom ITO electrode for electrical contact.

### 3.3 Characterization

#### 3.3.1 Thickness Measurement

Before deposition, one side of the ITO/ATO substrate is covered with a microscope glass slide to create a step in the deposited film. Film thickness is measured by running the tip of a Tencor (Alpha-Step 500) profilometer across this interface at different areas and an average value is taken as the film thickness.

#### 3.3.2 Electroluminescence (EL) Measurement [46]

Optical properties such as brightness, chromaticity and emission spectrum are routinely measured for all the deposited films. EL emission was excited by applying 2.5 kHz positive and negative trapezoidal voltage pulses, 30 $\mu$ s and 5 $\mu$ s in length with 5 $\mu$ s rise and fall times. The typical ac trapezoidal pulse used to drive the ACTFEL devices is shown in Figure 3.3. The emitted light is analyzed with an Oriel MS257 0.25m monochromator using reflective optics. A chopper and lock-in detection scheme is used to improve the signal to noise ratio. A Si-based photomultiplier tube (PMT)(Oriel instruments, model 77345) attached to one of the exit ports on the monochromator was used to detect light up to 0.8 $\mu$ m, and a thermo-electric cooled Ge photodiode (Oriel instruments, model 71614) on a second exit port was used to detect light with wavelengths up to 2 $\mu$ m. An Oriel Merlin radiometry system controlled the chopper and was used to interface the monochromator and detectors with the acquisition software. The setup for the optical bench is shown in Figure 3.4.

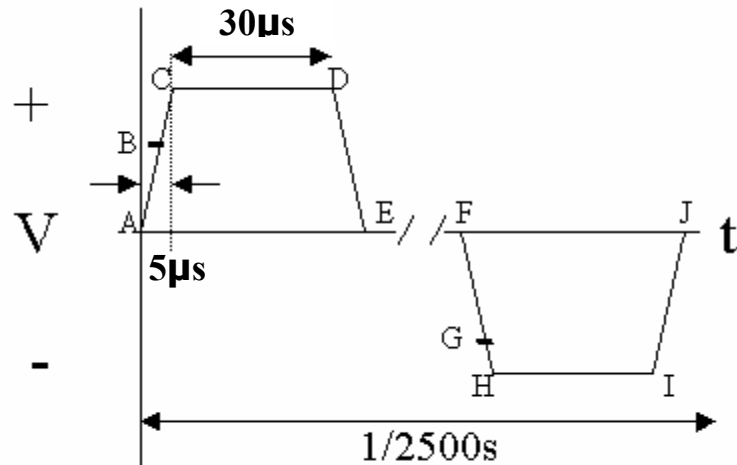


Figure 3.3 Typical commercial ACTFEL device driving waveform.

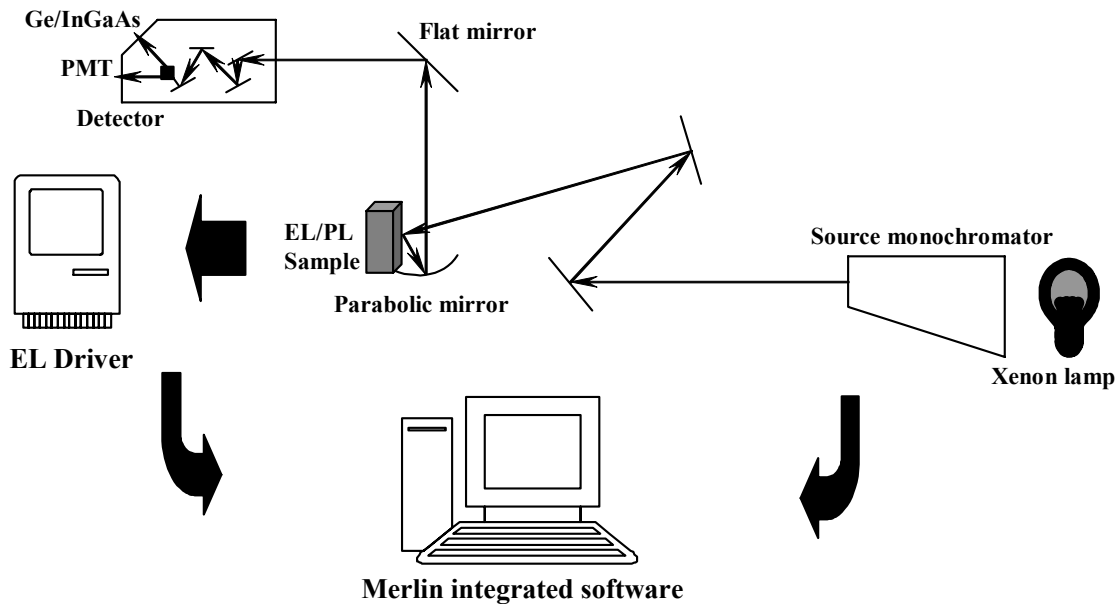


Figure 3.4 Optical bench setup for measuring EL and PL from ACTFEL.

The spectrometer was calibrated using a Oriel model 63358 QTH calibrated lamp. The calibrated lamp is traceable to NIST standards in the 200-2400nm range. Irradiance was provided in this range at a distance of 50cm from the source, through a  $1\text{cm}^2$  aperture.

Using proper protocols for the minimization of reflected light, the standard was placed at 50cm from the sample position and its spectrum measured using fixed optics

and monochromator settings. That is, a known irradiance value was produced at the sample position. This measurement provided a curve with the physical meaning ‘irradiance per unit response’ [ $\mu\text{W}/\text{cm}^2 \cdot \text{V}$ ] which in fact is a correction curve. The irradiance of EL devices was obtained by measurement using the exact sample position, fixed optics and monochromator settings as those used for the determination of the calibration curve. Irradiance is then obtained simply by multiplying the measured spectrum [V] by the calibration curve.

### 3.3.3 Photoluminescence (PL) Measurement [112]

A Xenon lamp was used for the excitation source for PL. The excitation wavelength is selected with a source monochromator (Oriel Instruments, Cornerstone 260) between the lamp and the sample. The monochromator is capable of selecting wavelengths ranging from 200 nm to 1200nm. PL measurements are carried out at room temperature in a dark room. The emission spectrum is collected from 300nm to 1800nm utilizing suitable detectors and monochromators (Oriel Instruments, MS257).

### 3.3.4 X-ray Diffraction (XRD)

X-ray diffraction gives information about the quality of a material, specifically the type and quality of the crystalline structure of the material under investigation. For this study a Philips APD 3720 x-ray diffractometer was used with a  $\text{Cu K}\alpha$  wavelength of  $1.54\text{\AA}$  generated with a 40keV, 20mA electron beam. The x-rays are diffracted according to Bragg’s law such that

$$n\lambda = 2d\sin\theta \quad (3.1)$$

where  $n$  is an integer,  $\lambda$  is the wavelength of the incident x-ray,  $d$  is the spacing of the (hkl) plane and  $\theta$  is the angle between the incident and detection directions and the surface normal. Data were collected for  $2\theta$  from  $25^\circ$  to  $65^\circ$  at a scan rate of  $0.05^\circ/\text{sec}$ .

Since the major ZnS peak lies at around  $28.5^\circ$ , a scan range of  $27^\circ$  to  $30^\circ$  at a scan rate of  $0.005^\circ/\text{sec}$  was selected for determination of the full width half maximum (FWHM), a measure of crystalline quality. Important information such as crystallographic orientation, crystallite size and internal stresses can be obtained from the diffraction peak width and shape [113]. In single crystal samples, the intensity would be a very narrow, intense peak, whereas for a thin film sample, broad peaks are recorded indicative of small crystallite size and strain in the lattice.

### 3.3.5 Transmission Electron Microscopy (TEM)

For Transmission Electron Microscopy (TEM) [112] a high energy electron beam (200keV in this case) is used to image the sample. The optics consist of a series of lenses housed in a central column capable of focusing an electron beam down to a very small spot size. This electron beam then passes through the sample and the image is produced on the underlying phosphor screen. To facilitate transmission of electrons, the sample has to be extremely thin ( $<100$  nm) by careful preparation. TEM may be used to produce either images of the material or producing electron diffraction patterns which identify the crystal structure and orientation of the sample. In the case of ACTFEL devices cross-section TEM (XTEM) samples are required to examine the thin film interface and its structure.

To prepare a XTEM sample, it is first cut into thin strips and two strips with the films facing each other were joined together with G1 bond. The glue between the strips is cured to achieve proper bonding and the sample checked for any air bubbles. These strips are then cut into several small pieces ( $2\text{mm} \times 1.5\text{mm}$ ) using a slow speed diamond saw. The samples are then mounted on an aluminum block and polished on a rotating Gatan

grinder wheel using progressively smaller grit papers (400,600 and 1200 grit). The sample is thinned to approximately 100  $\mu\text{m}$ , at which the sample edges are almost invisible. The samples are removed and mounted on a hollow copper grid to give them support during the subsequent processing steps. The above-mentioned processing steps are shown in the Figure 3.5.

Once the sample is mounted onto the copper grid (for support while handling), it is ready for dimpling. Dimpling is carried out using an 8  $\mu\text{m}$  grit slurry and the sample was thinned down to about 50  $\mu\text{m}$ . Thinner sample are desired for easier ion-milling. For ion milling, two guns operating at 6kV and 1mA, with the sample rotating continuously, are used until a hole at the glue line is observed. The angle for milling is set at 18° for this step. Once a hole is seen, the angle is reduced to 12° and the sample milled for an additional 30 minutes to get a progressive thinner cross section around the hole. The sample is then checked with an optical microscope for optical interference fringes which indicate the size of the thinned area and smooth surfaces. For better results, the sample is coated with carbon before placing inside the TEM.

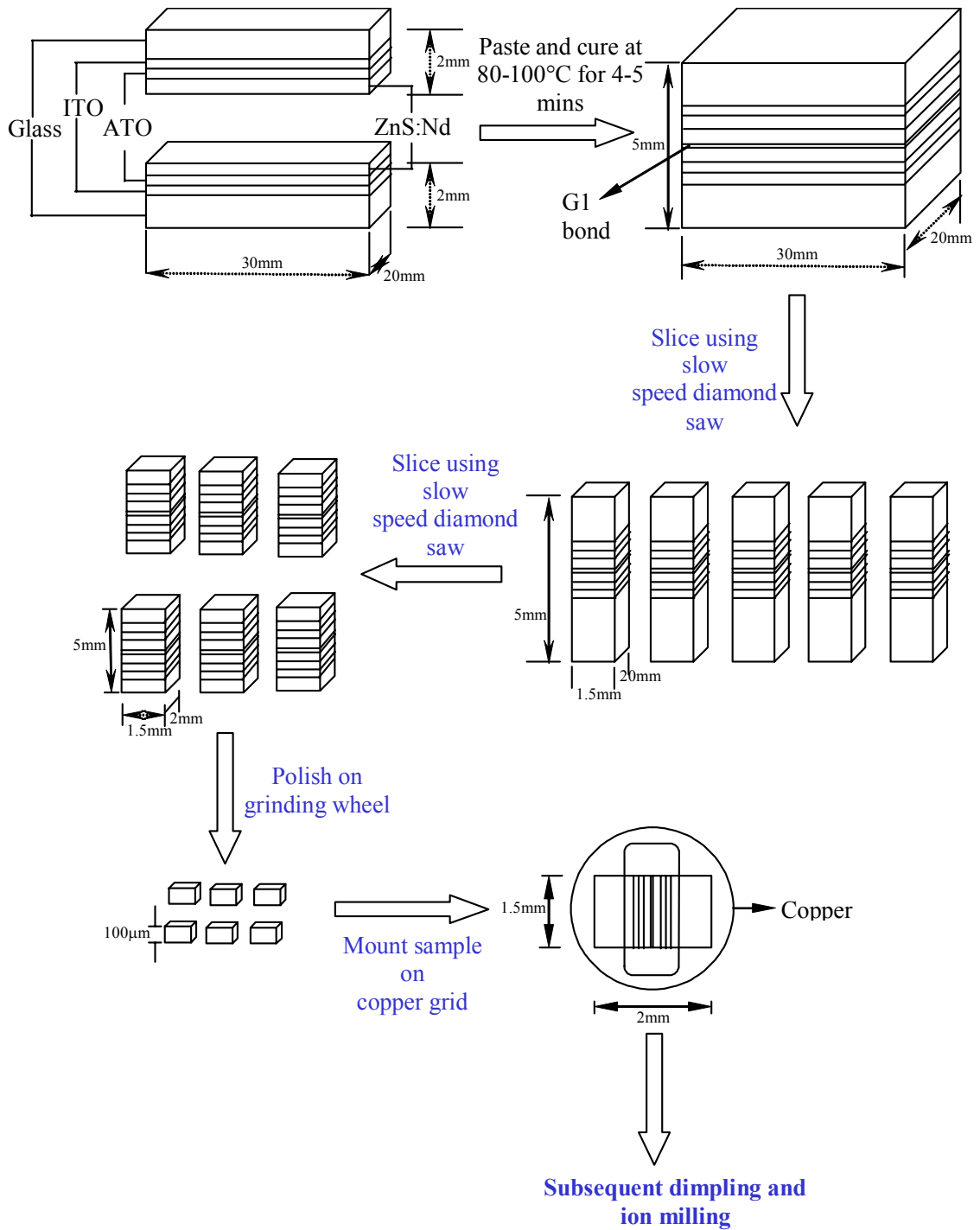


Figure 3.5 XTEM sample preparation technique.

### 3.3.6 Atomic Force Microscopy (AFM)

Surface roughness and morphology are characterized by using atomic force microscopy using a Digital Instruments Nanoscope III in the tapping mode (1 to 3hz). A

schematic of the AFM is shown in Figure 3.6, which shows a sharp tip mounted on a flexible cantilever. As the tip comes within a few Å of the samples surface, repulsive van der Waals forces between the atoms on the tip and the surface cause the cantilever to deflect. The magnitude of this deflection depends upon the tip to sample distance  $d$ . The most common detection system for monitoring the deflection is the beam bounce detection system. In this system, light from a laser diode is reflected from the back of the cantilever onto a position sensitive photodiode (PSD). A given cantilever deflection corresponds to a specific position of the laser beam on the position sensitive photodiode. The PSD can detect displacements of the order of  $0.1\text{Å}$ .

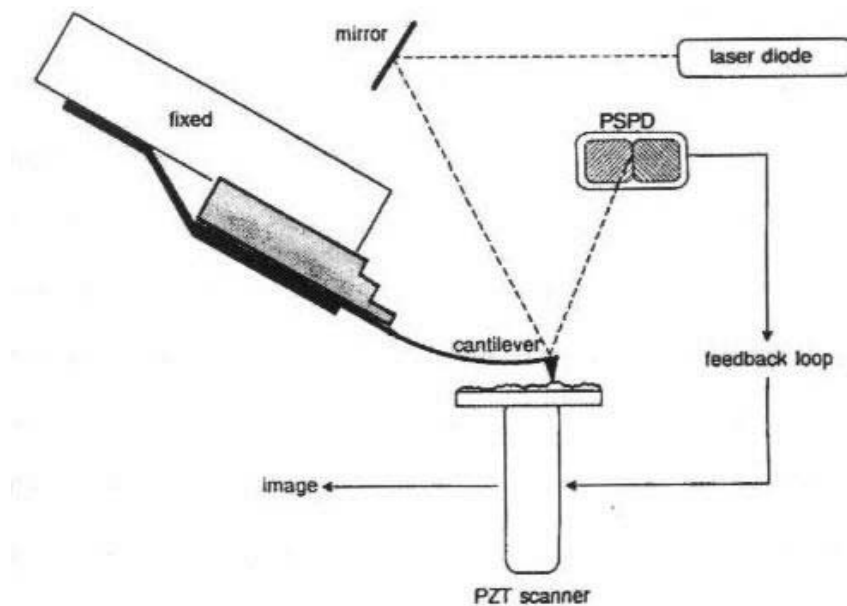


Figure 3.6 Schematic of an Atomic Force Microscope. Piezoelectric scanner scans tip across sample and the feedback loop maintains constant separation between the tip and the sample.

### 3.3.7 Electron Probe Micro Analysis (EPMA)

Electron probe x-ray microanalysis (EPMA) is a spatially resolved, quantitative elemental analysis technique based on the generation of characteristic x-rays by a focused beam of energetic electrons [114-116]. A high energetic beam of electrons is

used to eject core level electrons from the constituent atoms of the material. The ejected core electron leaves an electron vacancy which can be filled by an electron from a higher level electron and the energy difference emitted as an x-ray. The emitted x-rays have an energy that is characteristic of the parent atom. The concentration of the atomic species is proportional to the number of x-rays emitted. EPMA is used to measure the concentration of elements (beryllium to the actinides) at levels as low as 100 parts per million (ppm) with determination of the lateral distributions through mapping.

In x-ray spectroscopy, the wavelength and intensities of characteristic x-rays generated from the specimen due to electron bombardment are used as information. The EPMA uses linear focusing spectrometers to determine the energy of the x-rays [115]. Since the x-ray take-off angle in the spectrometer is fixed, the effect of absorption and unevenness of the specimen is constant. Furthermore, the geometry of the spectrometer ensures high x-ray intensities, P-B ratio, wavelength resolution, etc.

### 3.3.8 Electrical Characterization

A detailed review of the electrical characterization was given in section 2.6.1.2. As mentioned, we use an applied voltage called the threshold voltage, defined as the intersection on voltage axis of the extrapolation of the maximum linear slope of the B-V curve. The applied voltage is the 2.5kHz trapezoidal pulses (5 $\mu$ s rise time, 30 $\mu$ s dwell time, 5 $\mu$ s fall time) as described in section 3.3.2. A Tektronix TDS 510A digitizing oscilloscope is used to measure the voltage at each point indicated as  $V_1$ ,  $V_2$  and  $V_3$  as shown in Figure 2.15. The current passing through the EL device can then be calculated by dividing the voltage across the sense resistor by the series resistance, such that

$$i(t) = \frac{V_2(t) - V_1(t)}{R_{\text{series}}} \quad (3.2)$$

where  $R_{\text{series}}$  is the series resistance ( $128\Omega$ ). The external charge ( $Q_{\text{ext}}(t)$ ) is determined by integrating the current over time as described in section 2.6.2.2.

To measure the time dependence on the luminescence (decay data), luminance versus time is collected by connecting the Tektronix TDS 510A digitizing oscilloscope to a Si-diode photomultiplier tube (PMT manufactured by Oriel instruments) whose output current is measured across a  $1\text{K}\Omega$  bridge resistor. Electrical data as well as the time decay data are collected from both the aluminum and the ITO electrodes under both positive and negative voltage polarities.

CHAPTER 4  
RF MAGNETRON SPUTTER DEPOSITION OF ZINC SULFIDE DOPED WITH  
NEODYMIUM ACTFEL DEVICES

4.1 Introduction

Sputtered films have a lot of point defects. Point defects alter the phosphor field and are responsible for increased inelastic scattering which negatively affects the number of electrons which become sufficiently hot and cause luminescence. This in turn negatively affects the excitation efficiency. Point defects also create non-radiative recombination pathways which are in direct competition with radiative pathways and therefore reduce the radiative efficiency [finally trap charge and bend electric field]. Hence it is important to minimize the number of point defects to achieve good luminescence. Annealing helps remove defects and also improves dopant activation. This chapter describes the effect of post-deposition annealing treatment on the electrical and optical characteristics of RF magnetron sputtered ZnS doped NdF<sub>3</sub> ACTFEL devices. To begin with, a description of the experimental procedure is given. This is followed by a summary of the various structural, optical and electrical characterization methods. The purpose of this study was to investigate how and why annealing up to a certain optimum annealing temperature improved EL device characteristics.

4.2 ACTFEL Device Efficiency

Device efficiency is one of the main properties required to quantify the performance of an ACTFEL device. The improved performance can best be quantified in terms of device efficiency keeping in mind the factors which contribute to device

efficiency and which may be facilitated by post-deposition annealing. Therefore a more detailed discussion of device efficiency is warranted.

Following the approach taken by Mach and Mueller [59], the most useful definition for device efficiency in terms of analyzing device processes is of the form

$$\eta = \frac{\text{photon flux} \left[ \frac{\text{photons}}{\text{cm}^2 \text{s}} \right]}{\text{transferred charge} \left[ \frac{\text{electrons}}{\text{cm}^2 \text{s}} \right]} \quad (4.1)$$

The total device efficiency is a product of three different efficiencies as mentioned above.

That is,

$$\eta = \eta_{exc} \eta_{rad} \eta_{out} \quad (4.2)$$

with each term related to a primary physical process involved in ACTFEL device operation. More specifically,  $\eta_{exc}$  is the efficiency related to the fraction of luminescent centers brought to an excited state by ballistic charge carriers, or

$$\eta_{exc} = \frac{\text{\# of centers excited} [\text{cm}^{-3}]}{\text{\# of above threshold energy electrons} [\text{cm}^{-3}]}, \quad (4.3)$$

$\eta_{rad}$  is the radiative efficiency of excited centers, or

$$\eta_{rad} = \frac{\text{\# of centers decaying radiatively} [\text{cm}^{-3}]}{\text{\# of centers excited} [\text{cm}^{-3}]} \quad (4.4)$$

and  $\eta_{out}$  is the outcoupling efficiency of photons generated in the phosphor layer, or

$$\eta_{out} = \frac{\text{\# of photons exiting the device} [\text{cm}^{-3}]}{\text{\# of photons generated within the device} [\text{cm}^{-3}]} \quad (4.5)$$

Each of these terms will be discussed with respect to the possible mechanisms responsible for the increased irradiance and/or efficiency of the devices, observed with annealing. Note that both  $\eta_{exc}$  and  $\eta_{opt}$  are related to the phosphor thickness. This is an

additional source of complications when there is a significant change in the phosphor layer thickness and uniformity. In the present study, samples that are compared directly are always taken from the same sputter run.

#### 4.2.1 Optical Outcoupling Efficiency

The probability that emitted photons will escape the thin film stack in the direction of the viewer is defined as the outcoupling efficiency. As the internal reflection of photons at the top and bottom surface increases, the outcoupling efficiency decreases. Internal reflection is due to the difference between the absolute values of the index of refraction of the phosphor and the dielectric layer, as well as the interface roughness (section 2.4.5). By reducing the index of refraction of the phosphor layer, which is normally larger than the index of the insulating layer, the outcoupling efficiency can be improved. [This is a point of contention. It is a constant for similarly processed materials. You are comparing as-deposited with annealed samples and the polarizability might be different].

Increased surface roughness may also reduce internal reflection resulting in improved optical outcoupling. The phosphor roughness is typically measured using AFM (atomic force microscopy). Interface roughness can be present at the phosphor/insulator, glass/air and insulator/glass interfaces. However, the glass/air interface is constant and insulators such as  $\text{Al}_2\text{O}_3$  ( $n=1.63$ ) are better matches to the index of glass ( $n=1.53$ ). Therefore, internal reflection is mostly affected by the phosphor/insulator variability.

Another technique to quantify internal reflection is diffuse reflectance measurement. The variation in diffuse reflectance values between the as-deposited and the annealed samples gives a direct measure of their outcoupling efficiency.

#### 4.2.2 Excitation and Radiative Efficiency

The analysis of excitation efficiency is not as straightforward as the other processes. Excitation efficiency refers to the ratio of the number of luminescent ions, in this case Nd\*, brought to an excited state, to the number of electrons above the energy threshold for excitation transported from the momentary cathodic phosphor/insulator interface to the anodic interface. Following the procedure outlined by Zeinert et al. [88,117], the relative excitation efficiency can be experimentally approximated. The essence of Zeinert's approximation is that the initial brightness of the phosphor after an excitation pulse is proportional to the number of excited states generated during that pulse when the pulse duration is much shorter than the decay time [You might want to think about /explain those decay times you use that are shorter than the 5microsecond excitation] so that the extent of de-excitation is negligible. Thus the following relationship can be used:

$$\eta_{exc} = \frac{\text{conc. excited centers}}{\text{no. electrons transported}} \propto \frac{B_{\max}}{Q_{\text{int}}} \quad (4.6)$$

The proportionality consists of measurable quantities, although the measurement of  $Q_{\text{int}}$  itself contains some assumptions and approximations (see Section 2.6.6.2). If the value for  $B_{\max}/Q_{\text{int}}$  is plotted as a function of applied voltage or transported charge, then the effect of excitation efficiency on overall device performance can be analyzed.

The radiative relaxation efficiency as defined earlier is a measure of the efficiency with which excited Nd centers, Nd\*, relax radiatively thereby producing photons. The radiative efficiency is measured by monitoring the luminescence decay lifetime of the particular transition. The radiative efficiency is site specific i.e., factors (e.g. uneven crystal field components) which affect the selection rules and oscillator strength will affect the radiative efficiency, as will non-radiative decay probability.

### 4.3 The Amount of Conduction Charge

The amount of conduction charge is one of the important factors that affects EL device performance. Here, the conduction charge above the minimum excitation threshold energy is specifically referred to. As discussed in section 2.4.1, the electrons that impact-excite luminescent centers are injected from the phosphor/insulator or the phosphor/aluminum interfaces and possibly from donor levels in the phosphor layer. As discussed in section 2.6.6.2, the quantity of conduction electrons can be increased by bulk phosphor trap ionization or, by band to band ionization leading to charge multiplication (avalanche breakdown). Increased conduction charge results in the increase in device brightness. The conduction charge was therefore determined from Q-V and  $Q_{\text{int}}-F_p$  measurements for both polarities.

### 4.4 Experimental Procedure

For the experiments described in this chapter traditional ZnS:NdF<sub>3</sub> ACTFEL devices were RF magnetron sputter deposited onto standard substrates. The device fabrication process flow is shown schematically in Figure 4.1 and the details are described in this section. This type of device structure as indicated earlier (see Section 2.3.1) is commonly known as the ‘half-stack’ structure.

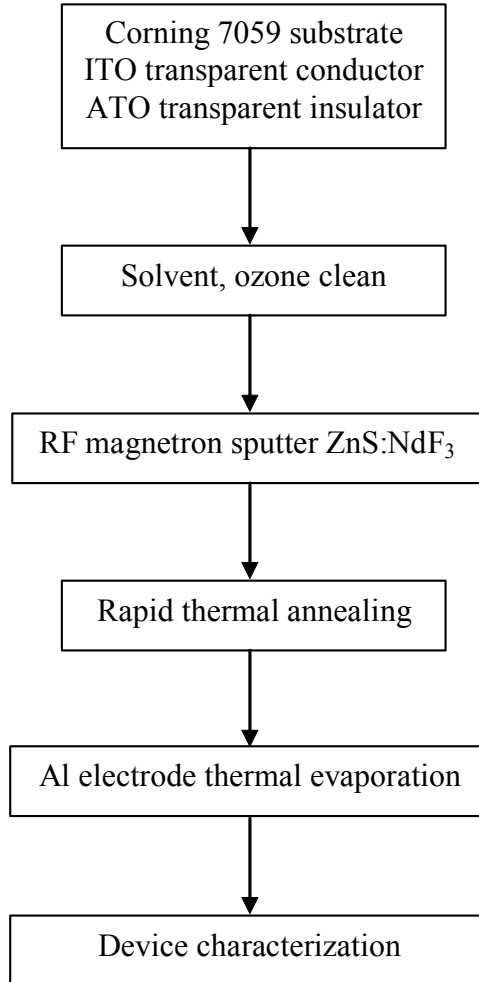


Figure 4.1 Schematic process flow diagram for ZnS:NdF<sub>3</sub> device fabrication.

#### 4.4.1 Substrate Materials

The substrates used were Corning 7059 glass substrates coated with ITO. The bottom dielectric was Al<sub>2</sub>O<sub>3</sub>/TiO<sub>2</sub> (ATO), deposited onto the ITO using ALD by Planar Systems, Inc. Before phosphor layer deposition the substrates were cleaned with methanol followed by a 6 minute ozone clean to remove hydrocarbons absorbed onto the substrate surface.

#### 4.4.2 Phosphor Layer Deposition

The ZnS:NdF<sub>3</sub> layer was deposited by RF magnetron sputtering using two individually controlled sources, namely pure ZnS and ZnS:NdF<sub>3</sub>. The pure ZnS target

was CVD grown polycrystalline bulk ZnS and was purchased from Morton Thiokol, Inc. The compound ZnS:NdF<sub>3</sub> target was purchased from SCI engineering materials. The target was prepared by mixing 98.5wt% ZnS powder with 1.5wt% NdF<sub>3</sub> powder, and hot pressing it to form the target. Multiple substrates were placed on a sample platter which rotated at a speed of 8 revolutions/minute. The sputter chamber was evacuated to a base pressure  $< 1 \times 10^{-6}$  Torr prior to deposition.

The conditions for phosphor deposition were evaluated and optimized by measuring the phosphor brightness at 20 (B<sub>20</sub>) and 40V (B<sub>40</sub>) above the threshold voltage (as indicated in Section 2.6.1.1) for the half stack devices. The following processing conditions were used for this particular study. The substrate temperature was kept at 160°C throughout the deposition. Both the ZnS and the ZnS:NdF<sub>3</sub> targets were operated at a power of 120W, with duty cycles of 100% for the ZnS target and 75% on the ZnS:NdF<sub>3</sub> target. These deposition conditions resulted in the optimal dopant concentration as determined by EL performance and measured by EDS with standards and Electron Microprobe analysis. The sputter deposition gas was Ar at a pressure of 20mTorr. Typical film thickness was  $0.78\mu\text{m} \pm 10\%$ . The resulting growth rate was typically 80-90Å/min. The sample platter is capable of holding seven 2" × 1" substrates for simultaneous processing, which allows various post-deposition processing conditions to be compared directly using identical phosphor films. One bare 2" × 1" glass substrate partially covered with a micro slide in order to create a step for measurement of thickness was included in each run. The devices were then annealed under flowing N<sub>2</sub> in a custom quartz, lamp-heated rapid thermal anneal (RTA) chamber. The sample was placed on a polished Si substrate during heating to help prevent contamination from the RTA

chamber walls. A thermocouple was placed immediately adjacent to the sample to record annealing temperature. To demonstrate the effect of annealing on device performance, a number of annealing temperatures were chosen in the range of 300°C-475°C. The standard processing conditions employed a 90 second ramp up to the desired temperature, a 60 minute anneal at that set temperature, and complete shutoff of the furnace during the cooling stage, which allowed the sample to cool to room temperature.

#### 4.4.3 Device Completion

The top electrode (0.079cm<sup>2</sup> area) was deposited via thermal evaporation of 220 nm of Al through a shadow mask using an Edwards evaporation system. Typical base pressure for this process was  $\sim 1 \times 10^{-6}$  Torr. Contact to the bottom (ITO) electrode was achieved by scratching through the upper insulating layers with a diamond scribe in order to expose the ITO layer, and melting pure indium metal, which wets the ITO layer for electrical contact, onto the scratched area using a solder gun.

### 4.5 Results

#### 4.5.1 Chemical and Structural Characterization

##### 4.5.1.1 Thin film concentration

Once the as deposited and annealed films were prepared, it was necessary to verify the rare earth concentration (Nd) in the films. From previous studies, the optimum rare earth (dopant) concentration for maximum brightness of ACTFEL devices has been observed to be in the range of 1-2 at%. The dopant concentration is extremely important in order to realize optimum brightness. Specifically, the dopant concentration must be maximized below the range where concentration quenching and clustering is negligible. Dopant concentration was measured using a JOEL Superprobe 733 (EPMA) which houses four crystals for element identification and quantification. Rare earth standards

were used to quantify the exact concentration of Nd in the films. Five to six different areas of the film were measured and the average concentration of Nd in the films was found to be 0.9 at%. EDS (energy dispersive spectroscopy) with a Nd standard gave similar results.

#### 4.5.1.2 X-ray diffraction (XRD)

As stated earlier XRD provides information regarding film quality and crystallinity. XRD data was collected using a Philips APD 3720 powder diffractometer. ZnS:NdF<sub>3</sub> films exposed to four different post-deposition conditions were chosen for analysis, specifically as-deposited films, and films annealed at 375°C, 425°C and 475°C for 1 hr . The 2θ° scan range was 27°-30° at a scan speed of 0.005°/sec, step size of 0.020°/step and 0.4sec time/step. Zinc sulfide has two observed crystal structures, cubic and hexagonal [118]. The 28.5° peak is an overlapped peak from the (111) plane of the cubic phase and the (0002) plane of the hexagonal phase. The full width half maximum (FWHM) of the 28.5° peak was used as a measure of the ZnS:NdF<sub>3</sub> thin film crystallinity. As shown in Figure 4.2, the FWHM of the 28.5° peak decreases as the annealing temperature increases, indicating improved crystallinity, with the assumption of homogeneous distribution of micro-strain throughout the films. Note that there is no sharp break in this decrease at 425°C, and that the crystallinity is better after annealing at 475°C.

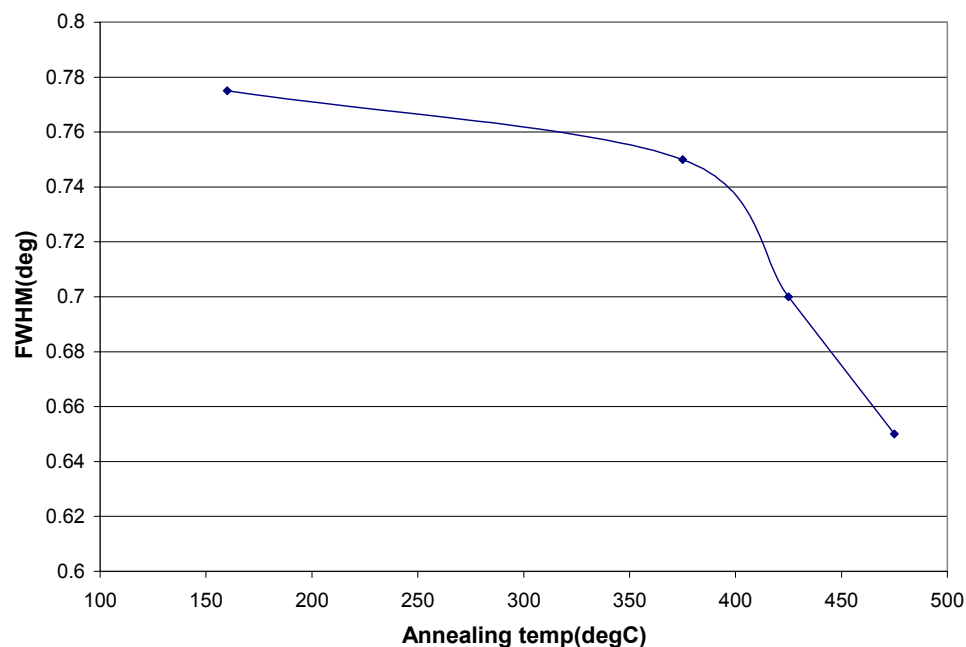
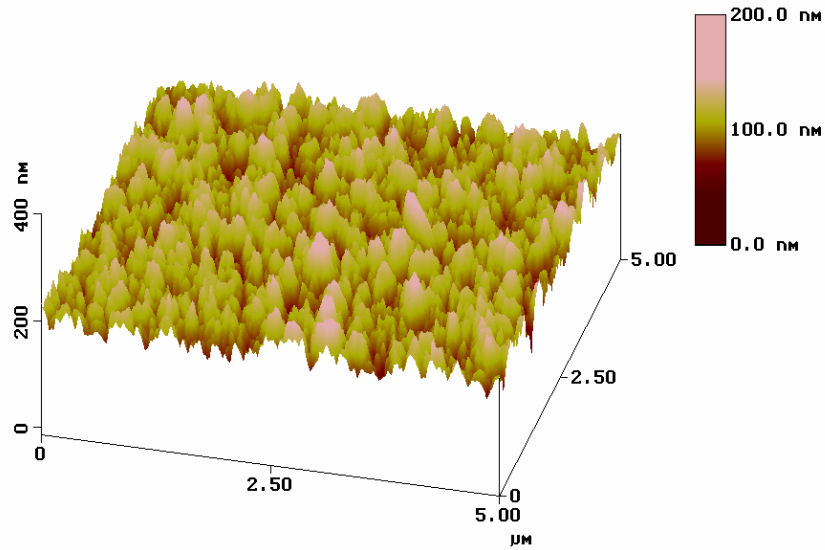


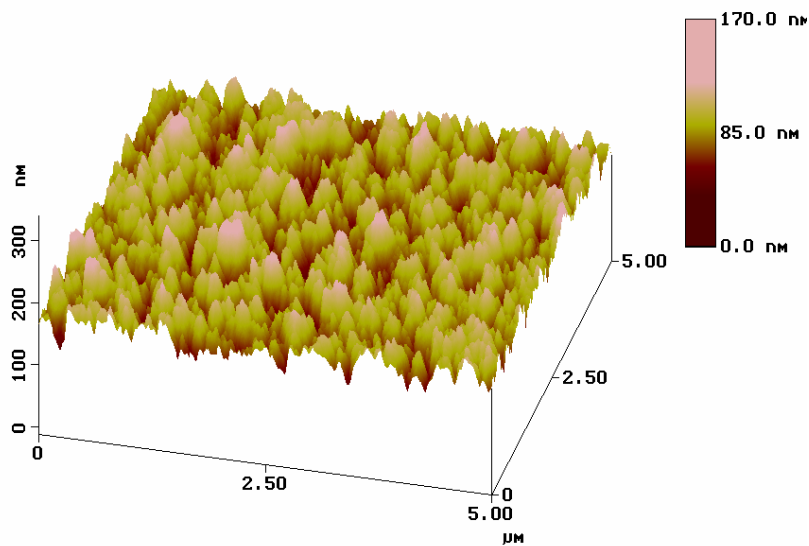
Figure 4.2 Effect of annealing temperature on the FWHM of the 28.5° X-ray diffraction peak from the ZnS:NdF<sub>3</sub> film.

#### 4.5.1.3 Atomic force microscopy (AFM)

Surface roughness can significantly affect the brightness of the device by affecting the outcoupling efficiency (see section 2.4.5 and section 4.2). As-deposited films and films annealed at 425°C for 1 hr films were quantitatively analyzed to study changes in surface roughness. Figure 4.3 shows surface morphology from AFM for as-deposited (a) and annealed ZnS:NdF<sub>3</sub> samples (b). The root mean square (RMS) surface roughness measured was 16 -16.5 nm for the as-deposited films and 15 – 15.5 nm for the annealed films. Negligible change ( $\pm 10\%$ ) in the surface roughness was observed between the two, suggesting that the outcoupling efficiency of EL emission was not changed by annealing.



(a) As-deposited ZnS:NdF<sub>3</sub> thin film (RMS = 16nm)



(b) Annealed 425°C for 1 hr ZnS:NdF<sub>3</sub> thin film (RMS = 15)

Figure 4.3 AFM surface morphologies of a) as-deposited and b) annealed at 425°C for 1 hr ZnS:NdF<sub>3</sub> thin films.

#### 4.5.1.4 Transmission electron microscopy (TEM)

It was difficult to resolve the cubic and hexagonal phases of the ZnS:NdF<sub>3</sub> thin film based on XRD data. To address the question about the ZnS phase, TEM was used to investigate the structure of the ZnS:NdF<sub>3</sub> thin films on a microscopic scale. A JOEL 200

CX TEM operating at 300keV was used for characterization and cross section samples were prepared as outlined by the method described in section 3.3.5. Figure 4.4 shows cross section TEM (XTEM) micrographs for ZnS:NdF<sub>3</sub> thin films in the as deposited (Figure 4.4a) and the annealed conditions (Figure 4.4b) which clearly shows the multi-stacked ACTFEL structure. To study the structure of the thin film device, electron diffraction patterns were collected from various parts of the ZnS:NdF<sub>3</sub> film. Standard cubic and hexagonal patterns for ZnS were obtained using Desktop Microscopist software where the space group and relative positions of the Zn and S atoms are input and diffraction patterns can be obtained (in this case, the polycrystalline ring pattern). Using a standard, our approach was to match the experimentally observed patterns to the standard patterns and index them accordingly. TEM revealed a mixture of two structures (cubic and hexagonal) though it was difficult to resolve one from the other. In one area of the film a predominantly cubic structure (Figure 4.4d) was observed whereas in other areas it was predominantly hexagonal (Figure 4.4c). On the whole a rather non-homogenous film was observed. Qing Zhai [119] showed with HRTEM that the structure switched back and forth.

#### 4.5.2 Optical Characterization

##### 4.5.2.1 Brightness-voltage (B-V) plots

The most common type of luminance plot, as mentioned earlier, is the brightness versus voltage plot, which is probably the most important measurement used to evaluate device performance. From this measurement, several important ACTFEL parameters such as threshold voltage ( $V_{th}$ ) and luminance ( $B_{40}$ ) at  $V_{th} + 40V$  can be extracted. The brightness vs. voltage behavior of the half cell ZnS:NdF<sub>3</sub> devices is shown in Figure 4.5. The wavelength monitored for this plot was 910nm ( ${}^4F_{3/2} \rightarrow {}^4I_{9/2}$  transition). Brightness

was monitored as a function of the applied voltage and the data was plotted for two samples: one as-deposited and the other annealed at 425°C for 1 hour. The threshold voltage ( $V_{th}$ , determined by method of extrapolation of the largest slope as detailed in section 2.6.1.1) and brightness values at 40 V above threshold ( $B_{40}$ ) were then derived from these plots. The threshold voltages for the as-deposited and annealed samples were 230V and 185V, respectively. Based on these threshold values,  $V_{40}$  equals 270V for the as deposited sample, whereas it was 225V for the annealed sample. It should also be noted that the threshold voltage for the visible transition was the same as that for the infrared transition.

These respective threshold voltages, 230V for the as-deposited sample and 185V for the annealed sample were then used as references for measuring and comparing the device brightness and device efficiencies between the as-deposited and annealed samples.

The values of diffuse reflectance for the as-deposited and annealed samples did not vary significantly (~10-15 % variation between the as-deposited and annealed samples). The data is shown in Figure 4.6. These values would enable us to get an idea about the outcoupling efficiency and discuss its influence on the total device efficiency.

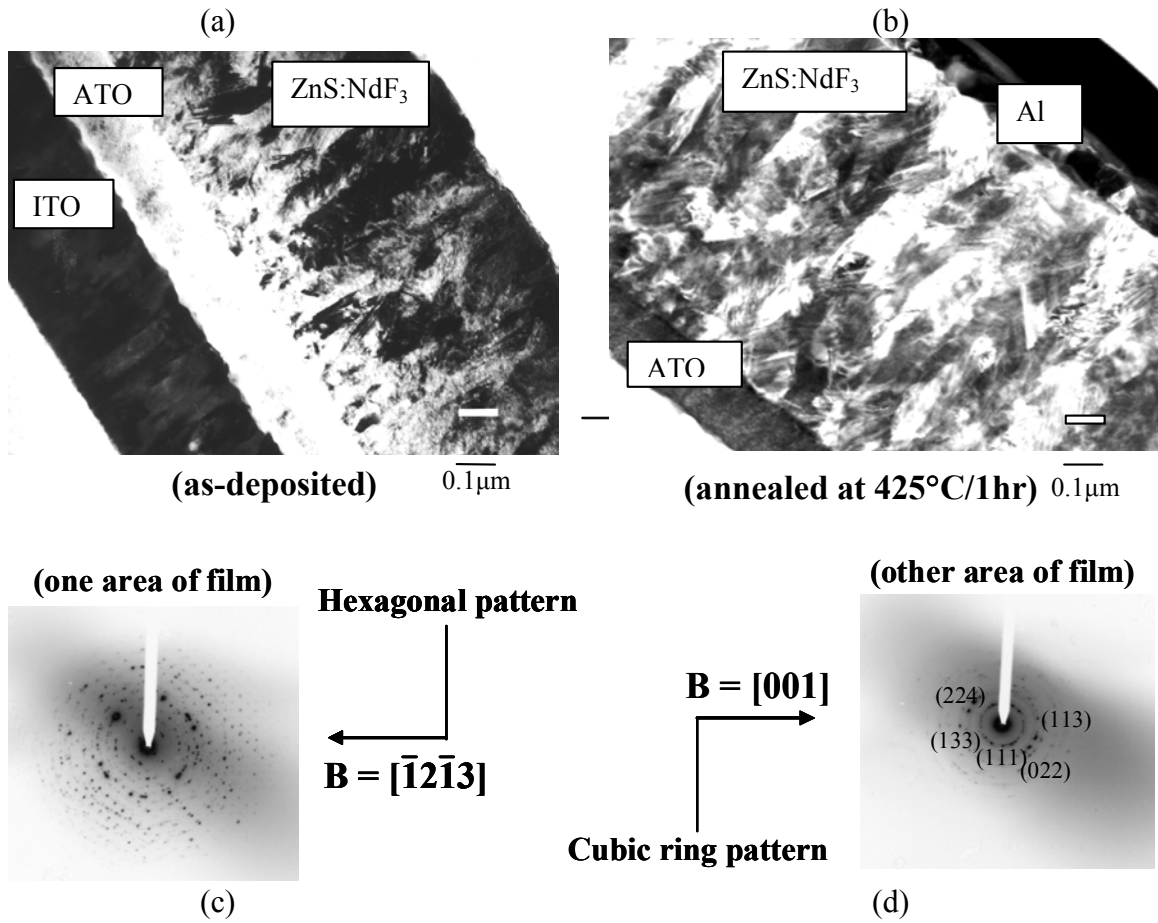


Figure 4.4 XTEM micrographs for ZnS:NdF<sub>3</sub> thin films.

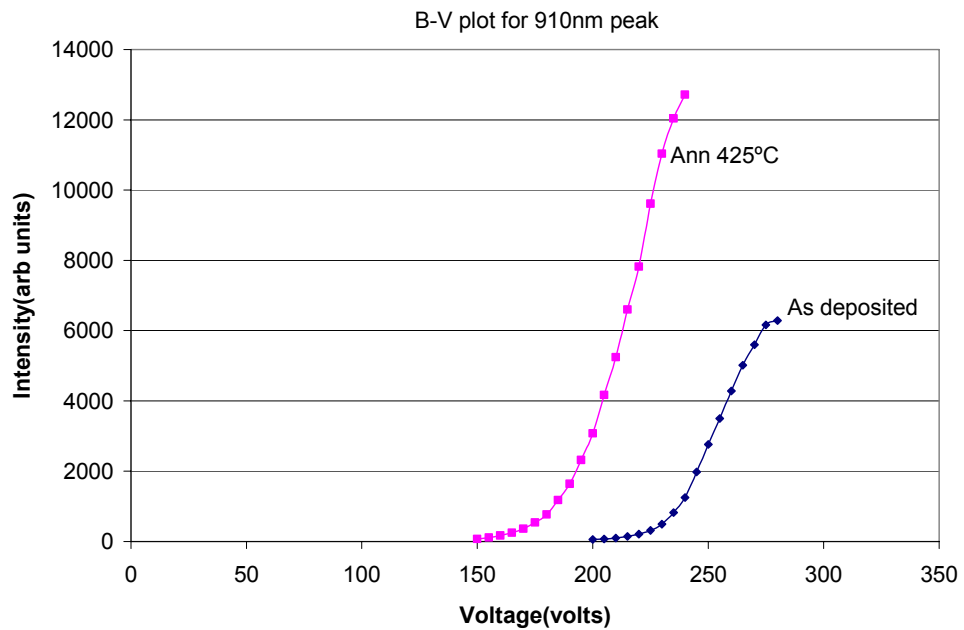


Figure 4.5 Brightness vs. voltage behavior as a function of annealing treatment.

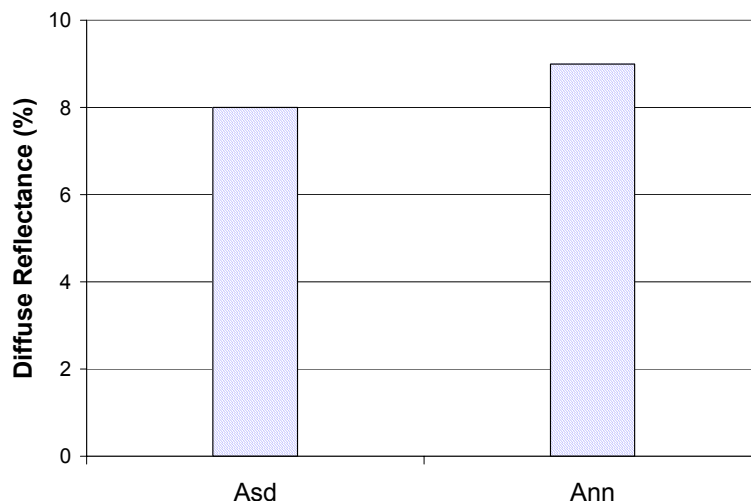
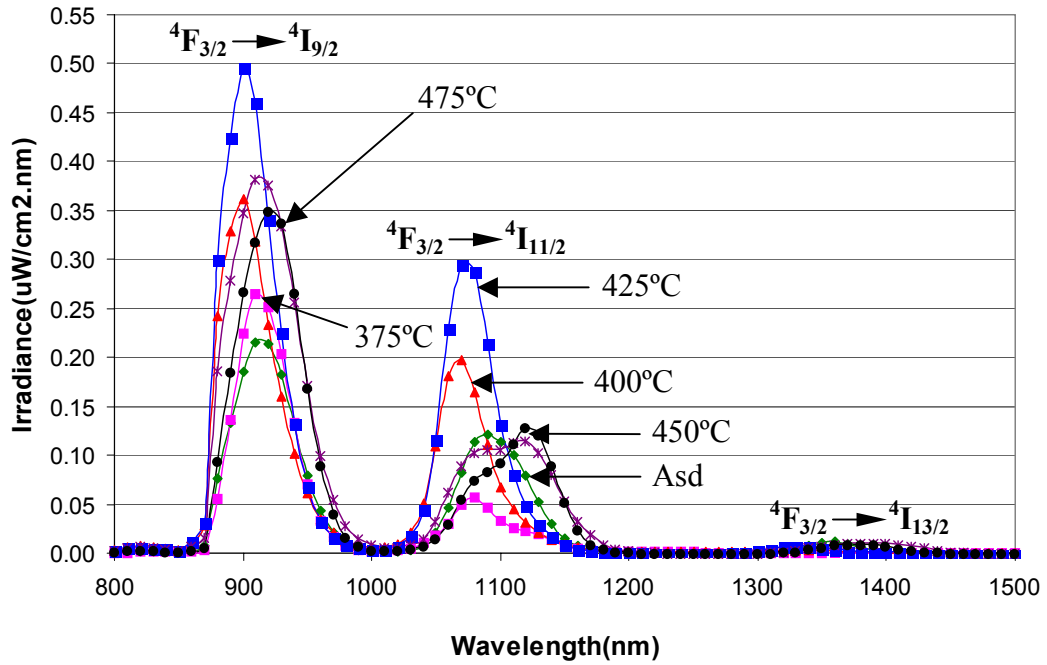


Figure 4.6 Diffuse reflectance values for as-deposited and annealed (425°C for 1 hr) ZnS:NdF<sub>3</sub> films.

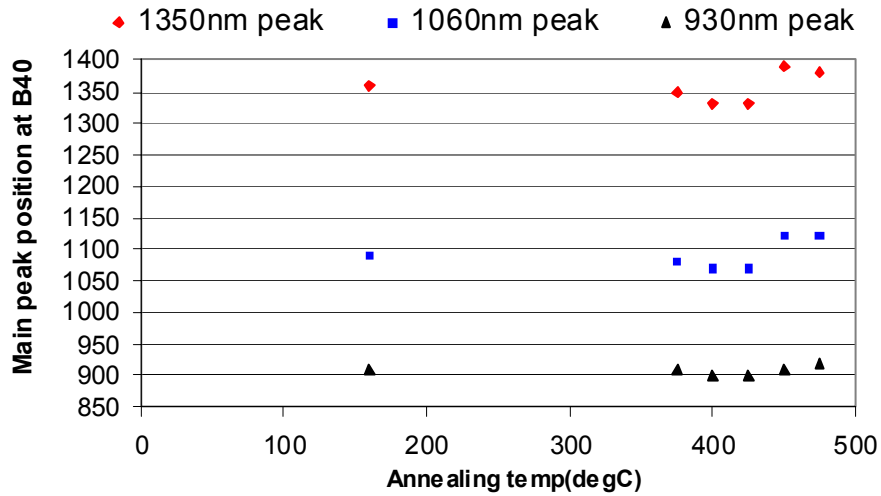
#### 4.5.2.2 The effect of annealing on infrared electroluminescence of ZnS:NdF<sub>3</sub> thin film devices

As mentioned earlier, the as-deposited and annealed samples were driven at their respective  $V_{40}$  voltages. Electroluminescence emission (EL) was excited by applying 2.5 kHz positive and negative trapezoidal voltage pulses, 30 $\mu$ s in length with 5 $\mu$ s rise and fall times. The emitted light was analyzed with a calibrated spectrometer featuring an Oriel MS257 1/4m monochromator and reflective optics. A chopper and lock-in detector was used to improve the signal to noise ratio. A Si photomultiplier (PMT) tube was housed on one exit port of the monochromator, which was capable of measuring visible emission wavelengths (300-800nm). A thermo-electric cooled Ge photodiode on a second exit port was used to detect light with wavelengths from 0.8 $\mu$ m up to 1.8  $\mu$ m. An Oriel Merlin<sup>TM</sup> radiometry system controlled the chopper and was used to interface the monochromator and detectors with the acquisition software. The experimental setup for these measurements is shown in Figure 3.4.

The effect of annealing temperature on the infrared EL spectra from ZnS:NdF<sub>3</sub> films is shown in Figure 4.7a. Brightness values in the visible region of the spectrum are measured in terms of cd/m<sup>2</sup>, which take into account the photopic response of the eye. In the infrared region of the spectrum the term brightness loses its meaning, and units of optical irradiance, i.e. μW/cm<sup>2</sup>.nm, are used for quantifying optical output. The Nd emission peaks at 910, 1060 and 1350nm arise from the <sup>4</sup>F<sub>3/2</sub>→<sup>4</sup>I<sub>9/2</sub>, <sup>4</sup>F<sub>3/2</sub>→<sup>4</sup>I<sub>11/2</sub> and <sup>4</sup>F<sub>3/2</sub>→<sup>4</sup>I<sub>13/2</sub> transitions, respectively [84, 85]. On increasing the annealing temperature up to 425°C, an increase in EL intensities was observed for the above mentioned transitions. Anneals at higher temperatures resulted in decreased EL infrared emission intensities. The wavelengths of the peak maxima versus annealing temperature are shown in Figure 4.7b. There is a slight blue shift of the peaks with annealing temperatures between as-deposited and 425°C, followed by a red shift for annealing temperatures above 425°C. The intensity of both the 1060 and 910nm peaks increased with increasing anneal temperature up to 425°C, but decreased above this temperature (Figure 4.7c). To study the effect of annealing on the visible emission intensity, the 600nm peak (<sup>4</sup>G<sub>5/2</sub>→<sup>4</sup>I<sub>9/2</sub> transition) was monitored. As shown by the inset in Figure 4.7c, the 600nm visible EL peak intensity (<sup>4</sup>G<sub>5/2</sub>→<sup>4</sup>I<sub>9/2</sub>) was lowest from a sample annealed at 425°C, but the intensity increases for higher annealing temperatures. Hence a contrast in behavior was observed in changes of emission intensity between visible and infrared peaks and annealing temperatures at and above 425°C. To obtain the power density (radiance) values, the area under the corresponding EL peak was integrated. The radiance values at 1060nm and 910nm for ZnS:NdF<sub>3</sub> after a 425°C anneal (Figure 4.7d) were found to be twice (15 and 25μW/cm<sup>2</sup>, respectively) that of the as deposited sample.

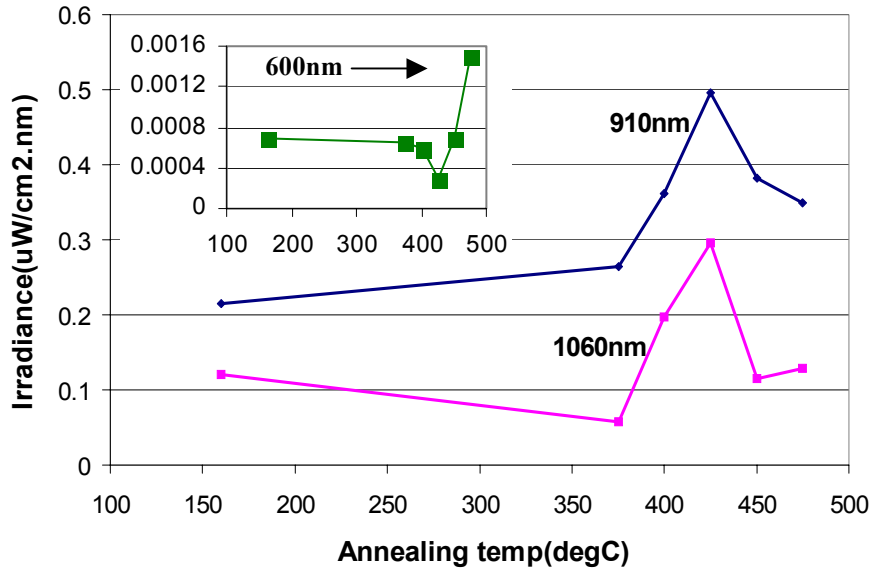


(a)

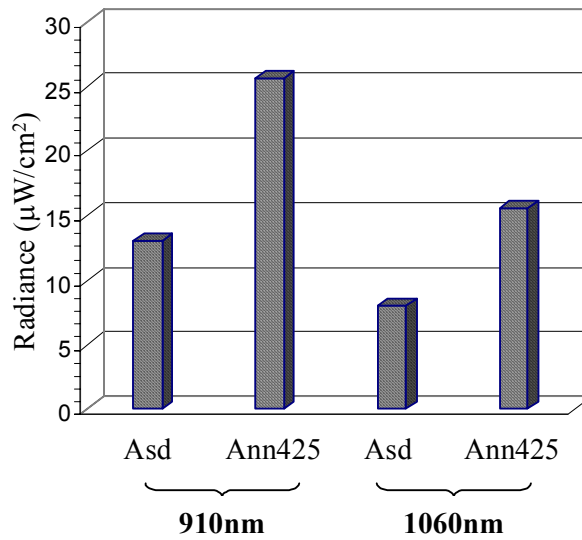


(b)

Figure 4.7 Effect of annealing on the IR EL emission from ZnS:NdF<sub>3</sub> thin films. (a) EL spectrum showing shifts in emission wavelength, (b) emission peak wavelength versus annealing temperature, and (c) plot of irradiance versus annealing temperature for the 910 and 1060 nm peaks. The inset in (c) shows the dependence of the visible emission peak at 600nm upon the anneal temperature. Note that for  $T > 425^\circ\text{C}$ , the visible peak increases while the IR peaks decrease in irradiance, (d) comparison of EL for as deposited and annealed sample.



(c)



(d)

Figure 4.7 continued.

#### 4.5.2.3 Luminescence decay characterization (room temperature)

Electroluminescence decay together with device current measurements as a function applied voltages are used to evaluate the mechanisms responsible for luminescence. The visible luminance versus time ( $L(t)$ ) as a function of applied voltage was studied by monitoring the output of the PMT as well as the applied voltage pulse simultaneously on an oscilloscope (Tektronix TDS 510A digitizing). The setup for

collecting the luminescence decay data is described in sections 3.3.2 and 3.3.8. The oscilloscope was also used to monitor the luminescence and the voltages at different positions in the circuit as a function of time. Figure 4.8 shows a schematic of the actual setup utilized for measuring the time resolved luminescence decay data. For an  $Al^+$  pulse,  $Ch_1$  and  $Ch_2$  monitors the voltage pulse before and after the  $128\Omega$  resistor,  $Ch_3$  monitors the current for the first half of the pulse and  $Ch_4$  monitors the luminescence directly by connecting the output of the PMT to the oscilloscope. On the contrary when the polarity changes for an  $Al^-$  pulse,  $Ch_3$  records the pulse voltage,  $Ch_2$  records current and  $Ch_4$  measures the luminescence as a function of time.

The oscilloscope not only monitors the luminescence behavior but also monitors conduction current as a function of the applied voltage. Trapezoidal 2.5kHz frequency pulses were applied to the device with rise, fall and dwell times of  $5\mu s$  each and the devices were operated at  $V_{40}$  voltage. A short pulse width of  $5\mu s$  was chosen over a longer one ( $30\mu s$ ), since it enables us to measure the luminescence decay behavior during and at the end of the pulse, whereas with the  $30\mu s$  pulse the luminescence starts to decay even before the pulse ends.

Due to equipment limitations, it was not possible to measure time decays for the near infrared transitions. This was measured for only the visible 600nm emission ( ${}^4G_{5/2} \rightarrow {}^4I_{9/2}$ ) for neodymium. Luminescence data was collected for an entire pulse ( $Al^+$  and  $Al^-$  polarities), but for better viewing only the  $Al^+$  polarity data have been plotted.

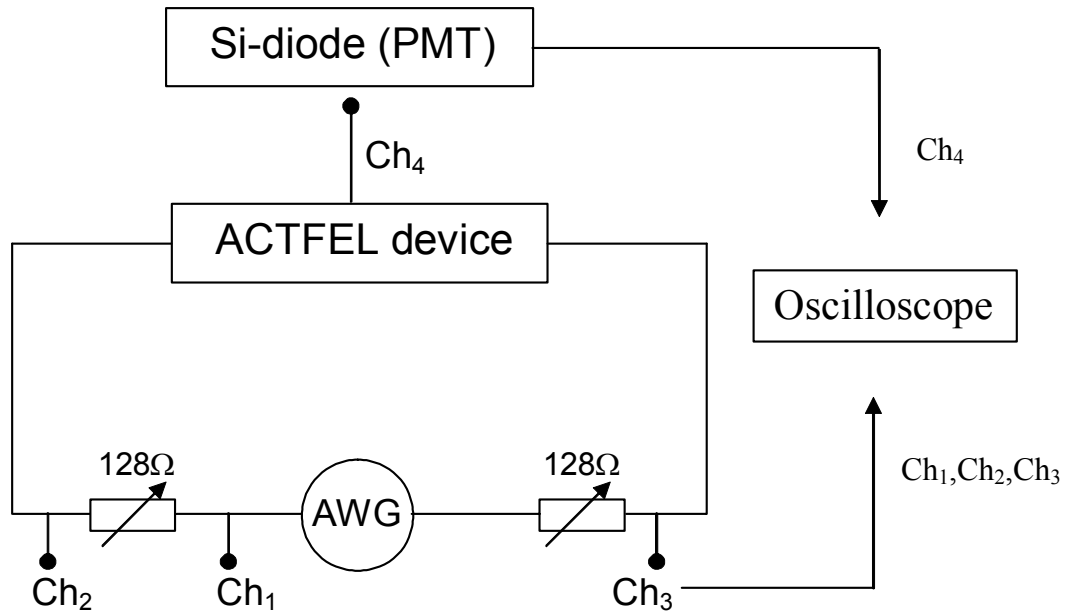
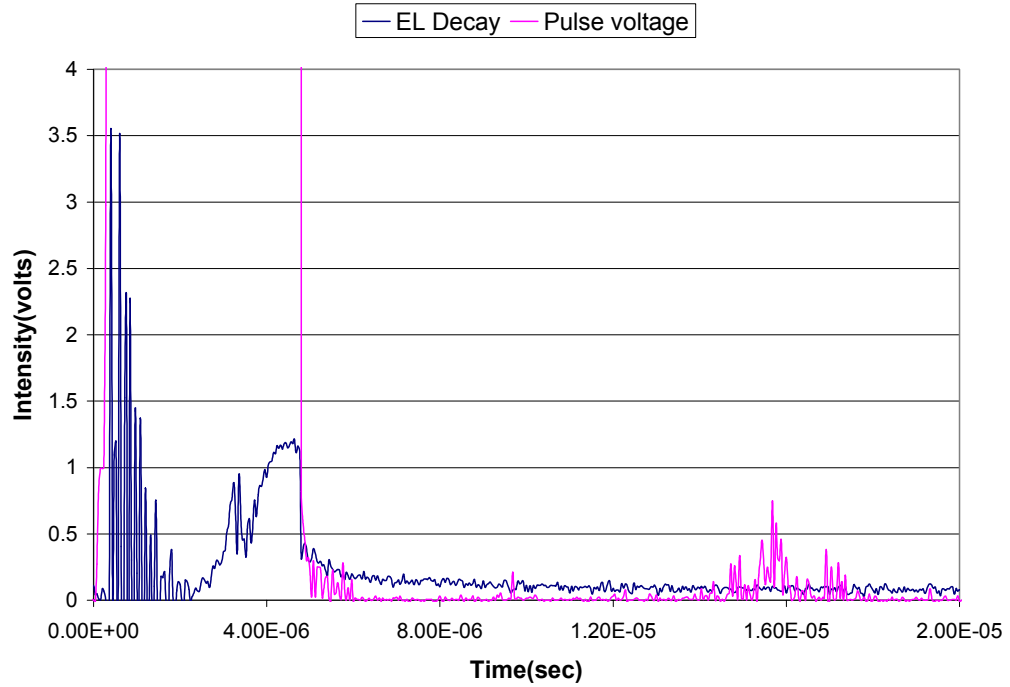


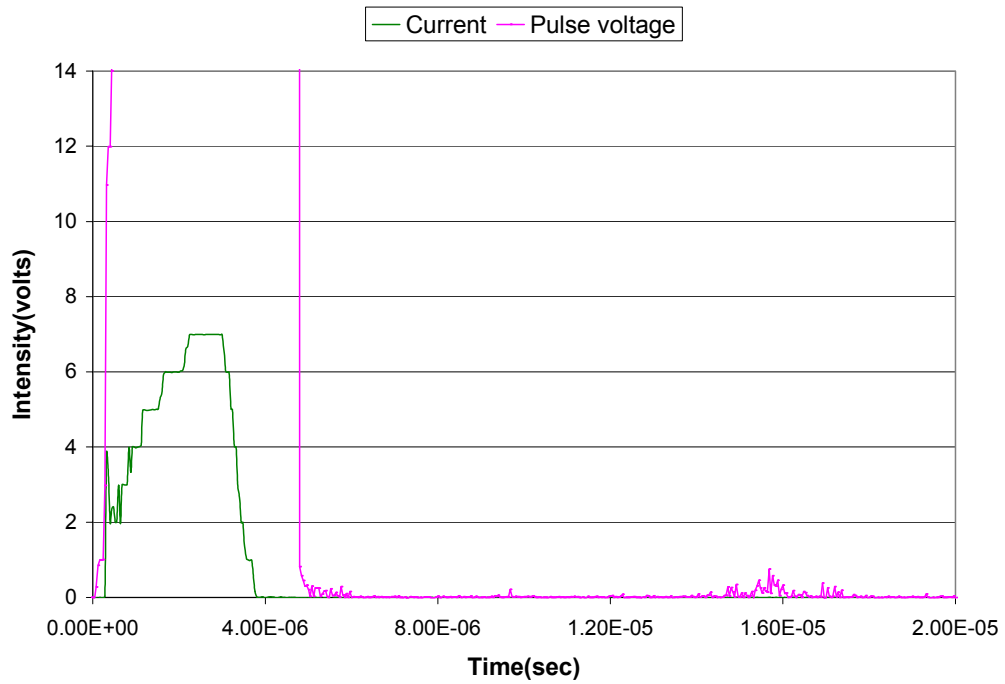
Figure 4.8 Luminescence decay data measurement setup for ZnS:NdF<sub>3</sub> thin films.

Figure 4.9a shows the luminescence decay behavior and applied voltage pulse of the as deposited ZnS:NdF<sub>3</sub> film versus of time. Luminescence is observed at the rising edge of the voltage pulse and decays to near zero within 20 μs after the voltage pulse ends, suggesting that the luminescent lifetime is shorter than this time.

To better understand the EL decay data, the conduction current through the device was monitored simultaneously with the applied voltage (Figure 4.9b). The conduction current can be calculated mathematically from the voltage data by using equation 2.25. The current through of the device increased during the pulse but dropped back to zero at the end of the pulse. There was no evidence of current flow after the external voltage was removed (e.g. from a reverse bias field).

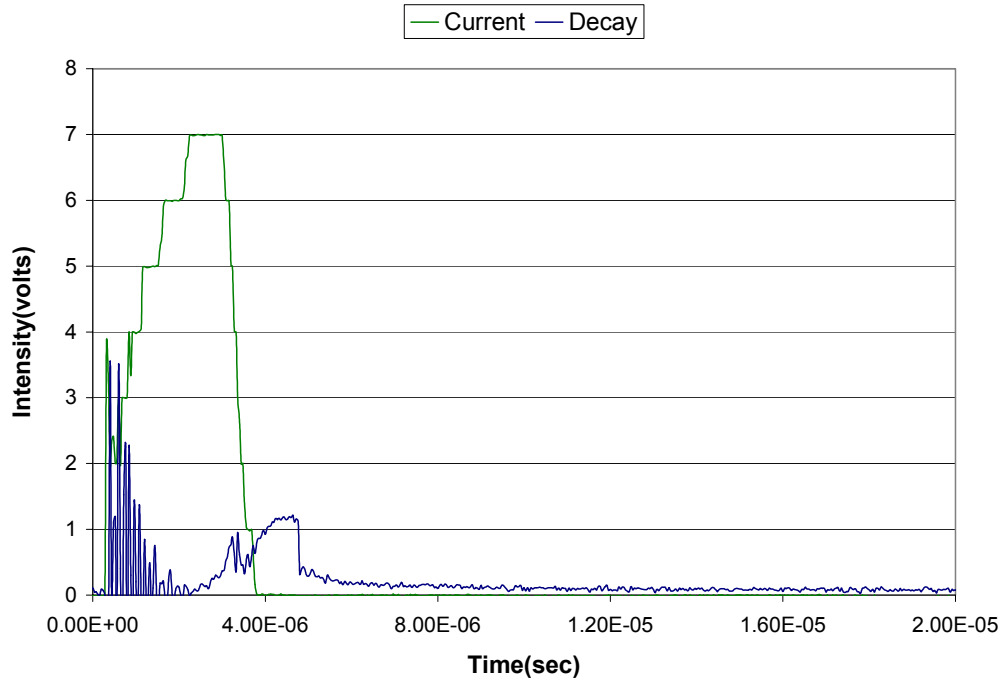


(a)



(b)

Figure 4.9 Luminescence decay behavior for as deposited ZnS:NdF<sub>3</sub> thin film operated at  $V_{40}$ , 2.5kHz frequency, 5 $\mu$ s pulse width. (a) luminescence decay and applied voltage (b) conduction current and applied voltage, and (c) luminescence and conduction current versus time.



(c)

Figure 4.9 continued.

Using the above data, luminescence and current versus time may be compared on a common plot (Figure 4.9c). The drop in the conduction current, and the onset of luminescence decay correspond well with the trailing edge of the applied voltage pulse (as seen from Figures 4.9a and 4.9b).

To obtain a value for the decay constant, the luminescence data in Figure 4.9 was fitted by two exponential functions. Figure 4.10 shows the un-smoothed time resolved luminescence data (black line) for an as deposited ZnS:NdF<sub>3</sub> thin film.

It was impossible to accurately fit the time decay data with a single exponential and hence a double exponential was utilized (red line). The decay curve consists of an initial fast decay from an intensity (in arb. units) of  $I = 0.2$  to  $I = 0.1$  with a time constant of  $3\mu\text{s} \pm 2\mu\text{s}$ , followed by a slower decay from  $I = 0.1$  to  $I = 0.07$  with a time constant of  $20\mu\text{s} \pm$

5 $\mu$ s. Note that the signal to noise ratio was low (signal to noise ratio of 1.5) for these data.

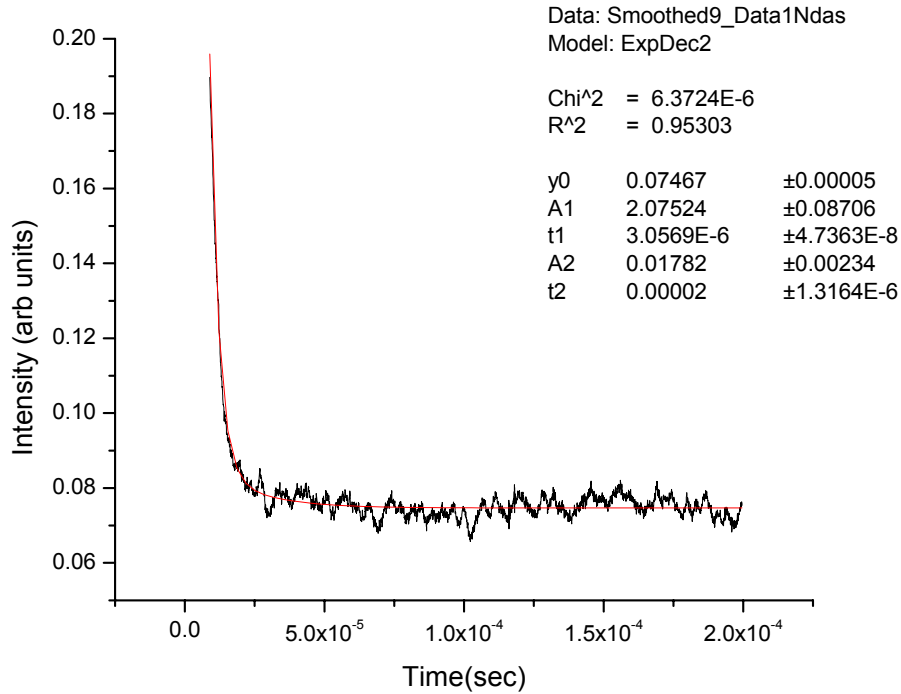
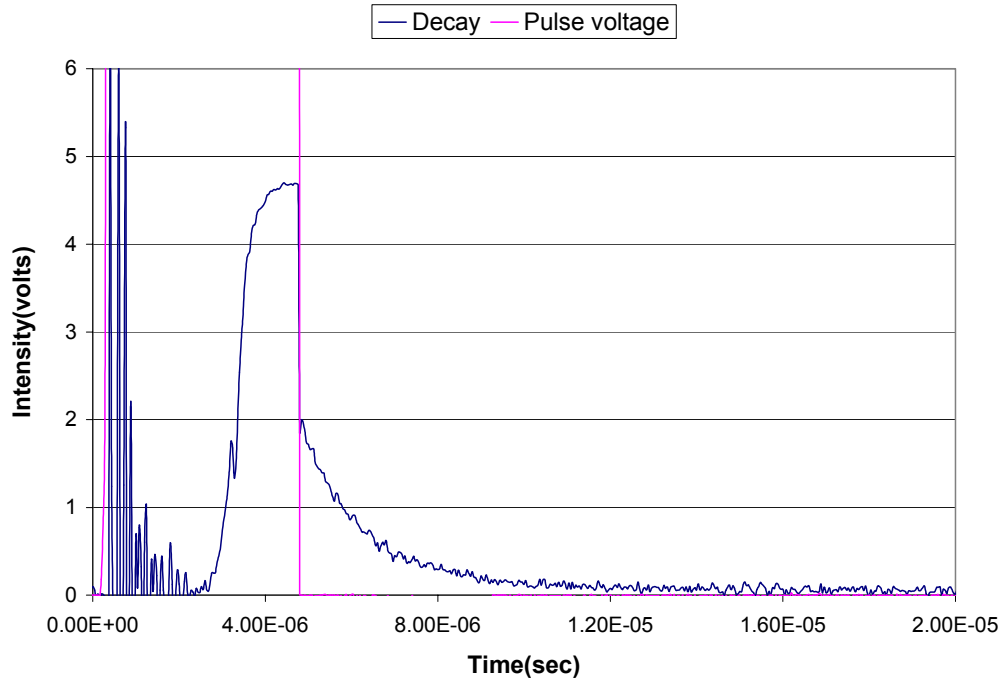


Figure 4.10 Time resolved luminescence decay data for ZnS:NdF<sub>3</sub> as deposited thin film.

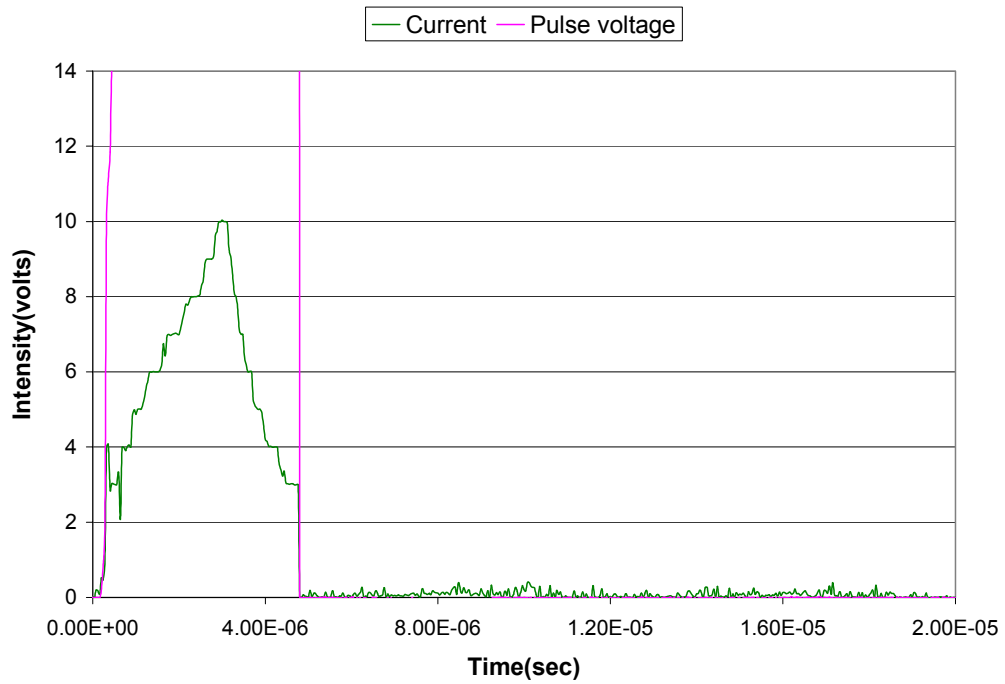
Similar to the as deposited ZnS:NdF<sub>3</sub>, luminescent decay from the 425°C annealed film sample was also studied for the same 600nm emission ( $^4G_{5/2} \rightarrow ^4I_{9/2}$ ) using a 5 $\mu$ s pulse at 2.5kHz (Figure 4.11a). The signal to noise ratio in Figure 4.11a was larger (almost 4-5 times) than that in Figure 4.9a because the luminescence signal is larger.

Figure 4.11b shows the conduction current behavior and pulse voltage versus time. As before, it was clearly observed that the current through the device increased during the pulse but dropped down to zero at the end of the pulse.

From the above plots, luminescence and current behavior with respect to applied voltage is shown on a common plot (Figure 4.11c).

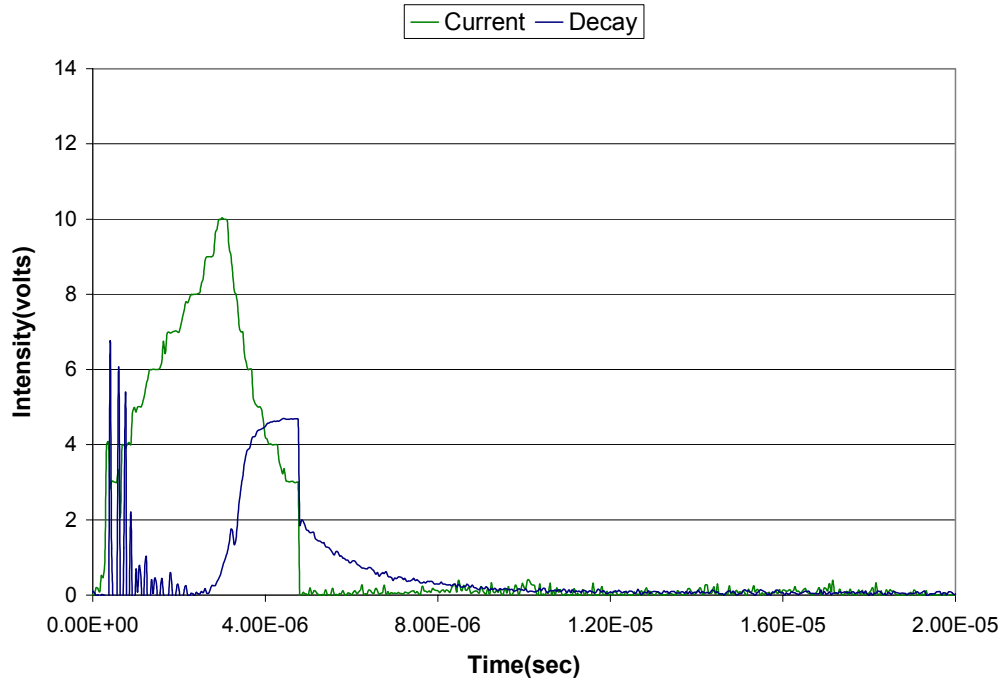


(a)



(b)

Figure 4.11 Luminescence decay behavior for annealed ZnS:NdF<sub>3</sub> thin film operated at  $V_{40}$ , 2.5kHz frequency, 5 $\mu$ s pulse width (a) luminescence decay and applied voltage, (b) conduction current and applied voltage, and (c) luminescence and conduction current versus time.



(c)

Figure 4.11 continued.

Figure 4.12 shows the unsmoothed time resolved luminescence decay data (black line), for the annealed ZnS:NdF<sub>3</sub> thin film. The luminescence decay behavior is similar to that from as deposited films, requiring two exponential functions to be fitted accurately. The data were best fitted with two consecutive (from  $I = 2$  (arb. units) to 0.9 (arb. units) with a time constant of  $1.3\mu\text{s} \pm 2\mu\text{s}$ , and from  $I = 0.9$  (arb. units) to 0.15 (arb. units) with a time constant of  $10\mu\text{s} \pm 5\mu\text{s}$ ) exponential functions (red line).

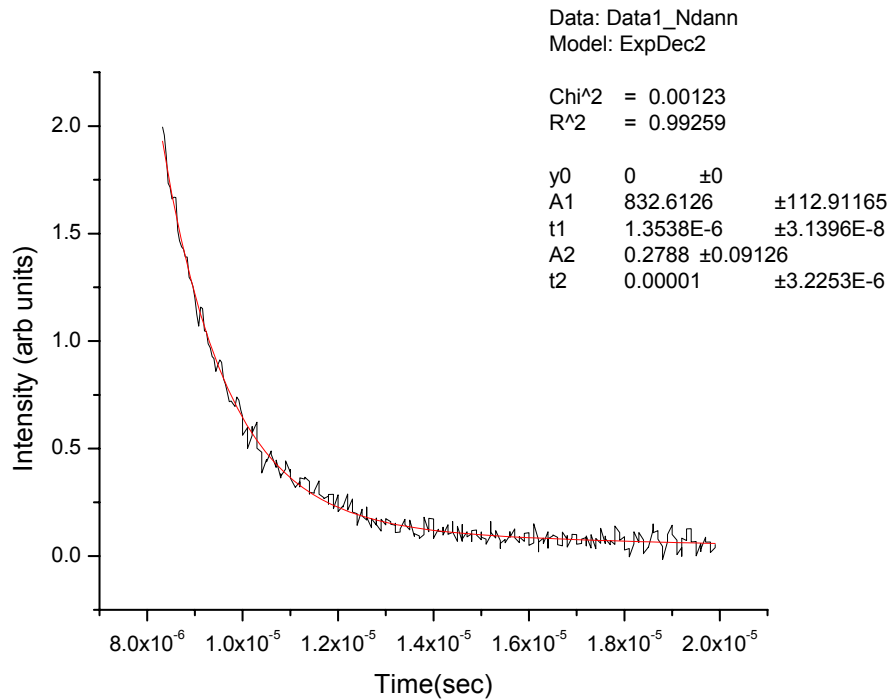


Figure 4.12 Time resolved luminescence decay data for ZnS:NdF<sub>3</sub> annealed thin film.

#### 4.5.3 Electrical Characterization

Neglecting the additional dissipative process of luminescence, an ACTFEL device is essentially a two-terminal electrical device. The significance of and procedure for measuring electrical properties were already discussed in chapters 2 and 3. The transport properties of an ACTFEL device are often studied by the time resolved current and voltages of the device as discussed in Section 2.6.6.2, often in conjunction with studying time resolved luminescence. Q-V, C-V and Q<sub>int</sub>-F<sub>p</sub> plots were measured using a Sawyer-Tower bridge and a 128 Ω resistor as the sense element to measure either the stored charge or the current, respectively, using a Tektronix TDS 510A digitizing oscilloscope. The circuit for electrical characterization is shown in Figure 4.8.

The Q-V plot in Figure 4.13 shows the external charge on the y-axis versus the applied voltage on the x-axis for both Al (+) and Al (-) polarities. Data at 40V above their

respective thresholds are shown in Figure 4.13 for the as deposited and annealed ( $425^\circ$  for 1 hr) ZnS:NdF<sub>3</sub> thin film samples. First, note that the Q-V loop is read in a counter-clockwise direction. For the Q-V data in Figure 4.13, the most obvious differences are (1) the amount of average total external charge was smaller for the as deposited sample ( $1.85\mu\text{C}/\text{cm}^2$  compared to  $5.58\mu\text{C}/\text{cm}^2$  for the annealed sample), (2) the turn on voltage for the annealed sample (185V), was much smaller than that for the as deposited sample (230V), and (3) the slope of the Q-V curve before electrical turn on for the annealed sample was much larger than that for the as deposited sample.

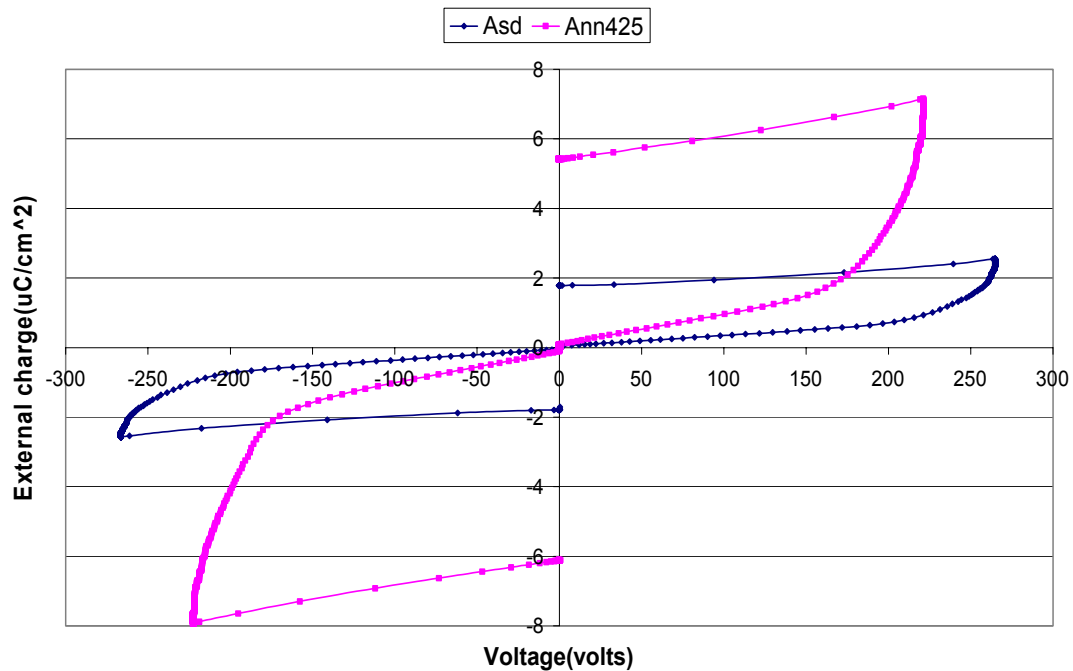


Figure 4.13 External charge ( $Q_{\text{ext}}$ ) versus applied voltage ( $V_{\text{EL}}$ ) for Al (+) and Al (-) polarities at 40V above threshold for as deposited and annealed at  $425^\circ\text{C}$  for 1 hr ZnS:NdF<sub>3</sub> thin film samples.

Figure 4.13 shows that the annealed films exhibit a significantly larger conduction charge as compared to the as-deposited film. Specifically, in comparison to the as-deposited film, the annealed film shows almost thrice the conduction charge density at

$V_{40}$ . No significant differences were seen between the Al (+) and the Al (-) polarities and the Q-V plot was almost symmetric.

Capacitance-voltage plots were generated for the as deposited and annealed samples as well. The results are shown in Figure 4.14. The first characteristic to note is the rigid shift of the applied voltage to a lower value for the annealed sample compared the as-deposited sample. This is in agreement with the voltage drop seen in the Q-V plot. Second, the capacitance value for the annealed sample at threshold is much larger than that for the as-deposited sample.

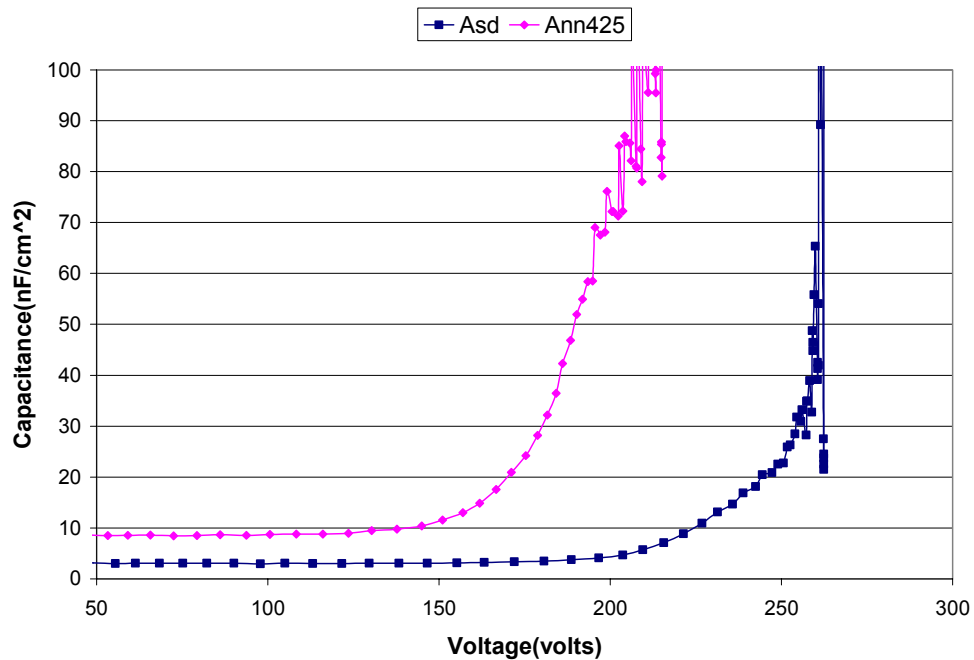


Figure 4.14 Capacitance (C) versus applied voltage ( $V_{EL}$ ) for Al (+) polarity at 40V above threshold for as deposited and annealed (425°C for 1 hr) ZnS:NdF<sub>3</sub> thin film samples.

There are two limitations in the use of Q-V data to understand device physics. First, it is not easy to accurately quantify the magnitudes of various kinds of charge (e.g. polarization and conduction charge) based on a Q-V curve because some of these charges are internal and others are external. Second, the voltage axis of a Q-V curve involves the

voltage applied across the entire ACTFEL stack. As described above, these data can be reduced to determine the internal charge ( $Q_{int}$ ) versus phosphor field ( $F_p$ ) Figure 4.15 shows internal charge ( $Q_{int}$ ) versus phosphor field ( $F_p$ ) data for as deposited and annealed ZnS:NdF<sub>3</sub> thin film samples at 40V above their respective threshold voltages for the Al (+) and Al (-) polarities.

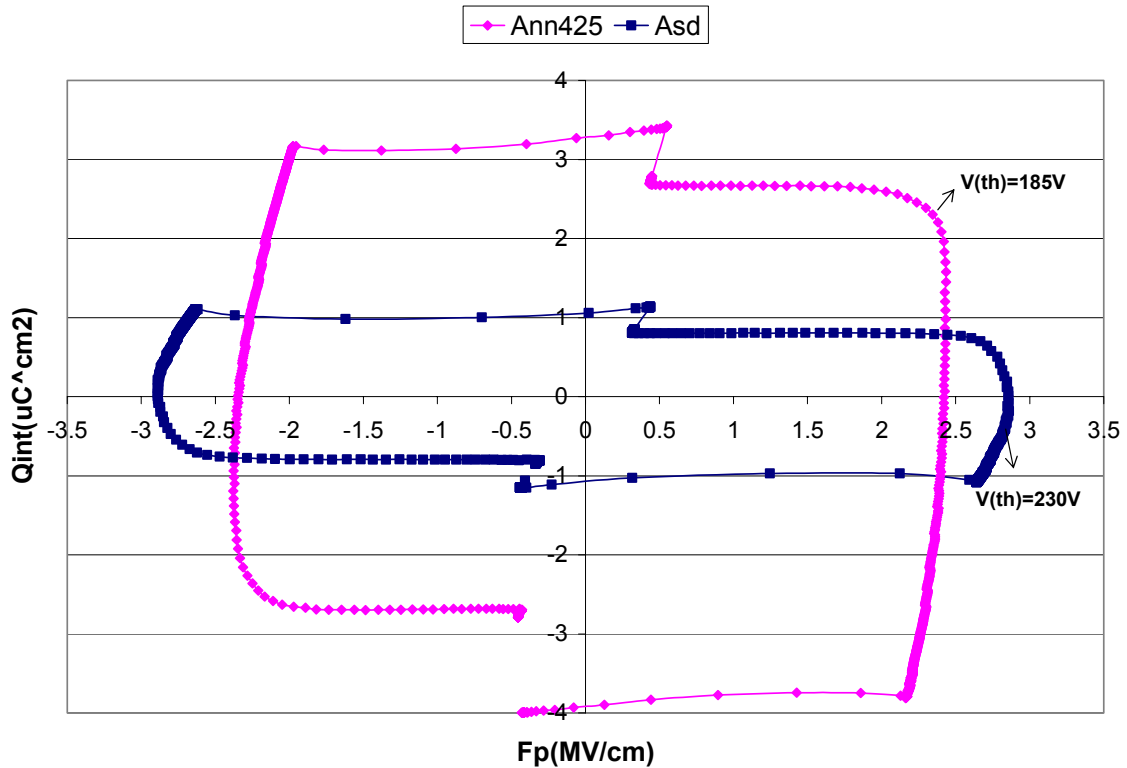


Figure 4.15 Internal charge ( $Q_{int}$ ) versus phosphor field ( $F_p$ ) for Al (+) and Al (-) polarities at 40V above threshold for as deposited and annealed (425°C for 1 hr) ZnS:NdF<sub>3</sub> thin film samples.

To reduce the data to that shown in Figure 2.19, the  $Q_{int}$ - $F_p$  plots exhibited horizontal lines between A-B and DE and vertical line between B-C when the phosphor capacitance was chosen to be 0.26nF for the as deposited film and 0.69nF for the annealed films. These values correspond to 3.33 nF/cm<sup>2</sup> and 8.79nF/cm<sup>2</sup>, respectively. The  $Q_{int}$ - $F_p$  data shows a steady state field ( $F_{ss}$ ) of 2.8MV/cm for the as deposited sample versus 2.4MV/cm for the annealed sample. The average internal conduction charge for

the annealed sample ( $6\mu\text{C}/\text{cm}^2$ ) is also much higher (3.3 times) than that of the as deposited sample ( $1.77\mu\text{C}/\text{cm}^2$ ).

The excitation efficiency is estimated by the value of the maximum brightness ( $B_{\text{max}}$ ), divided by the transferred internal conduction charge ( $Q_{\text{int}}$ ) for different voltages. The maximum brightness ( $B_{\text{max}}$ ) was measured simultaneously by recording the time-dependent EL emission,  $L(t)$ . Due to voltage oscillations from the high voltages and ramp rates, it was necessary to extrapolate the  $L(t)$  back to its maximum value as shown schematically in Figure 4.16.

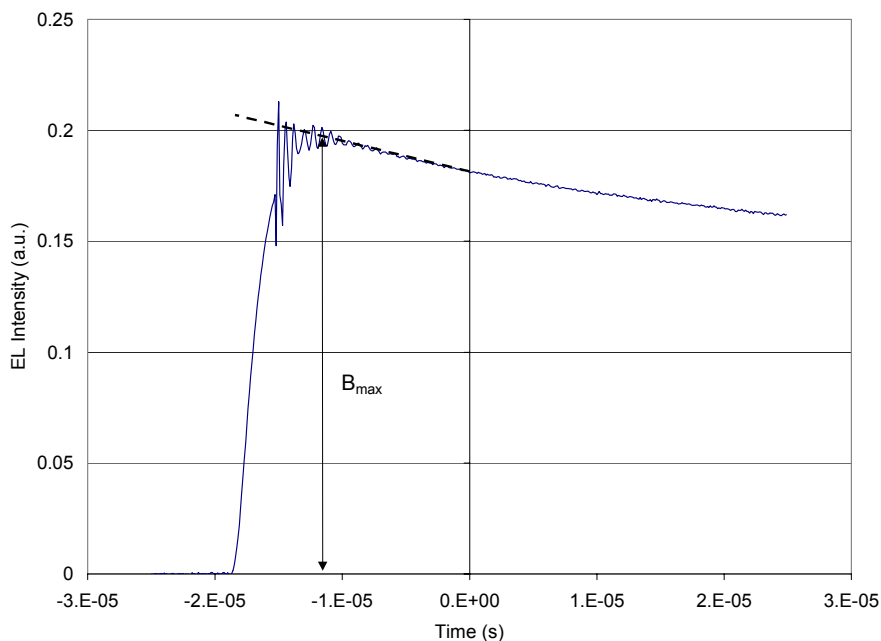
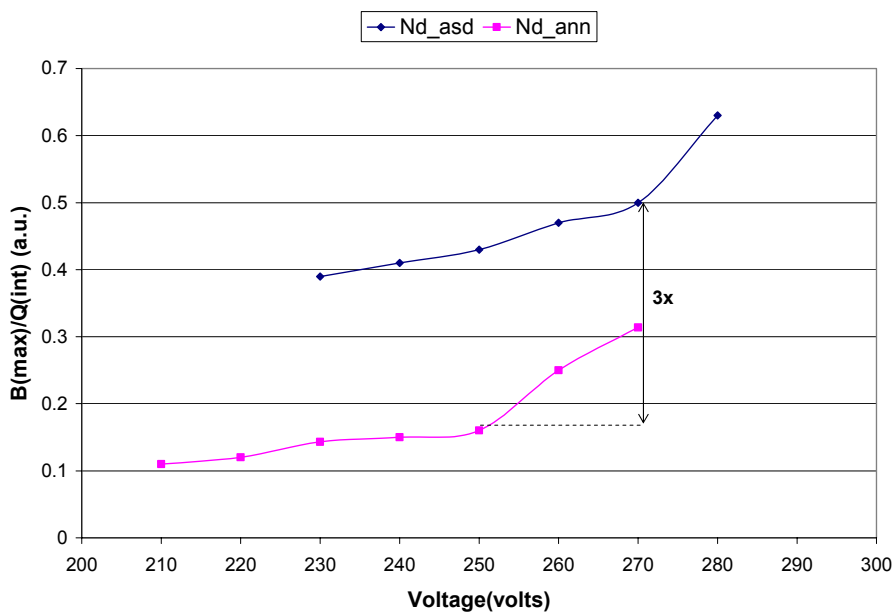
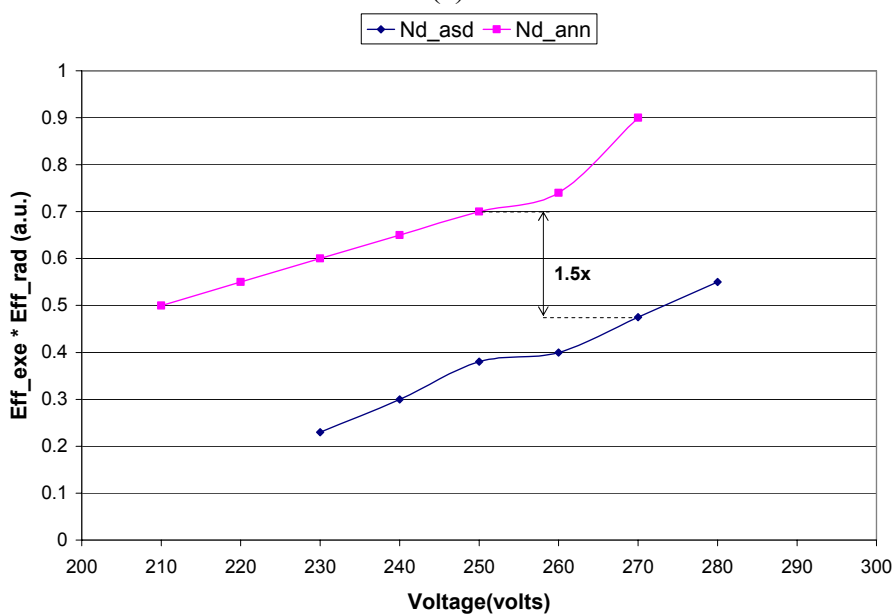


Figure 4.16 Determination of  $B_{\text{max}}$  from  $L(t)$  data. Note the necessary extrapolation back to the end of the voltage pulse.

Figure 4.17a is the  $B_{\text{max}}/Q_{\text{int}}$  ratio for the visible (600nm) transition at  $V_{40}$  for the Al (+) polarity. In this case it was observed that the excitation efficiency of the annealed sample was a factor of three smaller than the as-deposited sample. Note that this drop in excitation efficiency for the annealed sample correlates well with the drop in maximum intensity ( $B_{\text{max}}$ ) (see Figure 4.7c).



(a)



(b)

Figure 4.17 a) Excitation efficiency, ( $B_{\max}/Q_{\text{int}}$ ) versus voltage for visible transition (600nm) and b)  $\text{Eff}_{\text{exe}} \cdot \text{Eff}_{\text{rad}}$  versus voltage for near infrared transition (910nm).

The infrared excitation efficiency can also be derived in a similar manner by monitoring the  $B_{\max}$  for the infrared transition. Due to equipment limitations,  $B_{\max}$  values for the infrared transition could not be measured directly. Hence a direct ratio of  $B_{\max}/Q_{\text{int}}$

versus voltage could not be determined. In order to establish a measure the total device efficiency, we monitor a product of the excitation efficiency and the radiative efficiency ( $\text{Eff\_exe}(\eta_{\text{exe}}) * \text{Eff\_rad}(\eta_{\text{rad}})$ ) versus voltage and the results are shown in Figure 4.17b for the near infrared (910nm) transition at  $V_{40}$  for the Al (+) polarity. Annealing improved this product by a factor of 1.5 as compared to the as-deposited sample.

#### 4.6 Summary

The effects of post-deposition annealing on the optical and electrical properties half-stack ZnS:NdF<sub>3</sub> ACTFELDs were investigated. ZnS:NdF<sub>3</sub> doped thin films were deposited from two separate targets, pure ZnS and ZnS:NdF<sub>3</sub>, and annealed at temperatures ranging from 375°-425°C for 1 hr. Duty cycles of 100% on the pure ZnS target and 75% on the ZnS:NdF<sub>3</sub> target were found to result in an optimal Nd concentration of 0.9at% in the films, and result in optimal infra-red irradiance of 0.22 $\mu\text{W}/\text{cm}^2 \cdot \text{nm}$ , 0.13 $\mu\text{W}/\text{cm}^2 \cdot \text{nm}$ , 0.01 $\mu\text{W}/\text{cm}^2 \cdot \text{nm}$ , for the 910 ( ${}^4\text{F}_{3/2} \rightarrow {}^4\text{I}_{9/2}$ ), 1060 ( ${}^4\text{F}_{3/2} \rightarrow {}^4\text{I}_{11/2}$ ) and 1350 ( ${}^4\text{F}_{3/2} \rightarrow {}^4\text{I}_{13/2}$ ) nm emissions respectively. The FWHM of the 28.5° diffraction peak decreased with increasing annealing temperature suggesting that the film crystallinity was improved by annealing. TEM studies were shown to be more effective than XRD in understanding the complex film crystal structure, because it was difficult to differentiate the cubic phase from the hexagonal phase using XRD due to almost identical  $2\theta$  values at 28.5° from the cubic (111) and hexagonal (0002) planes. The films showed a predominant cubic structure in some regions, and a predominant hexagonal structure in others. B-V plots indicated that the threshold voltage for the annealed film was almost 20V smaller than that of the as-deposited film. The infrared intensity for ZnS:NdF<sub>3</sub> doped thin films for 910 and 1060nm emissions at 40V above threshold was found to increase

with annealing temperature up to 425°C, then decreased at higher anneal temperatures. Shifts in emission wavelength were observed with annealing temperature. On the contrary, the intensity for the visible 600nm ( $^4G_{5/2} \rightarrow ^4I_{9/2}$ ) emission was the lowest at 425°C, and then was observed to increase with higher annealing temperatures. ZnS:NdF<sub>3</sub> doped thin films annealed at 425°C for 1 hr showed a maximum infrared power density of 27μW/cm<sup>2</sup> for the 910nm transition and 15μW/cm<sup>2</sup> for the 1060nm transition, which were 100% larger than those from as-deposited counterparts. The luminescent decay time constant was 20μs ± 5μs for the as deposited ZnS:NdF<sub>3</sub> thin film and 10μs ± 5μs for thin films annealed at 425 °C for 1 hr. Electrical data (Q-V, C-V, and Q-F) were nearly symmetrical for Al (+) and Al (-) polarities. At 40V above threshold, the annealed films showed higher external as well as internal conduction charge density (5.58μC/cm<sup>2</sup> and 6μC/cm<sup>2</sup>) versus as-deposited films (1.85μC/cm<sup>2</sup> and 1.77μC/cm<sup>2</sup>) respectively. The Q-V and C-V plots also indicated lower thresholds and higher capacitances above thresholds for the annealed films as compared to the as-deposited films. External as well as internal conduction charge increased with annealing. The average external charge for the annealed sample improved by a factor of 3 over the as-deposited sample, whereas the internal charge improved by a factor of 3.5. Average excitation efficiency for the annealed sample dropped by a factor of 3 for the visible transition, that for the near infrared transition improved by a factor of 1.5. The origin of these effects will be discussed in chapter 6.

## CHAPTER 5 RF MAGNETRON SPUTTER DEPOSITION OF ZINC SULFIDE DOPED WITH ERBIUM ACTFEL DEVICES

### 5.1 Introduction

This chapter reports the effect of post-deposition annealing on the optical and electro-optical characteristics of RF magnetron sputtered ZnS doped ErF<sub>3</sub> ACTFEL devices. A description of the experimental procedures is given, followed by the results of the various structural, optical and electrical characterization methods utilized to study these devices. Erbium has a near infrared 1550nm optical transition, which has potential applications in optical communication. As in the previous chapter, the purpose of this study was to correlate the effect of annealing with various factors that could be responsible for improved electro-optical performance, and provide a common explanation to explain these effects. The total device efficiency and its components (outcoupling ( $\eta_{\text{opt}}$ ), excitation ( $\eta_{\text{exc}}$ ) and radiative ( $\eta_{\text{rad}}$ ) efficiencies) have already been defined in the previous chapter (section 4.2). The device performance of ZnS:ErF<sub>3</sub> thin films will be evaluated in a similar manner as we did with ZnS:NdF<sub>3</sub> thin films.

### 5.2 Experimental Procedure

‘Half-stack’ (see Section 2.3.1) ZnS:ErF<sub>3</sub> ACTFEL devices were RF magnetron sputter deposited onto standard substrates. The device fabrication process flow is shown schematically in Figure 5.1 and the details are described in this section.

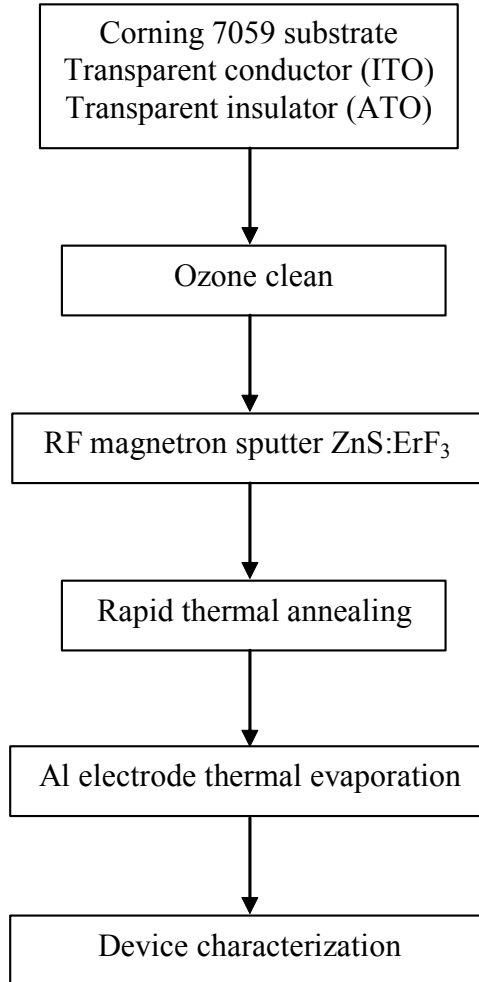


Figure 5.1 Schematic process flow diagram for ZnS:ErF<sub>3</sub> device fabrication.

### 5.2.1 Substrate Materials

The substrates used were ITO coated Corning 7059 glass substrates. The bottom Al<sub>2</sub>O<sub>3</sub>/TiO<sub>2</sub> (ATO) dielectric was deposited using atomic layer deposition, by Planar Systems, Inc. Before phosphor layer deposition, the substrates were cleaned with methanol followed by a 6 minute ozone clean to remove hydrocarbons absorbed onto the substrate surface.

### 5.2.2 Deposition of Phosphor Layer

The ZnS:ErF<sub>3</sub> layer was deposited by RF magnetron sputtering using two independently controlled sources. Pure, polycrystalline, bulk CVD grown ZnS purchased

from Morton Thiokol, Inc was used as the ZnS target and the rare earth was sputtered from a compound ZnS:ErF<sub>3</sub> target purchased from SCI engineering materials. The compound ZnS:ErF<sub>3</sub> target was prepared by mixing 1.5wt% ErF<sub>3</sub> powder with 98.5wt% ZnS powder, and hot pressing it to form the target. Several 2 × 1” substrates were placed on a sample platter rotating at a speed of 8 revolutions/minute. The sputter chamber was evacuated to a base pressure < 1 × 10<sup>-6</sup> Torr.

The phosphor brightness at 20 and 40V above the threshold voltage (B<sub>20</sub> and B<sub>40</sub> respectively, as indicated in Section 2.6.1.1) for various half-stack devices was measured and the deposition conditions evaluated and optimized. The substrate temperature was kept constant at 160°C throughout the deposition based on the aforementioned optimization. Both the ZnS and the ZnS:ErF<sub>3</sub> targets were run at a power of 120W with duty cycles of 100% for both targets. Argon, at a pressure of 20mTorr was used as the sputtering gas. The typical film thickness was 0.86μm ± 10%. The resulting growth rate was ~ 50-60Å/min. The sample platter capable of holding several substrates for simultaneous processing, allows various post-deposition processing conditions to be compared using phosphor films deposited under identical conditions. One bare glass substrate partially covered with a micro slide to create a step was included in each run to measure film thickness by profilometry.

A custom quartz lamp-heated rapid thermal anneal (RTA) chamber was used to anneal the devices under flowing N<sub>2</sub>. The sample was placed on a polished Si wafer during heating to help prevent contamination of/from the RTA chamber. A thermocouple placed adjacent to the sample, recorded the temperature. To study the effect of annealing on device performance, a number of annealing temperatures in the range of 300°C-475°C

were selected. The standard processing conditions employed 1 hour anneals with a 90 second ramp time up to the desired temperature and complete shutoff of the furnace during cooling.

### 5.2.3 Device Completion

Thermal evaporation of Al ( $0.079\text{cm}^2$ ) through a shadow mask using an Edwards evaporation system, formed the top electrode. Typical base pressures for this process were  $1 \times 10^{-6}$  Torr. Contact to the bottom (ITO) electrode was achieved by scratching through the upper insulating layers with a diamond scribe, then melting pure indium metal onto the scratched area which wets the ITO layer, thereby establishing electrical contact.

## 5.3 Experimental Results

### 5.3.1 Structural and Chemical Characterization

#### 5.3.1.1 Thin film concentration

The as-deposited and annealed films were then analyzed to verify the rare earth concentration (Er) in the films. From previous studies, the optimum rare earth (dopant) concentration for maximum brightness of ACTFEL devices has been observed to be in the range of 1-2 at%. Too much dopant in the film also leads to concentration quenching which effectively reduces the device brightness. Hence it is extremely important to obtain the correct concentration of dopant in the films in order that optimal optical output may be realized. The dopant concentration was measured using a JOEL Superprobe 733 (EPMA), which uses four crystals for element identification and quantification. Rare earth standards were used to quantify the exact concentration of Er in the films. Five to six different areas of the film were measured and the average concentration of Er in the films was found to be  $\sim 1.0$  at%.

### 5.3.1.2 X-ray diffraction (XRD)

As stated in Chapter 3, XRD provides information regarding the film quality and crystallinity. XRD data was collected using a Philips APD 3720 powder diffractometer. As before, four different conditions were chosen for the ZnS:ErF<sub>3</sub> films, specifically as-deposited films and films annealed at 375°C, 425°C and 475°C for 1 hr each respectively. The scan range used was 27°-31° (2 $\theta$ ) at a scan rate of 0.005°/sec. The peak observed at 28.5° is an overlapped peak from the (111) plane of the cubic phase and the (0002) plane of the hexagonal phase. The full width half maximum (FWHM) of the 28.5° peak was used as a measure of the ZnS:ErF<sub>3</sub> thin film crystallinity. As shown in Figure 5.2, the FWHM of the 28.5° peak decreases, (reduces from 0.65° to 0.5°) as the annealing temperature increases, indicating improved crystallinity.

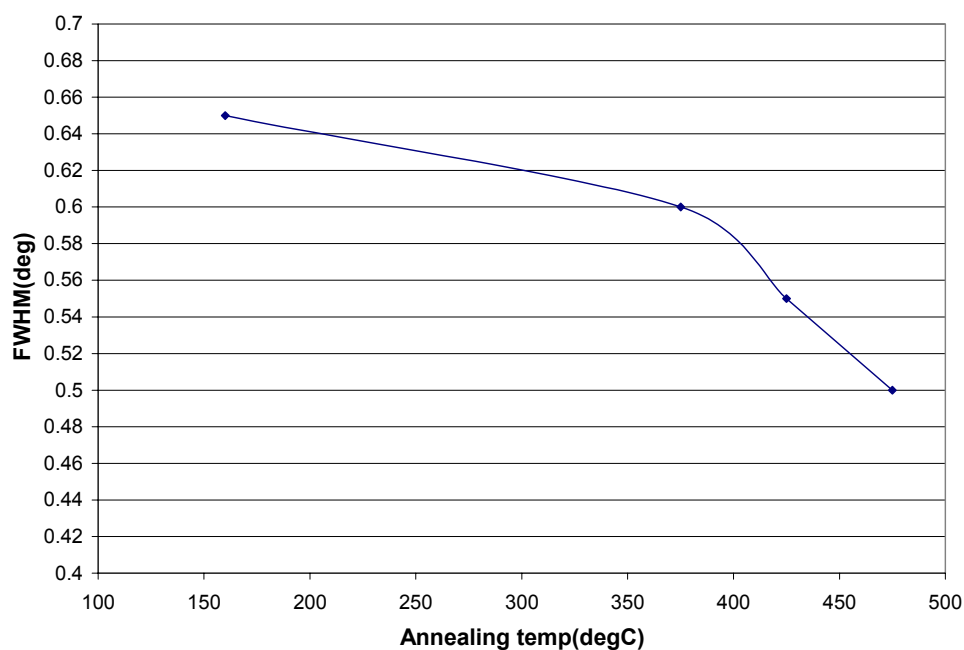
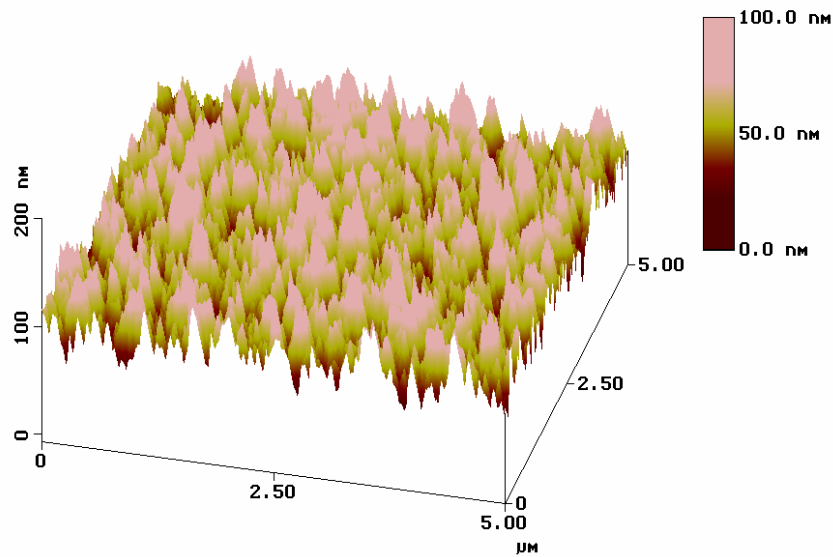


Figure 5.2 Effect of annealing temperature on the FWHM of the 28.5° X-ray diffraction peak from the ZnS:ErF<sub>3</sub> film.

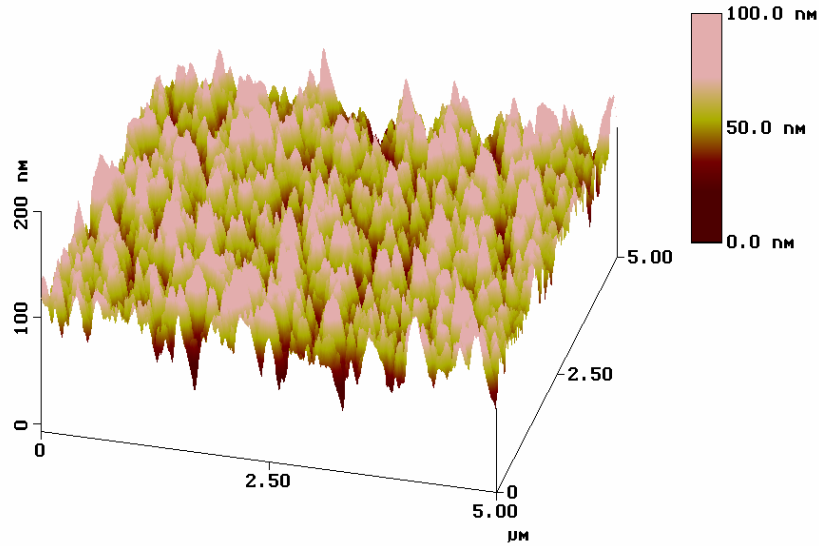
### 5.3.1.3 Atomic force microscopy (AFM)

Surface roughness can significantly affect the brightness of the device by affecting the outcoupling efficiency (see section 2.4.5). As-deposited films and films annealed at 425°C for 1 hr films were measured to study changes in surface roughness. Figure 5.3 shows the actual surface morphology from AFM for as-deposited (a) and annealed ZnS:ErF<sub>3</sub> samples (b). The RMS surface roughness valued for the as-deposited and annealed (425°C for 1 hr) films was measured to be 15 and 14 nm respectively. Negligible changes ( $\pm 10\%$ ) in the surface roughness were observed between the two samples, suggesting that outcoupling efficiency did not vary with annealing (see below).



(a) As-deposited ZnS:ErF<sub>3</sub> thin film (RMS = 15nm)

Figure 5.3 AFM surface morphologies of a) as-deposited and b) annealed at 425°C for 1 hr ZnS:ErF<sub>3</sub> thin films.



(b) Annealed 425°C for 1 hr ZnS:ErF<sub>3</sub> thin film (RMS = 14)

Figure 5.3 continued.

### 5.3.2 Optical Characterization

#### 5.3.2.1 Brightness-voltage (B-V) plots

The brightness vs. voltage behavior of the as deposited and annealed at 425°C for 1 hr half cell ZnS:ErF<sub>3</sub> devices is shown in Figure 5.4. Emitted light was collected and analyzed using a fiber optic cable connected to an Ocean Optics 2000 spectrometer with variable gratings. As we were mainly interested in the infrared electroluminescence, the wavelength monitored for this plot was 990nm. It should be noted that the turn on voltage for the visible transition at 545nm was also the same as that for the 990nm and the 1550nm. The threshold voltage and brightness values at 40 V above threshold ( $B_{40}$ ) were derived from these B-V data. From these plots, the threshold voltage for the as-deposited sample was observed to be 185V, indicating  $V_{40}$  equal to 225V. The threshold for the annealed sample it was 160V, making  $V_{40}$  equal to 200V. The as-deposited and annealed devices were operated at these respective  $V_{40}$  values (185V for as-deposited and 160V for annealed) to measure and compare the brightness and efficiencies for the two devices.

The point to be noted is the difference in turn-on voltages for the as-deposited and annealed samples. Outcoupling efficiencies for the as-deposited and annealed samples can be compared by collecting diffuse reflectance data for both samples. The values of diffuse reflectance for the as-deposited and annealed samples did not vary significantly (~10% variation between the as-deposited and annealed samples). The data are shown in Figure 5.5.

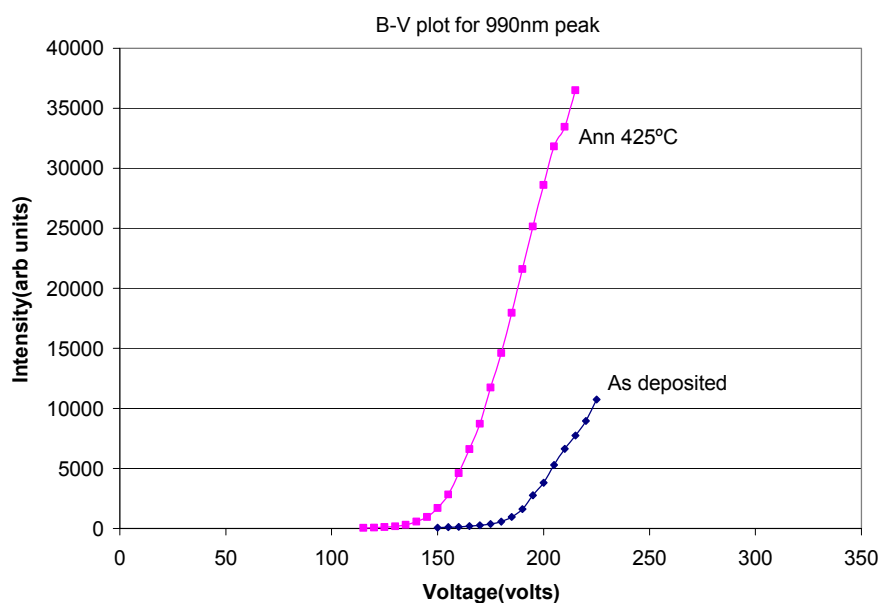


Figure 5.4 Brightness vs. voltage behavior as a function of annealing treatment.

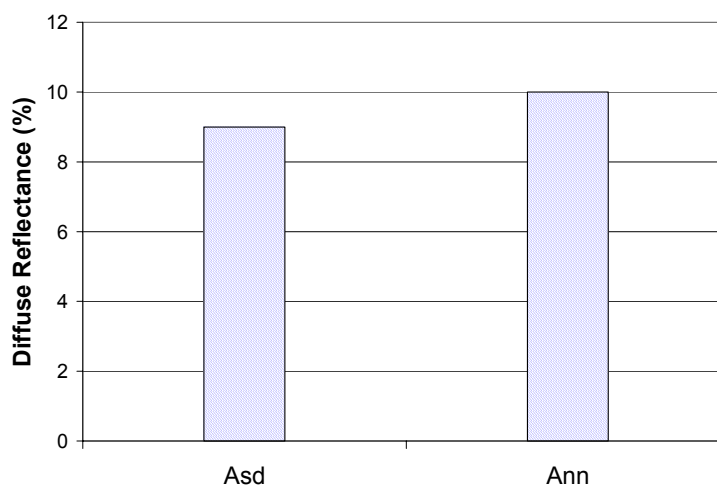
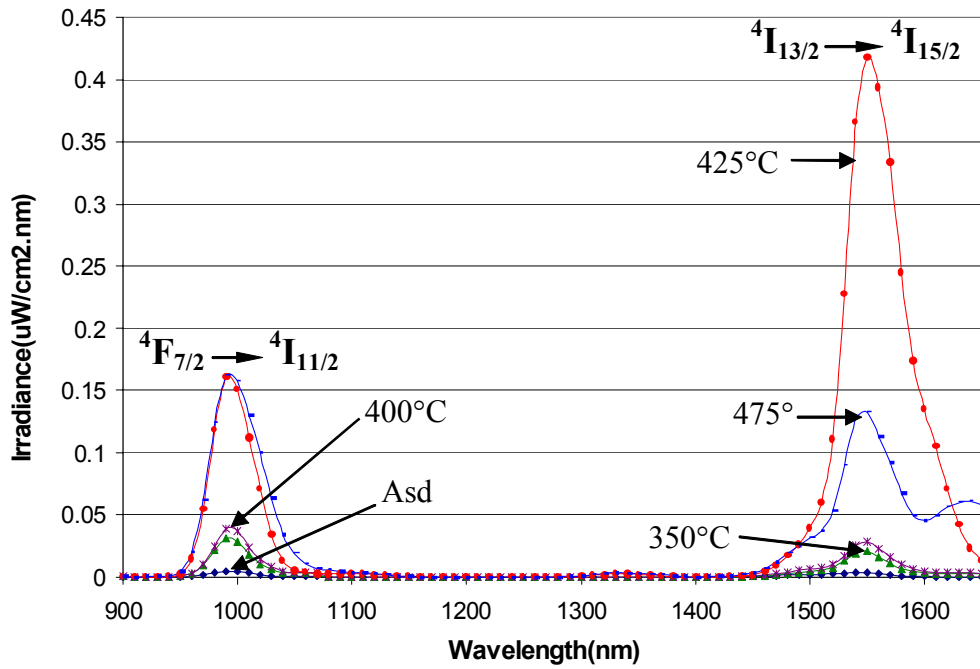


Figure 5.5 Diffuse reflectance values for as-deposited and annealed (425°C for 1 hr) ZnS:ErF<sub>3</sub> films.

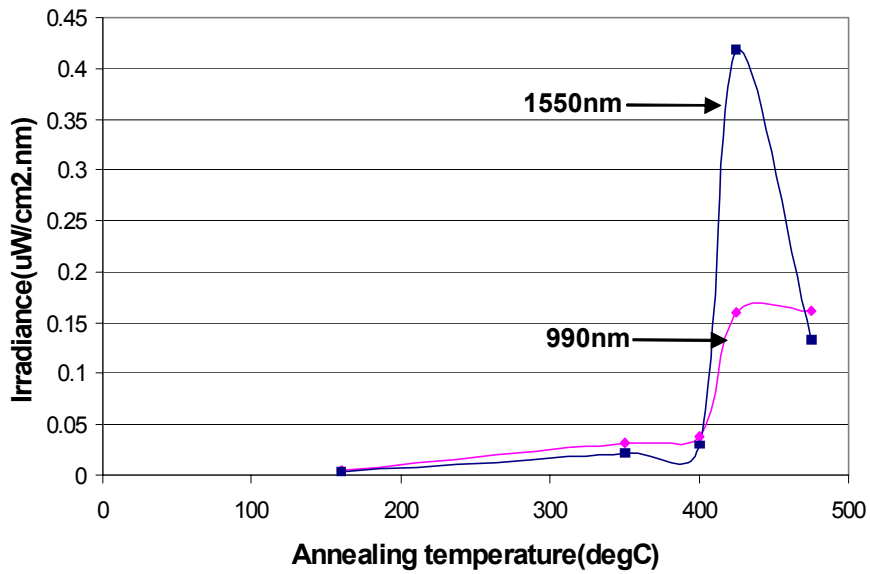
### 5.3.2.2 Effect of annealing on infrared electroluminescence of ZnS:ErF<sub>3</sub> thin film devices

As mentioned in the chapter 4, electroluminescent emission (EL) was excited by applying 2.5kHz positive and negative trapezoidal voltage pulses, 30 $\mu$ s in length with 5 $\mu$ s rise and fall times. The spectrometer used for analysis of the emitted light has been previously described in Chapter 3.

The effect of annealing on the NIR EL emission from ZnS:ErF<sub>3</sub> is shown in Figure 5.6a. The highest irradiance peak at 1550nm originates from the  $^4I_{13/2} \rightarrow ^4I_{15/2}$  Er ion radiative relaxation, whereas the 990nm peak originates from the  $^4F_{7/2} \rightarrow ^4I_{11/2}$  transition [85]. The intensities of both the 990nm and the 1550nm emissions were found to increase with annealing temperature. The wavelengths of these emission peaks remain constant with annealing unlike in the case of neodymium, where they were observed to shift with annealing temperature. The EL intensity of the 1550nm peak increased with anneals up to 425°C, but decreased at higher annealing temperatures (see Figure 5.6b). Likewise, the intensity of the 990nm peak increased with anneals up to 425°C, but remained constant at higher anneals up to the maximum temperature (475°C). The output power density was calculated by integrating the area under the peaks. As depicted in Figure 5.6c, at 1550nm the EL power density for the sample annealed at 425°C was  $\sim 30x$  that of the as-deposited sample. An improvement of  $\sim 8x$  was obtained at 990nm. The specific improvement in power density achieved by annealing was  $\sim 28\mu\text{W}/\text{cm}^2$  at 1550nm and  $\sim 7\mu\text{W}/\text{cm}^2$  at 990nm.

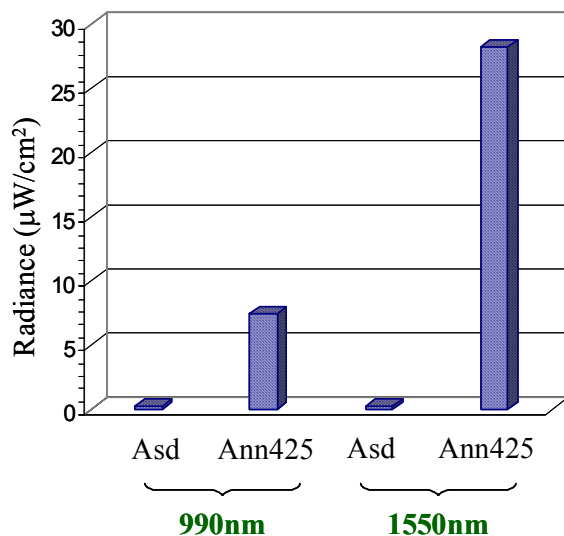


(a)



(b)

Figure 5.6 Effect of annealing on the IR EL emission from ZnS:ErF<sub>3</sub> thin films. (a) EL spectrum showing no shift in emission wavelength, and (b) plot of irradiance versus annealing temperature for the 990 and 1550 nm peaks, (c) comparison of EL for as deposited and annealed sample.



(c)

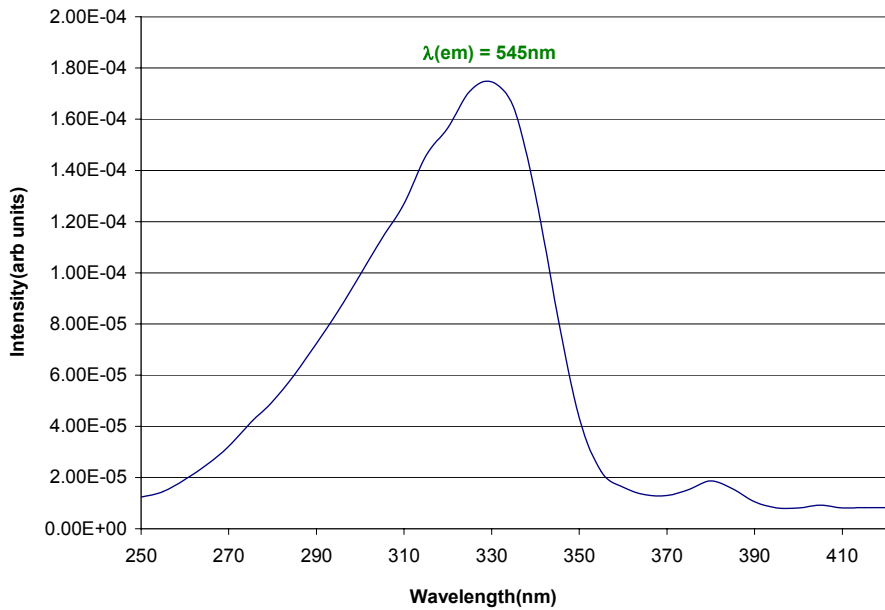
Figure 5.6 continued.

### 5.3.2.3 Photoluminescence (PL) characterization (room temperature)

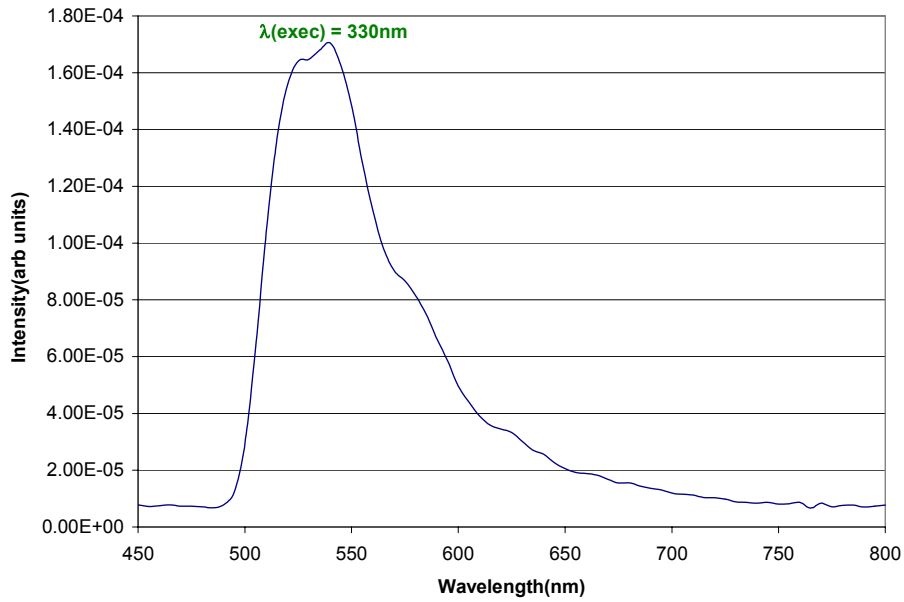
Photoluminescence measurements were employed to study the zero field energy level positions associated with light emission. A ‘white’ Xenon lamp was used together with a monochromator in order to obtain PL excitation (PLE) spectra from 250 to 1250nm. As discussed earlier, a photomultiplier tube was used for analysis of the visible emission whereas a thermoelectrically cooled germanium photodiode detector was used to monitor the infrared emission.

Neither visible nor infra-red photoluminescence was observed from the as-deposited ZnS:Er samples. Green photoluminescence visible to the naked eye was observed from the sample annealed at 425°C upon excitation at 330 nm . To find the optimum excitation wavelength for 545nm visible emission, the emission monochromator was fixed at a wavelength of 545nm, and the source monochromator was scanned from 250nm to 425nm. In other words, a photoluminescence excitation spectrum was obtained.

As shown in Figure 5.7a, the optimum excitation wavelength for 545nm emission was 330nm. The photoluminescence emission spectrum over the range of 450nm to 800nm using 330nm excitation is presented in Figure 5.7b. These two plots provide good insight to of PL emission and PLE excitation behavior in the visible region.



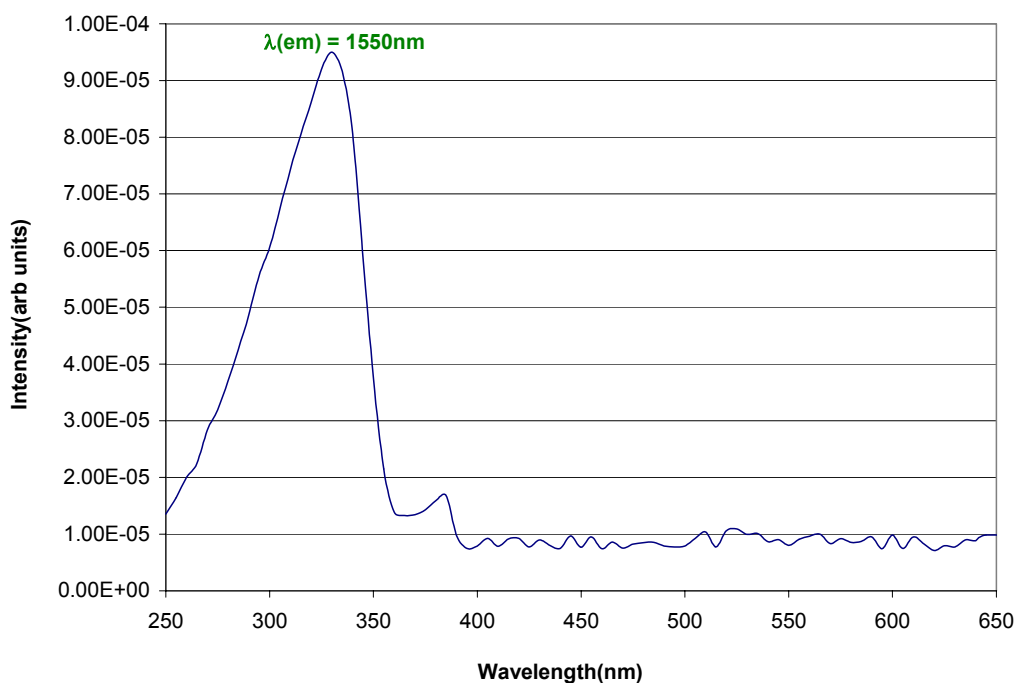
(a)



(b)

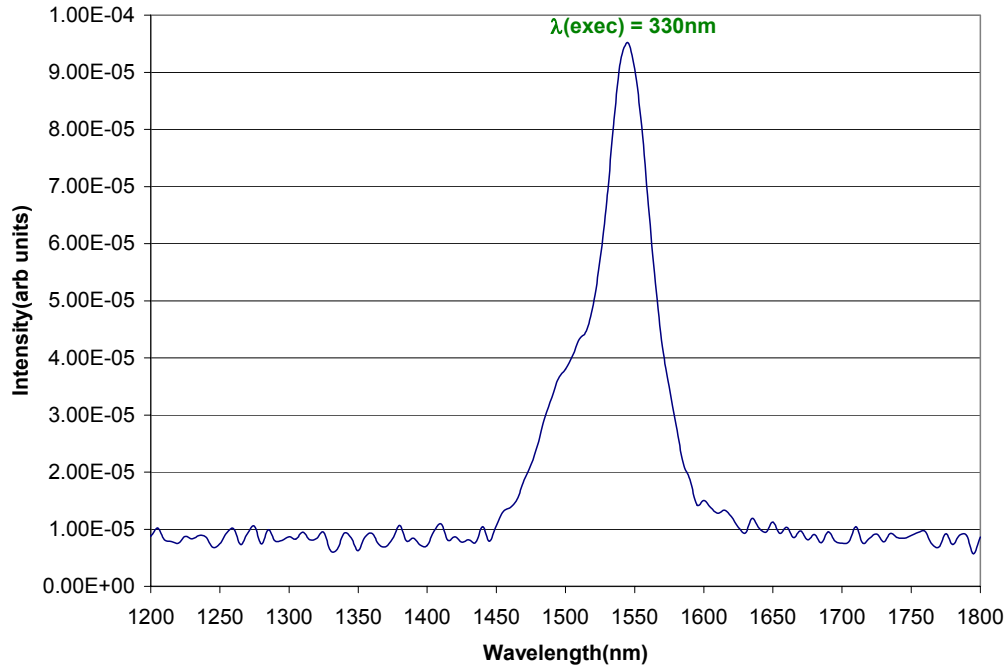
Figure 5.7 Visible PL/PLE spectrum for annealed ZnS:ErF<sub>3</sub> thin film (a) PLE spectrum, and (b) PL spectrum.

As pointed out earlier, the 1550nm infrared emission from  $\text{Er}^{3+}$  overlaps the absorption minimum region of silica based optical fibers, and hence is potentially useful for applications in optical communications. Using the procedure described above, the detection wavelength on the Germanium detector was fixed at 1550nm and the source monochromator was scanned over the range of 250nm to 650nm (see Figure 5.8a). The excitation maximum for the 1550nm transition was found to also be 330nm. Once this was established, the excitation source was fixed at 330nm a PL emission spectrum taken over the range of 1200nm to 1800nm (see Figure 5.8b). It should be remembered from these plots that the optical threshold is the same for the visible (545nm) and the infrared (1550nm) transition, which suggests that the main issue to be discussed is de-excitation rather than excitation from these respective states.



(a)

Figure 5.8 Infrared PL/PLE spectrum for annealed  $\text{ZnS:ErF}_3$  thin film (a) PLE spectrum, and (b) PL spectrum.



(b)

Figure 5.8 continued.

#### 5.3.2.4 Luminescence decay characterization (room temperature)

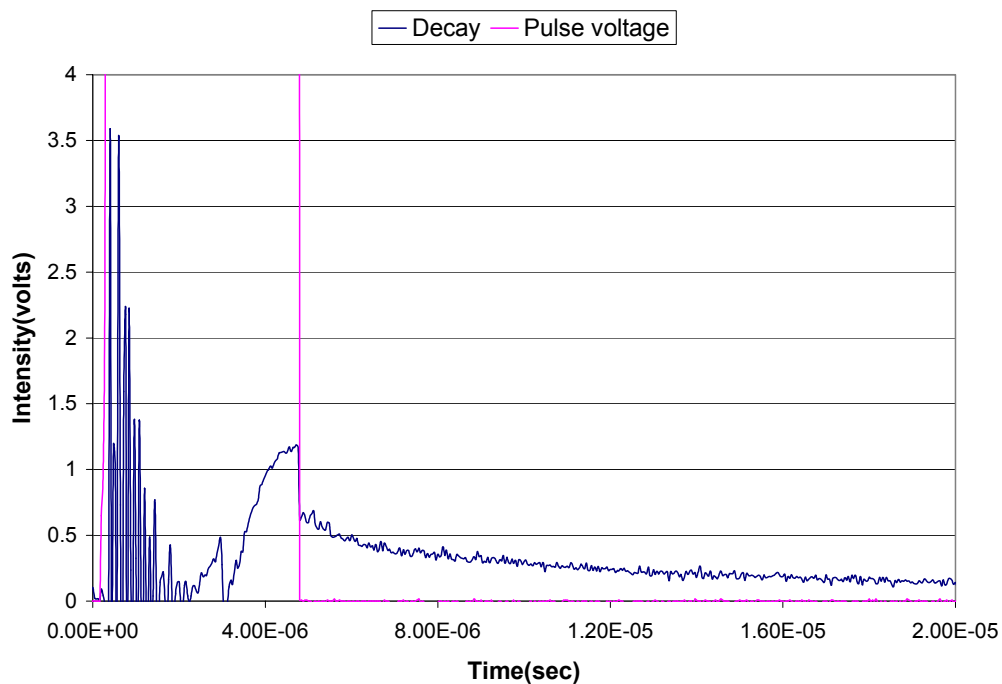
Luminance versus time ( $L(t)$ ) data were collected on the oscilloscope by monitoring the signal output from a Si-diode photomultiplier tube (PMT) manufactured by Oriel. The setup for collecting the luminescence decay data is described in detail in section 4.4.2.3. In addition to the waveform generator and PMT, a Tektronix TDS 510A digitizing oscilloscope was used to monitor the luminescence and the voltages at different positions in the circuit (as shown in Figure 4.8) as a function of time. The oscilloscope monitors the luminescence behavior as well as the conduction current as a function of the applied voltage. Trapezoidal 2.5kHz frequency pulses were applied to the device with rise, fall and dwell times of  $5\mu\text{s}$  each and the devices was operated at  $V_{40}$  voltage. A short pulse width of  $5\mu\text{s}$  was chosen over a longer one ( $30\mu\text{s}$ ), since it enables us to measure the luminescence decay behavior during and at the end of the pulse, whereas with the

30 $\mu$ s pulse the luminescence starts to decay even before the pulse ends. As in the case of neodymium, the infrared transitions could not be measured due to limitations and hence only the visible 545nm emission ( $^4S_{3/2} \rightarrow ^4I_{15/2}$ ) for erbium was monitored to study the electroluminescence decay behavior. Luminescence data was collected for an entire pulse (Al<sup>+</sup> and Al<sup>-</sup> polarities), but for better viewing only the Al<sup>+</sup> polarity data has been plotted.

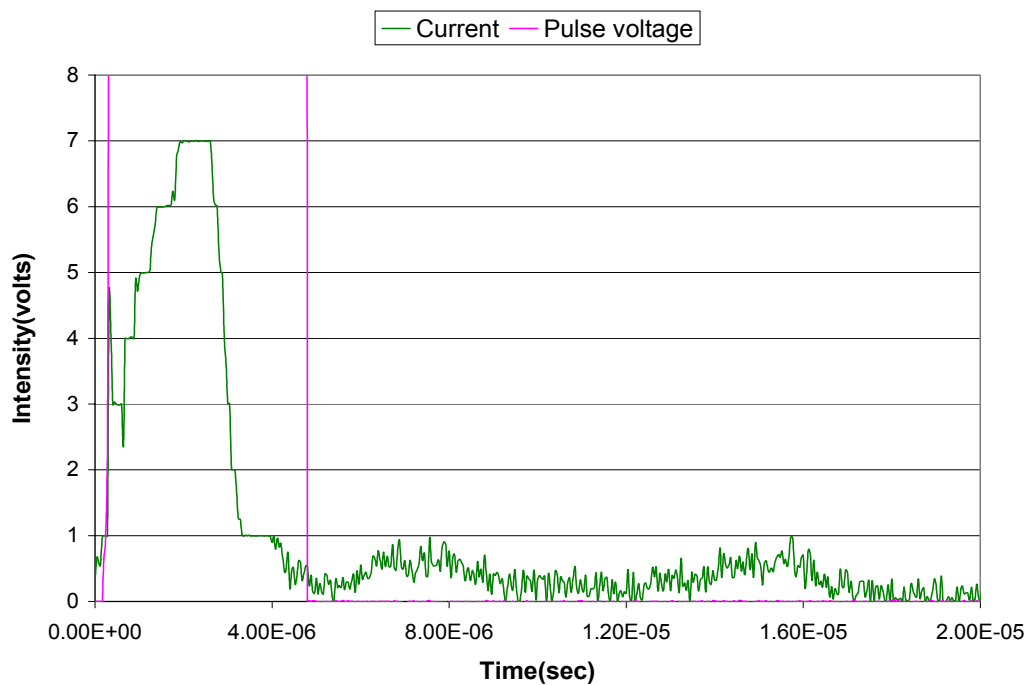
Figure 5.9a shows the luminescence decay behavior and applied voltage pulse of the as deposited ZnS:ErF<sub>3</sub> film versus time. The luminescence was observed at the rising edge of the voltage pulse and then decays near zero, within 20 $\mu$ s suggesting a shorter lifetime.

To better understand the EL decay data, the conduction current through the device was monitored as a function of the applied voltage (Figure 5.9b). Figure 5.9b shows the conduction current behavior and the pulse voltage versus time. It was clearly observed that the current through the device increased during the pulse but dropped down to zero at the end of the pulse. There was no evidence of current flow after the end of the voltage pulse.

From the above plots, luminescence and current behavior with respect to time were derived and shown on a common plot (Figure 5.9c). The drop in the current and the onset of luminescence decay seem to correspond well with the trailing edge of the applied voltage pulse (as seen from Figures 5.9a and 5.9b).

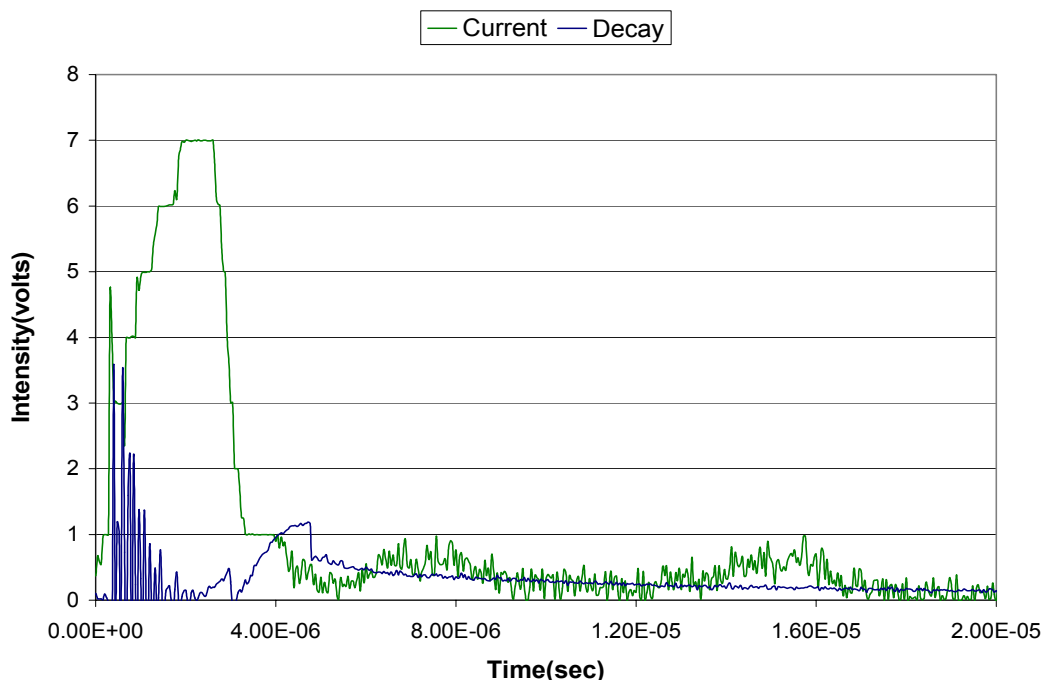


(a)



(b)

Figure 5.9 Luminescence decay behavior for as deposited ZnS:ErF<sub>3</sub> thin film operated at  $V_{40}$ , 2.5kHz frequency, 5 $\mu$ s pulse width. (a) luminescence decay and applied voltage, (b) conduction current and applied voltage, and (c) luminescence decay and conduction current versus time.



(c)

Figure 5.9 continued.

To obtain a value for the decay constant, the luminescence data in Figure 5.9 was fitted utilizing two exponentials. Figure 5.10 shows the un-smoothed time resolved luminescence decay data (black line), which was subsequently smoothed to minimize the noise, for an as deposited ZnS:ErF<sub>3</sub> thin film.

As seen from the plot, it was impossible to fit the curve with a single exponential and hence we utilized a double exponential to fit the data (red line). The decay curve consists of a sharp initial component from  $I = 0.48$  (arb. units) to  $I = 0.15$  (arb. units) with a time constant of  $5.5\mu\text{s} \pm 2\mu\text{s}$  followed by a relatively slower component from  $I = 0.15$  (arb. units) to  $I = 0.08$  (arb. units) with a time constant of  $30\mu\text{s} \pm 5\mu\text{s}$ .

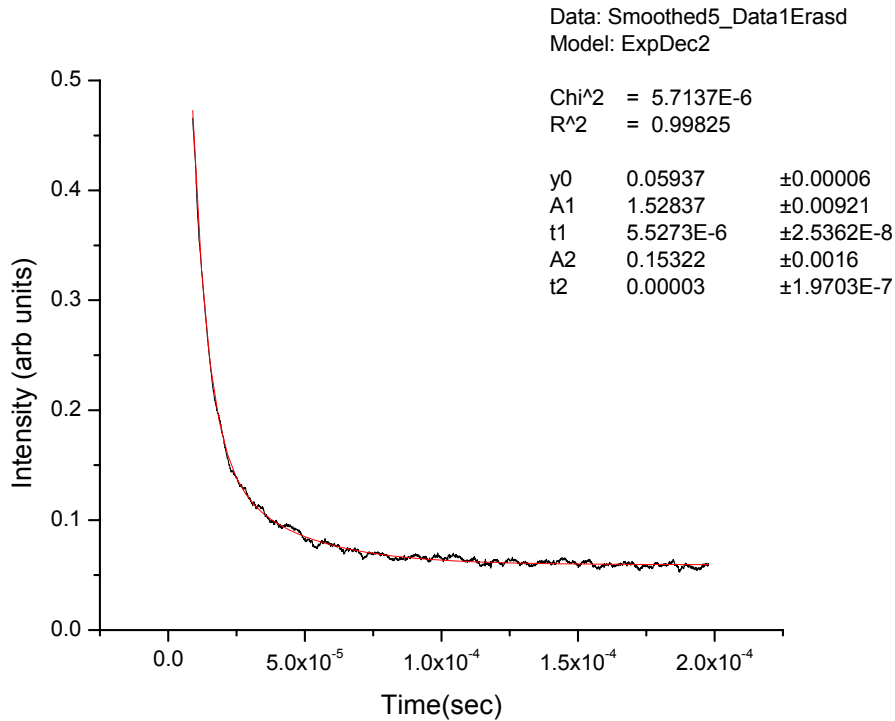


Figure 5.10 Time resolved luminescence decay data for ZnS:ErF<sub>3</sub> as deposited thin film.

Similar to the as deposited ZnS:ErF<sub>3</sub>, the luminescence decay data for the 545nm visible emission ( $^4S_{3/2} \rightarrow ^4I_{15/2}$ ) for the annealed film was also studied. Using the same pulse voltage width of 5 $\mu$ s, luminescence decay data was collected in a similar way.

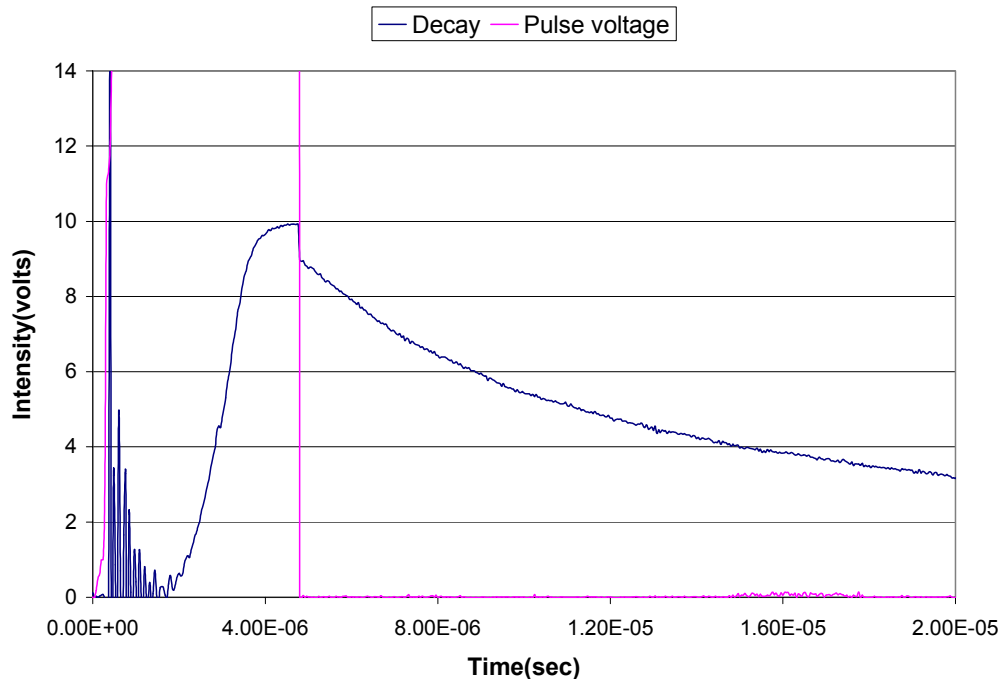
Figure 5.11a shows the luminescence decay behavior and applied voltage pulse for the annealed ZnS:ErF<sub>3</sub> film versus time. For the annealed film, the signal to noise ratio (10 times) was much higher than the as deposited film (1.5 times). Luminescence is seen to rise during the rise of the pulse and then decays almost to zero with the trailing edge of the pulse.

Figure 5.11b shows the conduction current behavior and the pulse voltage versus time. As before, it was clearly seen that the current through the device increased during the pulse but dropped down to zero at the end of the pulse.

From the above plots, luminescence and current behavior with respect to applied voltage was derived and shown on a common plot (Figure 5.11c). The drop in the current and the onset of luminescence decay correspond well with the shutting of the applied voltage pulse.

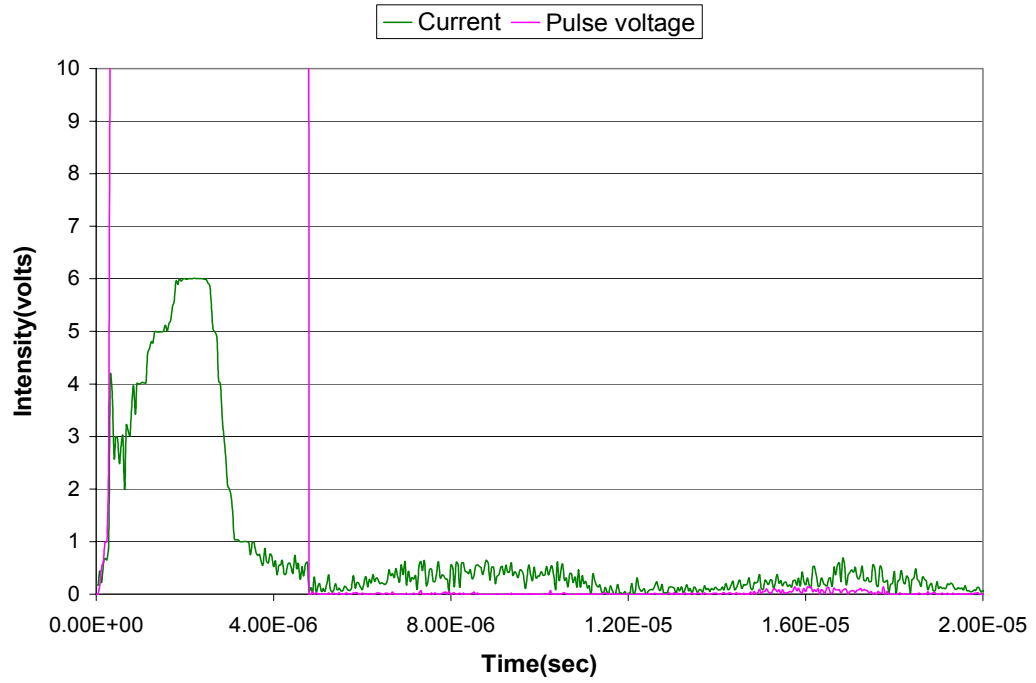
Figure 5.12 shows the un-smoothed resolved luminescence decay data (black line), which was subsequently smoothed to minimize the noise, for the annealed ZnS:ErF<sub>3</sub> thin film. As seen before, the data had to be fitted utilizing a double exponential function (red line) since it was impossible to fit it using a single exponential.

Again, the data were best fitted with two consecutive (from  $I = 8$  (arb. units) to  $I = 2$  (arb. units) with a time constant of  $7\mu\text{s} \pm 2\mu\text{s}$ , and from  $I = 2$  (arb. units) to  $I = 0.8$  (arb. units) with a time constant of  $40\mu\text{s} \pm 5\mu\text{s}$ ).

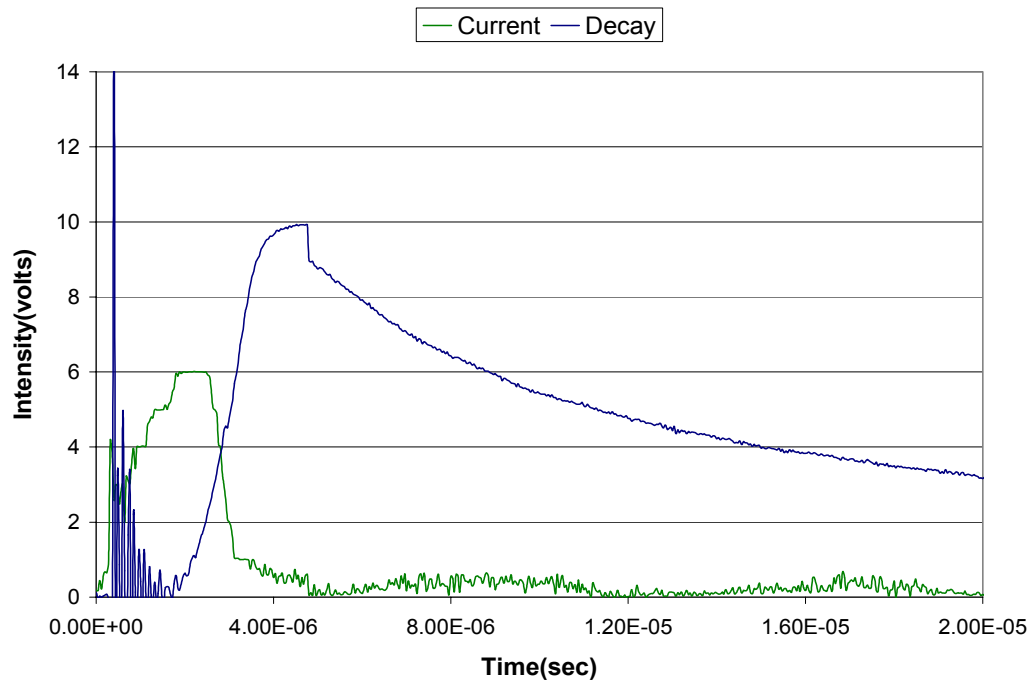


(a)

Figure 5.11 Luminescence decay behavior for annealed ZnS:ErF<sub>3</sub> thin film operated at  $V_{40}$ , 2.5kHz frequency,  $5\mu\text{s}$  pulse width. (a) luminescence decay and applied voltage, (b) conduction current and applied voltage, and (c) luminescence decay and conduction current versus time.



(b)



(c)

Figure 5.11 continued.

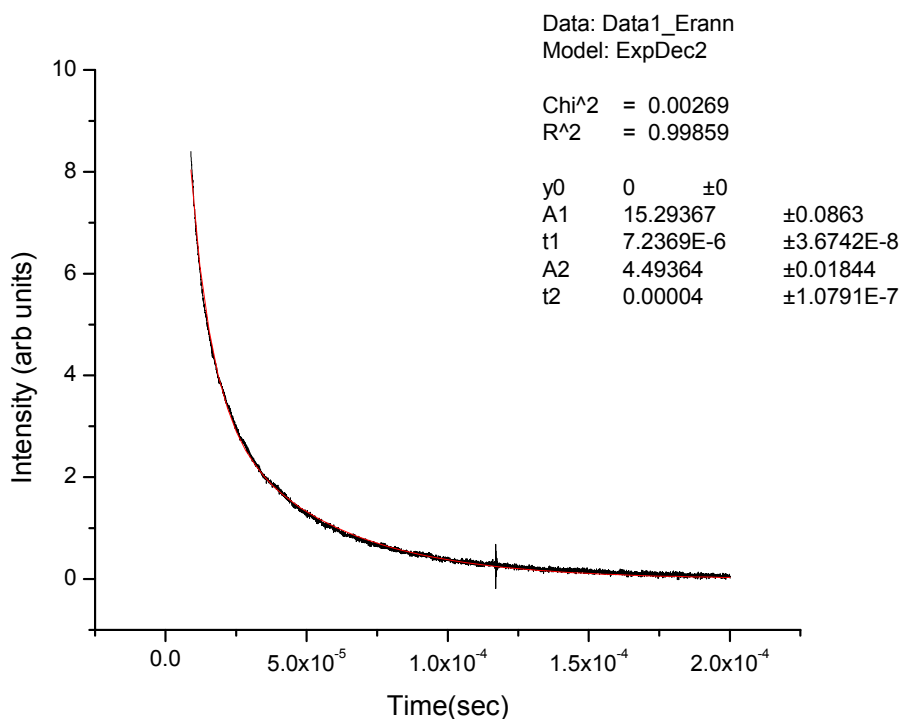


Figure 5.12 Time resolved luminescence decay data for ZnS:ErF<sub>3</sub> annealed thin film.

### 5.3.3 Electrical Characterization

The significance of and importance for measuring electrical properties were already discussed in chapters 2 and chapter 3, respectively. Similar to the procedure followed in chapter 4 for ZnS:NdF<sub>3</sub> samples, ZnS:ErF<sub>3</sub> thin film samples were characterized for measuring their electrical properties. A circuit similar to that shown in Figure 4.8 was used. The Q-V plot in Figure 5.13 shows the external charge ( $Q_{\text{ext}}$ ) versus applied voltage ( $V_{\text{EL}}$ ) on the EL device at 40V above threshold respectively for as deposited and annealed 425°C for 1 hr ZnS:ErF<sub>3</sub> thin film samples. These Q-V data are for combined Al (+) and Al (-) polarities. All measurements were done utilizing a 128Ω resistor as sense element.

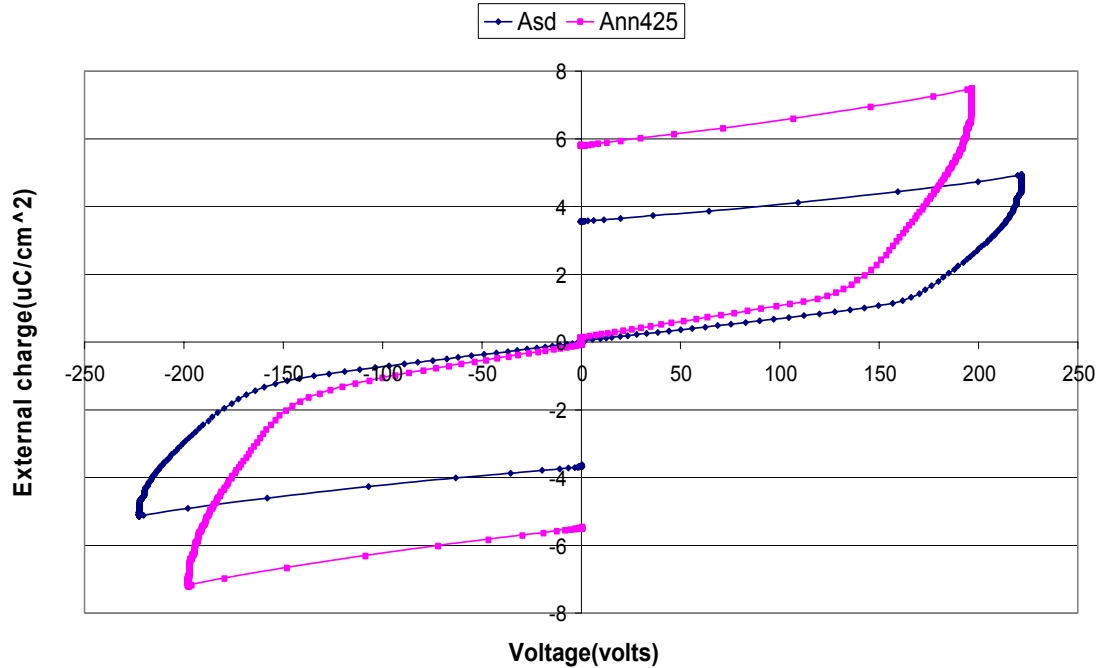


Figure 5.13 External charge ( $Q_{\text{ext}}$ ) versus applied voltage ( $V_{\text{EL}}$ ) for Al (+) and Al (-) polarities at 40V above threshold for as deposited and annealed at 425°C for 1 hr ZnS:ErF<sub>3</sub> thin film samples.

Figure 5.13 shows that there is more average conduction charge for the annealed sample with respect to the as deposited sample. At 40V above threshold, the average external conduction charge for the annealed sample ( $5.87\mu\text{C}/\text{cm}^2$ ) was almost 55% more than that of the as deposited sample ( $3.8\mu\text{C}/\text{cm}^2$ ). We also observed that the turn on voltage was significantly smaller for the annealed sample (160V) than the as deposited sample (185V). It was also seen that the slope of the Q-V plot for annealed sample before electrical turn on was higher than that for the as deposited sample.

Capacitance-voltage plots were generated for the as deposited and annealed samples as well. The results are shown in Figure 5.14. It was seen that the above turn on capacitance value for the annealed sample was much higher than that of the as deposited sample. Another feature seen was the rigid shift of the turn on to a lower voltage for the annealed sample.

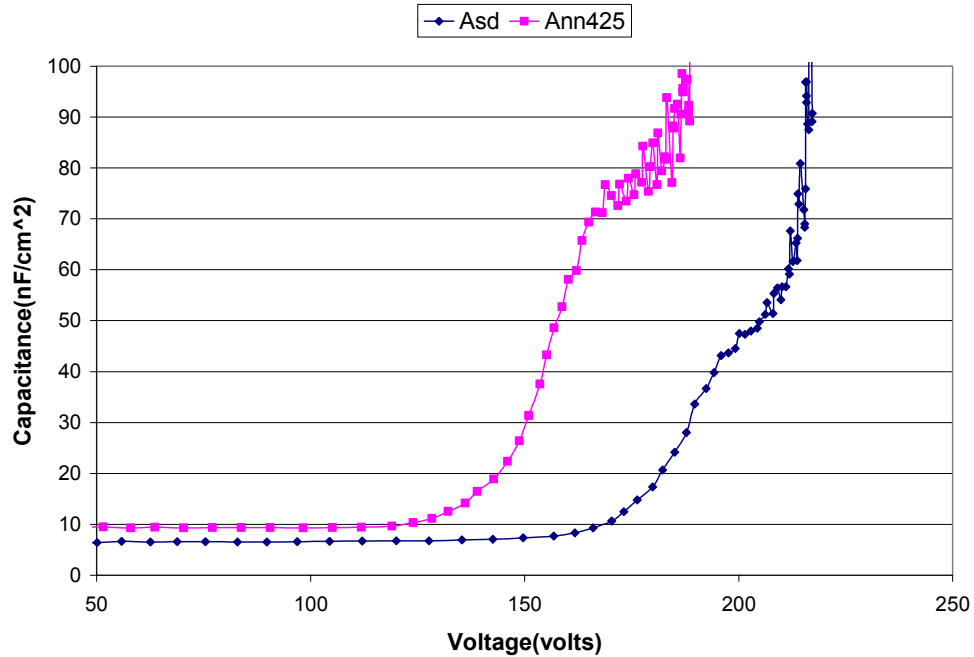


Figure 5.14 Capacitance (C) versus applied voltage ( $V_{EL}$ ) for Al (+) polarity at 40V above threshold for as deposited and annealed at 425°C for 1 hr ZnS:ErF<sub>3</sub> thin film samples.

The internal charge ( $Q_{int}$ ) versus phosphor field ( $F_p$ ) data gives more accurate information about the device physics and eliminates some of the limitations of the Q-V plot (as mentioned in chapter 4). The  $Q_{int}$ -  $F_p$  plots give true magnitudes of the internal charges and values can be directly correlated as there is no external component. Figure 5.15 shows internal charge ( $Q_{int}$ ) versus phosphor field ( $F_p$ ) data for as deposited and annealed ZnS:ErF<sub>3</sub> thin film samples at 40V above threshold for the Al (+) and Al (-) polarities.

As seen from Figure 5.15, the magnitude of average internal charge for the annealed sample ( $6.1\mu\text{C}/\text{cm}^2$ ) was also almost 55% greater than that for the as deposited sample ( $3.93\mu\text{C}/\text{cm}^2$ ). The  $Q_{int}$ - $F_p$  data show a steady state field ( $F_{ss}$ ) of 2.1MV/cm for the as deposited sample versus 1.8MV/cm for the annealed sample.

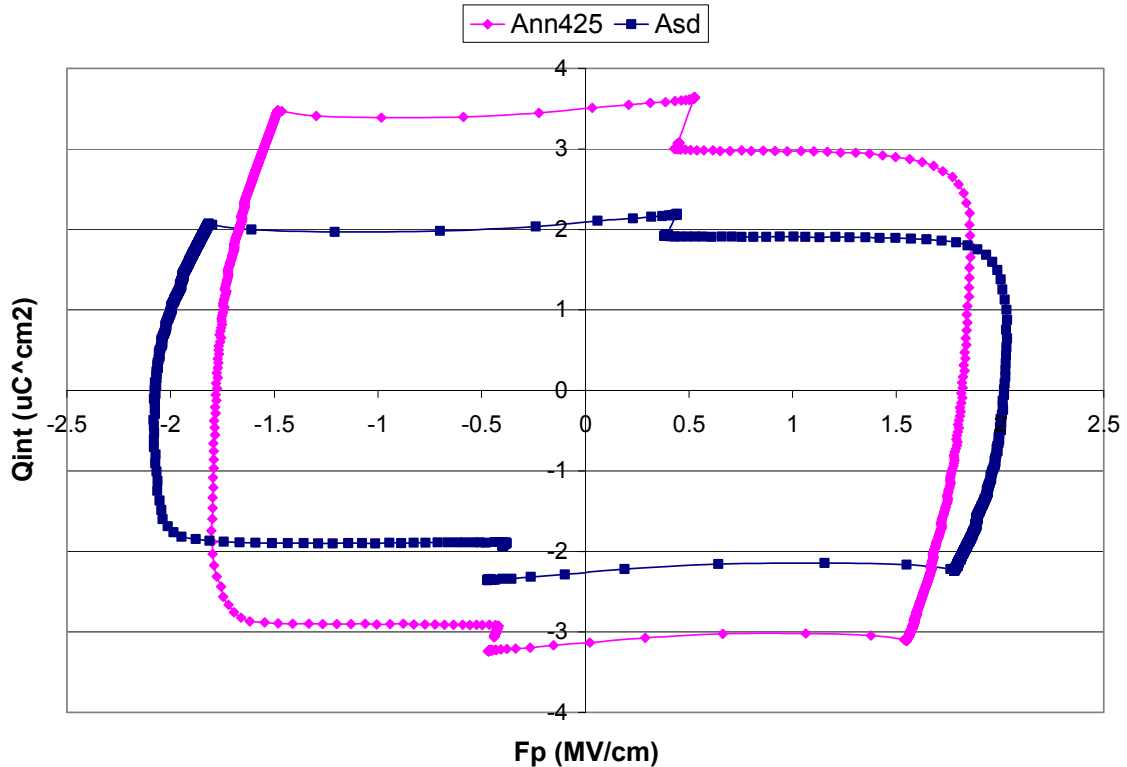
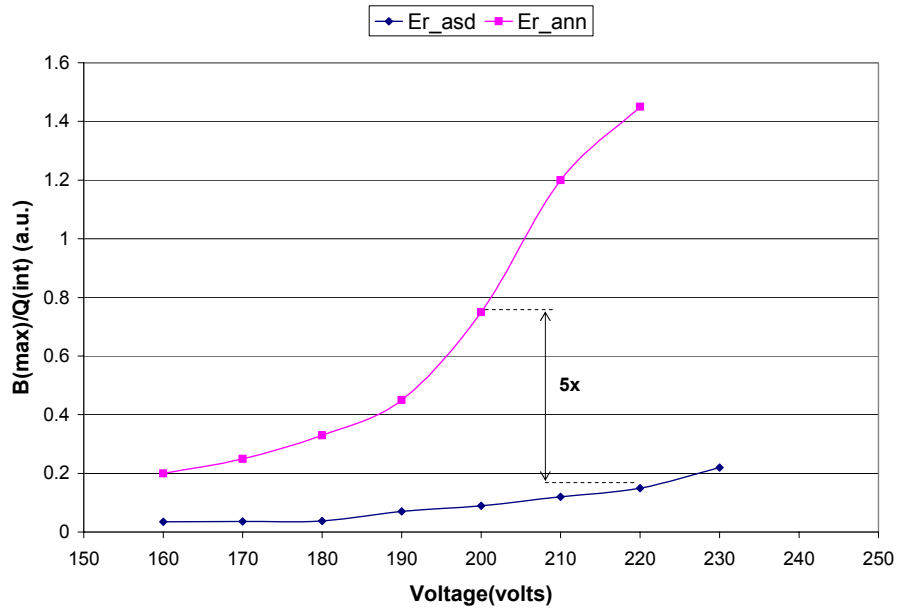


Figure 5.15 Internal charge ( $Q_{int}$ ) versus phosphor field ( $F_p$ ) for Al (+) and Al (-) polarities at 40V above threshold for as deposited and annealed at 425°C for 1 hr ZnS:ErF<sub>3</sub> thin film samples.

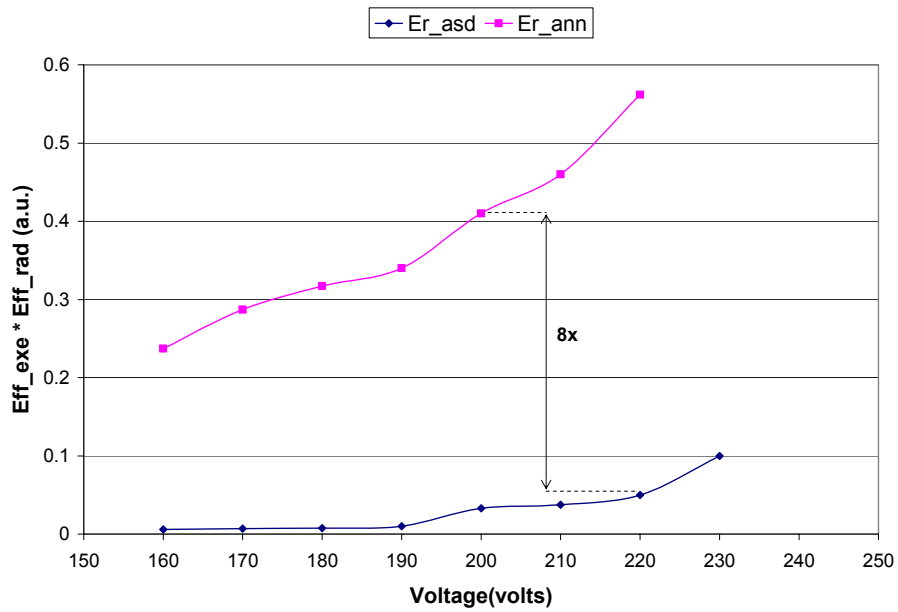
As mentioned in chapter 4 (section 4.2.2), the excitation efficiency can be estimated by dividing the maximum brightness ( $B_{max}$ ), by the transferred internal conduction charge ( $Q_{int}$ ). Figure 5.16a monitors the  $B_{max}/Q_{int}$  ratio for the visible (545nm) transition at  $V_{40}$  for the Al (+) polarity. In this case it was observed that the excitation efficiency of the annealed sample was a factor of 5 larger than the as-deposited sample.

Due to equipment limitations the  $B_{max}$  values for the near infrared transitions could not be measured. Hence instead of calculating the excitation efficiency independently, the total device efficiency for the infrared transition was estimated as a product of excitation and radiative efficiencies. Figure 5.16b monitors this product ( $Eff_{exe} * Eff_{rad}$ ) for the near infrared (1550nm) transition versus voltage for the Al (+) polarity. Annealing

improved the total efficiency ( $\text{Eff\_exe} * \text{Eff\_rad}$ ) by a factor of 8 as compared to the as-deposited sample.



(a)



(b)

Figure 5.16 Excitation efficiency, ( $B_{\max}/Q_{\text{int}}$ ) versus voltage for the a) visible transition (545nm) and b) near infrared transition (1550nm).

#### 5.4 Summary of Results

ZnS:ErF<sub>3</sub> doped thin films were deposited, annealed at temperatures ranging from 375°-425°C for 1 hr in order to investigate the effect of annealing on device properties. Duty cycles of 100% on each target operated at 120W, were found to result in the optimal Er concentration of ~ 1at% in the films and optimal infrared brightness of 0.01 and 0.02μW/cm<sup>2</sup> for the 990 and 1550nm transitions respectively. The FWHM of the 2θ diffraction peak decreased with increased annealing temperature, thereby providing evidence of improved film crystallinity. The threshold voltage for the visible and infrared emissions was found to be the same. B-V plots indicated that the threshold voltage for the annealed film was 25V smaller than that of the as-deposited film. The infrared intensity of the 990 and 1550nm emissions for the ZnS:ErF<sub>3</sub> doped thin films at 40V above threshold was observed to increase with annealing temperature up to 425°C, then decreased at higher anneal temperatures. The emission wavelengths remained constant, unlike in the case of neodymium doped samples. ZnS:ErF<sub>3</sub> doped thin films annealed at 425°C for 1 hr exhibited an optimum infrared brightness of 7.5μW/cm<sup>2</sup> for the 990nm transition and 28μW/cm<sup>2</sup> for the 1550nm transition, 650% and 2700% larger respectively than their as-deposited counterparts. Room temperature photoluminescence measurements indicated that 330nm was the optimum excitation wavelength for both the visible 545nm and the near infra-red 1550nm transitions. Time resolved luminescence decay measurements recorded a time constant of 30μs ± 5μs for the as-deposited ZnS:ErF<sub>3</sub> thin film and 40μs ± 5μs for the film annealed 425 °C for 1 hr. Electrical analysis showed that the various plots were relatively symmetrical between both the Al (+) and the Al (-) polarities. At 40V above threshold, the annealed films showed higher

external as well as internal conduction charge density ( $5.87\mu\text{C}/\text{cm}^2$  and  $6.1\mu\text{C}/\text{cm}^2$ ) versus as-deposited films ( $3.825\mu\text{C}/\text{cm}^2$  and  $3.93\mu\text{C}/\text{cm}^2$ ) respectively. The Q-V and C-V characterization also indicated lower thresholds and higher capacitances above threshold for the annealed films as compared to the as-deposited films. External as well as internal conduction charge increased with annealing. The average external charge for the annealed sample improved by a factor of 1.5 over the as-deposited sample, whereas the internal charge also improved by a factor of 1.5. Average excitation efficiency for the annealed sample improved by a factor of 8 for the near infrared transition, whereas that for the visible transition increased by a factor of 5.

## CHAPTER 6 DISCUSSIONS

Both ZnS:NdF<sub>3</sub> and ZnS:ErF<sub>3</sub> ACTFEL devices have been studied, and comparisons made between the as-deposited and annealed conditions. This chapter focuses on providing explanations for the demonstrated increase in infrared irradiance, achieved through post-deposition annealing.

As presented in chapter 4, annealing improved the ZnS:NdF<sub>3</sub> NIR irradiance over as-deposited samples. In the best case, the irradiance at V<sub>40</sub> for the 910nm and 1060nm transitions increased by a factor of 2 with annealing at 425°C for 1 hr, compared to as-deposited samples under identical conditions (Figure 4.7d). In addition to the increase in optical output, shifts in the infrared peak emission wavelengths from Nd were also observed.

In the case of ZnS:ErF<sub>3</sub> ACTFEL devices as shown in Figure 5.6c, the irradiance at V<sub>40</sub> for the 990nm and 1550nm transitions increased by a factor of 8 and 30 respectively with annealing at 425°C for 1 hr, compared to as-deposited samples. No shifts were observed in the infrared peak emission wavelengths from Er.

The primary measures of ACTFEL device performance are emission wavelength (in nm), optical output (brightness in lumens/cm<sup>2</sup> or W/cm<sup>2</sup>, or irradiance in W/cm<sup>2</sup>-nm or radiance in W/cm<sup>2</sup>) and efficiency (in W/W). The goal of this research is to relate the effects of post-deposition annealing to the improved performance of ZnS:Nd or Er. Based on the physics and electro-optical phenomena of ACTFEL devices [119, 120], several potential mechanisms for increased performance will be discussed.

## 6.1 Neodymium Fluoride (NdF<sub>3</sub>) Doped Zinc Sulfide ACTFEL Devices

### 6.1.1 Wavelength Dependence with Temperature

While it is generally true that the emission wavelengths of rare earth ions are independent of the host in which they reside [37], Figure 4.7b shows that the wavelength of the NIR peaks from ZnS:NdF<sub>3</sub> exhibited a blue, then a red shift with increasing annealing temperature. In the free ion state, molecular orbital interactions are absent and if the spin-orbit interactions are overlooked, all the f-orbitals are degenerate with respect to energy (i.e. all have the same energy). When a rare-earth ion is surrounded by a host matrix, the normal electron orbital distributions are perturbed and new energy states are created. For more covalently bonded solids (electronegativity difference between constituent ions is smaller), the electrons spread over wider orbitals and the interactions between them are reduced. As a result, transitions between energy levels may shift to lower energy for increasing covalency in the electron bonding. This effect, called the nephelauxetic effect, which literally means (electron) cloud expanding [58], has been studied by numerous authors [121-123]. Indeed, Jorgensen et al. have reported shifts in the emission wavelength of Nd doped phosphors, and attributed these shifts to the nephelauxetic effect [121]. However, substitution of an Nd ion onto a Zn site results in a larger electronegativity difference between the metal and ligand as compared to Er and Zn. In other words, the Nd-S bond is more ionic (decreasing covalency) than Zn-S or Er-S bonds. Furthermore, the Nd emission peaks (see Figure 4.7b) were observed to blue shift at low anneal temperatures, then red shift at higher anneal temperatures. Based on the nephelauxetic effect, only a red shift would be expected. Since the only host evaluated in this study for all annealing conditions was ZnS, the nephelauxetic effect cannot be the mechanism responsible for the observed peak shifts.

In addition to changes in the covalency of the bonds, hybridization of the 5d and  $4f^7$  levels resulting in  $4f^{n-1}5d-4f^n$  states for  $Nd^{+3}$  has been reported [124]. Transitions from hybridized orbitals are poorly shielded and are therefore may be influenced by local crystal fields. Local rearrangements of the lattice (and crystal fields) and position of Nd ions in the lattice due to annealing is a more likely explanation for the observed changes in spectral properties i.e., the observed peak shifts and changes in FWHM. It is suggested that this possibility could be examined in detail by x-ray absorption fine structure analysis.

### 6.1.2 Brightness and Efficiency Improvement with Annealing

In addition to shifts in the emission wavelengths observed for Nd, changes in peak wavelength intensities with annealing were very dramatic. Qualitatively, the increases in optical output can be understood in the following manner: sputtered films inherently have high defect concentrations [120, 125]. In the as-deposited condition, the films show lower electroluminescence intensity due to high electron scattering cross sections for defects, which limits the number of injected electrons that become sufficiently ‘hot’ to cause impact excitation. In addition, the large defect density in as-deposited films could provide non-radiative relaxation pathways which are faster than, and are in direct competition with, radiative relaxation. As the films are annealed, defects are eliminated, and the EL intensity could increase due to changes in a number of electro-optical phenomena described in more detail below.

For  $ZnS:NdF_3$  thin films, both the 910nm and the 1060nm emissions arise from the same excited state (the  $^4F_{3/2}$  state at  $1.1 \times 10^4 \text{ cm}^{-1}$ ). As a result the intensities of both EL peaks behave similarly versus annealing temperature, i.e. both increase in intensity for anneals up to 425°C, and both decrease for anneals at 475°C (see Fig 4.7c). In contrast as

shown by the inset in Fig. 4.7c, the Nd visible EL signal at 600nm increases dramatically as the annealing temperature is raised above 425°C. The visible emission peaks results from relaxation from the  $^4G_{5/2}$  at  $1.9 \times 10^4 \text{ cm}^{-1}$ . The intensity of the visible emission peak presumably continues to increase at higher annealing temperatures due to the reduction of defects in the film.

As mentioned earlier (section 4.2) the total device efficiency is calculated as a product of the outcoupling ( $\eta_{\text{opt}}$ ), radiative ( $\eta_{\text{rad}}$ ) and excitation efficiencies ( $\eta_{\text{exc}}$ ). The effect(s) of annealing on each of these factors will now be discussed.

#### 6.1.2.1 Outcoupling efficiency

The roughness of the as-deposited and annealed (425° for 1 hr) ZnS:NdF<sub>3</sub> thin films were measured by AFM (atomic force microscopy) as shown in Figure 4.3. The surface roughness values for the as-deposited (RMS=16) and annealed (RMS=15) films (425°C for 1 hr) were the same within experimental error. These data show that annealing does not increase surface roughness of the phosphor and suggest that the outcoupling efficiency should be constant. In order to directly quantify the outcoupling efficiency, diffuse reflectance measurements were performed. The variation in the diffuse reflectance between the as-deposited and annealed samples was ~10%, as shown in Figure 4.6 and again considered to be within experimental error. Both sets of data indicate that annealing does not improve the outcoupling efficiency upon annealing, indicating that  $\eta_{\text{opt}}$  is constant and that the increase in optical output observed with annealing is not due to increased optical outcoupling.

### 6.1.2.2 Radiative efficiency

Time resolved decay measurements for both as-deposited and annealed samples were recorded in order to evaluate the effect of annealing on radiative and excitation efficiencies. Figures 4.10 and 4.12 depict the time resolved decay behavior for the visible (600nm) transition for as-deposited and annealed samples, respectively. The time decay constants for the as-deposited samples were  $20 \pm 5\mu\text{s}$ , whereas the values for annealed samples were  $10 \pm 5\mu\text{s}$ . These values are within experimental error of one another, i.e. there is not a significant increase or decrease with annealing. Hence it is concluded that the radiative efficiency ( $\eta_{\text{rad}}$ ) is essentially constant for visible emission. Because of equipment limitations, the decay time for NIR emission peaks could not be measured. Considering that the visible and NIR emissions originate from different excited states, extrapolating the decay behavior observed in the visible to the NIR is not justified, even though it is tempting to postulate that the effects of annealing on NIR radiative efficiency are small.

### 6.1.2.3 Excitation efficiency

#### Visible emission at 600nm

As mentioned earlier (section 4.2.2), the excitation efficiency is proportional to the ratio of  $B_{\text{max}}/Q_{\text{int}}$ . The  $B_{\text{max}}$  value is obtained by extrapolating the brightness value from the luminescence decay measurements (see Figure 4.16) back to time  $(t) = 0$ . The internal charge ( $Q_{\text{int}}$ ) is the charge through the device after the onset of conduction. Figure 4.15 shows the influence of annealing on the behavior of internal conduction charge as a function of the phosphor field for the Al (+) and the Al (-) polarities. The conduction charge increases significantly with annealing at 425°C for 1 hr. Figure 4.17a compares

the  $B_{\max}/Q_{\text{int}}$  versus voltage for the visible transition (600nm) for the as-deposited and annealed sample. The excitation efficiency decreased by a factor of 3 for the annealed sample. This can be explained on the basis of Figure 4.7c, where at an annealing temperature of 425°C, the visible peak (600nm) intensity is the lowest and the infrared peak (910 and 1060nm) intensity is the highest. As stated earlier, the visible transition (600nm) results from relaxation from the  $^4G_{5/2}$  state to the ground ( $4I_{9/2}$ ) state, whereas both infrared transitions (910nm and 1060nm) originate from relaxation from the lower  $^4F_{3/2}$  state (see Figure 2.12). The optical threshold for the visible and NIR is the same, which suggests that both excited states are populated after breakdown of the phosphor. Since both the visible and IR have the same threshold voltage, changes in the radiative efficiencies must be related to de-excitation rather than excitation. Otherwise it would be expected that emission from the higher lying excited state of the 600nm emission would have a higher threshold voltage. At lower anneal temperatures, shallow traps cause a rapid decay of the population of the higher lying visible excited states by non-radiative de-excitation to the ground state as well as to the excited state of the NIR emission. The infrared excited state level then decays radiatively in an efficient manner. For anneals at 425°C, the infrared intensity is maximum and the infrared state de-excitation is at its highest rate. Annealing above 425°C results in the shallow traps causing these effects to be annealed out, resulting in a higher probability for direct radiative relaxation from the higher lying visible excited state. As a result the visible signal is observed to increase, with a subsequent decrease in the infrared signal at annealing temperatures  $>425^\circ\text{C}$ .

### Near infrared emission at 910nm

Due to the limitation and unavailability of instrumentation, luminescence time decay of the infrared transition (910nm) could not be measured. Therefore  $B_{\max}$  and hence excitation efficiency could not be determined. However the product of the excitation efficiency and the radiative efficiency ( $\eta_{\text{exc}} * \eta_{\text{rad}}$ ) can be determined. This product is equal to the total device NIR or visible optical output divided by the internal charge (Optical output/ $Q_{\text{int}}$ ). Figure 4.17b shows this product versus voltage for the near infrared (910nm) transition at  $V_{40}$  for the Al (+) polarity. Annealing at 425C improved the total efficiency by a factor of 1.5, compared to as-deposited samples. In this case, changes in either or both  $\eta_{\text{exc}}$  and  $\eta_{\text{rad}}$  may alter the total device brightness and efficiency. However, the main contributor to the improved irradiance and total device efficiency observed with annealing is proposed to be the excitation efficiency ( $\eta_{\text{exc}}$ ). This is based on the fact that a huge increase in both the external and internal conduction charge was observed with annealing. These results, summarized in Table 6.1, show that the internal charge increased by a factor of 3.3 with annealing.

Table 6.1 External and internal conduction charge versus voltage at  $V_{40}$  for as deposited and annealed ZnS:NdF<sub>3</sub> thin films.

ZnS:NdF <sub>3</sub> thin films		As deposited	Annealed 425°C
External charge ( $\mu\text{C}/\text{cm}^2$ )	Al <sup>+</sup>	1.86	5.32
	Al <sup>-</sup>	1.83	5.84
	Average	1.85	5.58
Internal charge ( $\mu\text{C}/\text{cm}^2$ )	Al <sup>+</sup>	1.77	5.81
	Al <sup>-</sup>	1.77	6.3
	Average	1.77	6

As reported in Chapter 4, the threshold voltage for the annealed samples (185V) is 45V smaller than that for the as-deposited samples (230V). This is possible due to the removal of shallow traps, which results in uncompensated positive space charge from

deep levels, and leads to enhanced band bending and reduction of defects with annealing. It is interpreted, that in the annealed films, the lower defect concentrations results in less inelastic scattering and therefore lower energy loss rates for conduction electrons, making it easier for them to attain the threshold energies for excitation at lower applied fields. The improved crystallinity with annealing, evident from the reduction in FWHM (full width half maximum) of the X-ray analysis data (see Figure 4.2) is also expected to contribute to larger average ballistic electron energies at equivalent electric fields. These factors combine to indicate that post-deposition annealing,

1. removes shallow traps, which results in uncompensated positive space charge from deep levels, and leads to enhanced band bending
2. reduces point defect concentrations and reduces inelastic scattering of ballistic electrons associated with defects
3. improves tunneling from interface states associated with 1
4. increases the amount of conduction charge resulting from 1 and 2
5. reduces the threshold voltage for a given optical output stemming from 1, and 2
6. improves optical output and/or device efficiency resulting from a combination of 1, 2, 3 and 4.

## 6.2 Erbium Fluoride (ErF<sub>3</sub>) Doped Zinc Sulfide ACTFEL Devices

### 6.2.1 Wavelength Independence of Temperature

In contrast to Nd, the peak wavelength positions for ZnS:ErF<sub>3</sub> thin films remain constant with varying annealing temperatures (see Fig 5.5a). It is concluded that for Er, the transitions related to emission are intraband 4f-4f transitions. Such transitions are well shielded from local fields by the 5s, 5p, 6s and 5d orbitals.

### 6.2.2 Brightness and Efficiency Improvement with Annealing

In addition to the increase in intensity, the 1550nm and 990nm emissions from Er behaved differently with increasing temperature. Both the 1550 nm and 990 nm peak

intensities first increased up to a temperature of 425°C, then the 1550 nm peak decreased at higher anneal temperatures while the 990 nm peak remained constant for a 475°C anneal. The 1550nm emission originates from a lower lying excited state (the  $^4I_{13/2}$  state at  $[7 \times 10^3] \text{cm}^{-1}$ ) while the 990nm emission originates from a higher energy excited state (the  $^4F_{7/2}$  state at  $[21 \times 10^3] \text{cm}^{-1}$ ). As for ZnS:Nd, the threshold voltages for the ZnS:Er visible and infrared transitions were the same. The lower energy level  $^4I_{13/2}$  state decays more efficiently than the higher energy  $^4F_{7/2}$  state, leading to relatively stronger emission at 1550 nm for films with  $T_{\text{anneal}} < 425^\circ\text{C}$  (see Fig 5b). In this case too, the same de-excitation argument holds as stated in section (6.1.2.3), i.e. at lower anneal temperatures, shallow traps rob the emission associated with higher lying excited states, whereas at higher anneal temperatures ( $>425^\circ\text{C}$ ), these states decay more effectively due to annealing out of shallow traps and reduced defect densities. Above 425°C, the concentration of defects have been substantially reduced according to the FWHM XRD data and internal charge increase, leading to better direct relaxation of the 990nm excited state to the ground level. This results in reduced non-radiative relaxation from higher excited states to the  $^4I_{13/2}$  excited state of the 1550nm emission. As a result the intensity of the 1550nm emission decreases at annealing temperatures  $>425^\circ\text{C}$ .

#### 6.2.2.1 Outcoupling efficiency

As discussed above (section 4.2.2), the total device efficiency is a product of outcoupling ( $\eta_{\text{opt}}$ ), radiative ( $\eta_{\text{rad}}$ ) and excitation efficiencies ( $\eta_{\text{exc}}$ ). As discussed in section 4.2.1, the two major factors that affect the outcoupling efficiency are index of refraction and surface roughness. AFM did not reveal a significant difference in surface roughness between the as-deposited and annealed films (see Figure 5.3). Likewise, the

diffuse reflectance of both sets of samples was essentially the same (see Figure 5.5).

Thus, it is concluded that the increase in optical output observed with annealing of ZnS:Er films is not due to increased optical outcoupling.

#### 6.2.2.2 Radiative efficiency

Time resolved luminescence decay studies were performed, as in the case of ZnS:Nd. Figure 5.16a shows plots of  $B_{\max}/Q_{\text{int}}$  versus voltage Based on the visible (545nm) transition. It is observed that the time decay constants for the as-deposited ( $30 \pm 5\mu\text{s}$ ) and the annealed samples ( $40 \pm 5\mu\text{s}$ ) are essentially constant and do not show an increase or decrease within experimental error. Thus it is concluded that the radiative efficiency remained constant and is not responsible for the increase in the total device brightness and efficiency observed with annealing.

#### 6.2.2.3 Excitation efficiency

##### Visible emission at 525nm

The excitation efficiency for the visible transition increased by a factor of 5 for the annealed sample compared to the as-deposited sample (see Figure 5.16a). In the case of erbium, the visible and infrared emission intensities follow the same trend. The optical threshold for the visible and NIR is the same which suggests that the main factor in the threshold for luminescence is breakdown of the phosphor. Since both the visible and IR have the same turn-on, the changes in intensity seems to be related to de-excitation rather than excitation.

### Near infrared emission at 1550nm

The limitations for measuring the excitation efficiency of the infrared transitions from ZnS:Er are the same as described above for ZnS:Nd. Again, the total device efficiency will be equilibrated to the product of the excitation efficiency and the radiative efficiency ( $\eta_{exc} * \eta_{rad}$ ) versus voltage. Figure 5.16b shows a plot of  $\eta_{exc} * \eta_{rad}$  versus voltage for the infrared transition (1550nm). Annealing improved this product by a factor of 8 compared to the as-deposited sample. While the visible luminescence behavior cannot be directly extrapolated to the IR because the excited states are different, the assumption that  $\eta_{rad}$  for the 1550 nm transition is not significantly affected by annealing is a reasonable one. Thus, it is proposed that the main factor responsible for device irradiance and efficiency improvements is the excitation efficiency ( $\eta_{exc}$ ). This is also reasonable based on the fact that significant increases in the internal conduction charge ( $Q_{int}$ ) are observed with annealing, as shown in Figures 5.15. These results, summarized in Table 6.2, show that both the average external and internal charges increased by factors of 1.5 with annealing. It is concluded that this is the major factor contributing to improved device NIR intensity and efficiency.

Table 6.2 External and internal conduction charge versus voltage at  $V_{40}$  for as deposited and annealed ZnS:ErF<sub>3</sub> thin films.

(ZnS:ErF <sub>3</sub> )		As deposited	Annealed 425°C
External charge ( $\mu\text{C}/\text{cm}^2$ )	Al <sup>+</sup>	3.84	6.14
	Al <sup>-</sup>	3.81	5.6
	Average	3.825	5.87
Internal charge ( $\mu\text{C}/\text{cm}^2$ )	Al <sup>+</sup>	3.86	6.2
	Al <sup>-</sup>	4	6
	Average	3.93	6.1

The threshold voltage for the annealed sample (160V) was observed to be smaller than that for the as-deposited sample (185V). This is represented in terms of the phosphor

field data as shown in Figure 5.15, and is attributed to the removal of shallow traps, which results in uncompensated positive space charge from deep levels, and leads to enhanced band bending and reduction of defects with annealing. The conduction electrons lose less energy to inelastic scattering events and are therefore able to attain the required threshold energies at lower applied fields. It is proposed that the observed decrease in the FWHM (see Figure 5.2) is due to improved crystallinity which also enhances high-field transport. Thus, similar to ZnS:NdF<sub>3</sub> devices, the experimental data suggest that improved electro-optical performance of annealed ZnS:ErF<sub>3</sub> is due to,

1. removal of shallow traps, which results in uncompensated positive space charge from deep levels, and leads to enhanced band bending
2. reduction in point defect concentrations and reduction of inelastic scattering of ballistic electrons associated with defects
3. improvement in tunneling from interface states associated with 1
4. increase in the amount of conduction charge [facilitated by reduced inelastic scattering]
5. reduction of the threshold voltage for a given optical output stemming from 1, and 2
6. improvement in the optical output and/or device efficiency resulting from a combination of 1, 2, 3 and 4.

## CHAPTER 7 CONCLUSIONS

ZnS:NdF<sub>3</sub> and ZnS:ErF<sub>3</sub> alternating current thin film electroluminescent (ACTFEL) devices were fabricated using RF plasma magnetron sputtering and deposited from an undoped ZnS target operated simultaneously with a ZnS:NdF<sub>3</sub> or ErF<sub>3</sub> target. The effects of post-deposition annealing on ZnS:NdF<sub>3</sub> and ZnS:ErF<sub>3</sub> ACTFEL devices were shown to improve near infrared (NIR) electroluminescence (EL) irradiance and total device efficiency.

For ZnS:NdF<sub>3</sub> thin films, an optimum concentration of 0.9at% Nd<sup>3+</sup>, resulted in a maximum infra-red power densities of 26 and 15μW/cm<sup>2</sup> at 910nm and 1060nm, respectively, after annealing at 425°C for one hour, an increase of 2 (100%) times over as-deposited films. Post-deposition annealing also increased the total device efficiency by 50%, from 0.47 to 0.7 W/W. The threshold voltage for luminescence from annealed samples (185V) is 45V smaller than that for the as-deposited samples (230V) due to annealing of shallow traps, which results in uncompensated positive space charge from deep levels, and enhanced band bending. It is postulated that the lower defect concentrations in annealed films also results in less inelastic scattering and therefore lower energy loss rates for conduction electrons, allowing them to be accelerated to the threshold energies for luminescence with lower applied fields. The increased device radiance and total device efficiency by annealing is attributed to a larger effective phosphor field, an increase in the conduction charge, and a reduction of inelastic scattering of ballistic electrons. The infrared peak EL intensities (910nm and 1060nm)

from ZnS:NdF<sub>3</sub> increased with annealing temperatures up to 425°C, then decreased at higher anneal temperatures. To the contrary, the visible intensity was the lowest after 425°C, and increases with higher annealing temperatures. The luminescent threshold voltage was the same for visible and infrared transitions, a de-excitation scheme is postulated, in which electrons in excited states that normally lead to visible luminescence decay non-radiatively into shallow traps and ultimately into the excited states that lead to NIR luminescence. For anneals above 425°C, these shallow traps are removed, leading increased visible luminescence. Both red and blue shifts in the infrared EL wavelengths from ZnS:NdF<sub>3</sub> were observed with annealing temperature, and was attributed to changes in hybridization of the 5d-4f orbitals during local rearrangements of the lattice (and crystal fields) due to annealing.

For ZnS:ErF<sub>3</sub> thin films, an optimal concentration of ~ 1at% Er<sup>3+</sup> achieved optimal infrared radiance of 7.5μW/cm<sup>2</sup> at 990nm and 28μW/cm<sup>2</sup> at 1550nm. These values were 7.5 (750%) and 28 (2800%) times larger than those of the as-deposited films, which exhibited a power density ~1μW/cm<sup>2</sup> at both respective wavelengths. In addition, a 740% increase in the total device efficiency was also achieved from 0.05 to 0.42 W/W. As for Nd, the threshold voltage for the annealed Er sample (160V) was smaller than that for the as-deposited sample (185V). This is again attributed to annealing of shallow traps, resulting in uncompensated positive space charge from deep levels, and enhanced band bending. The conduction electrons lose less energy to inelastic scattering and therefore attain the required luminescence threshold energies at lower applied fields. Improved device intensity and total device efficiency were thus attributed to a reduction in shallow traps and increased conduction charge. The infrared EL output was observed to increase

with annealing temperature up to 425°C, then decreased at higher anneal temperatures. A similar de-excitation mechanism as in the case of neodymium was proposed to explain this effect. The emission wavelengths remained constant, suggesting that emission is from intraband 4f-4f transitions that are well shielded from local fields by the 5s,5p, 6s and 5d orbitals.

## LIST OF REFERENCES

1. Kobayashi, H. and S. Tanaka, The present and future prospects of electroluminescent phosphors, J. SID, 1996. 4(3): p. 157-163.
2. Mauch, R.H., The current status of thin-film electroluminescence, J. SID, 1997. 5(3): p. 173-178.
3. Rack, P.D., A. Naman, P. H. Holloway, S. S. Sun and R. T. Tuenge, MRS Bulletin, 1996. 21(3): p. 49-58.
4. Ono, Y.A., Annual Reviews Materials Science, 1997. 27: p. 283-303.
5. King, C.N., Electroluminescence: an industry perspective, J. SID, 1996. 4(3): p. 153-156.
6. Mach, R. and G.O. Mueller, Semiconductor Science and Technology, 1991. 6: p. 305-323.
7. Anderson, M.T., R.J. Walko, and M.L.F. Phillips, Mat. Res. Soc. Symp. Ser, 1995. 345: p. 269.
8. Leskela, M., Journal of Alloys and Compounds, 1998. 277: p. 702-708.
9. Tornqvist, R., Acta Polytechn. Scand., Ser. Applied Physics, 1990. 170: p. 1.
10. King, C.N., J. Soc. Inf. Disp, 1992. 1: p. 1.
11. Ono, Y.A., *Electroluminescent Displays*, 1995, Singapore: World Scientific Publishing Co.
12. Tannas, L.E., *Flat-Panel Displays and CRT's*, 1985, New York: Van Nostrand Reinhold. 468.
13. Rack, P.D. and P.H. Holloway, Materials Science and Engineering, 1998. R21(4): p. 171-219.
14. Gudden, B. and R. Pohl, Z. Phys., 1920. 2: p. 192.
15. Destriau, G., J. Chim. Phys., 1936. 33: p. 587.
16. Vecht, A., Journal of Applied Physics, 1968. 1: p. 134.

17. Kahng, D., *Applied Physics Letters*, 1968. 13: p. 210.
18. Soxman, E.J. and R.D. Ketchpel, *Electroluminescence Thin Film Research Reports*, JANAIR Report 720903, 1972.
19. Russ, M.J. and D.I. Kennedy, *Journal of the Electrochemical Society*, 1967: p. 1066.
20. Inoguchi, T., M. Takeda, Y. Kakihara, Y. Nakata and M. Yoshida, *SID Digest*, 1974: p. 84-95.
21. Uede, H., Y. Kanatani, H. Kishishita, A. Fujimori and K. Okano, *SID Digest*, 1981: p. 28.
22. Takeda, M., Kanatani, H. Kishishita, T. Inoguchi and K. Okano, *SID Digest*, 1980: p. 66.
23. Takeda, M., Y. Kanatani, H. Kishishita, T. Inoguchi and K. Okano, *SID proceedings*, 1981. 57: p. 22.
24. S. Mito, C. Suzuki, Y. Kanatani and M. Ise, *SID 74 Digest International Symposium*, 1974: p. 86-87.
25. Jayaraj, M.K. and C.P.G. Vallabhan, *J. Electrochem. Soc.*, 1991. 138(5): p. 1512-1516.
26. Kobayashi, H., S. Tanaka, V. Shanker, M. Shiiki, T. Kunou, J. Mita and H. Sasakura, *Physica Status Solidi A-Applied Research*, 1985. 88(2): p. 713-720.
27. Pomrenke, G.S., P.B. Klein, and D.W. Lange, eds., *Mater. Res. Soc. Symp. Proc.* Vol. 301. 1993, Pittsburgh: MRS.
28. Coffa, S., A. Polman, and R.N. Schwartz, eds., *Mater. Res. Symp. Proc.*, Vol. 422. 1996: Pittsburgh: MRS.
29. Zavada, J.M. and D. Zhang, *Solid-State Electron.*, 1995. 38: p. 1285.
30. Chase, E.W., R. T. Hepplewhite, D. C. Krupka and D. Kahng, *Journal of Applied Physics*, 1969. 40(6): p. 2512-2519.
31. Godlewski, M. and M. Leskela, *Crit. Rev. Solid State Mater. Sci*, 1994. 19: p. 199.
32. Tornqvist, R., *SID 97 Digest*, 1997. 28: p. 855.
33. Harkonen, G., M. Leppanen, E. Soininen, R. Tornqvist and J. Viljanen, *Journal of Alloys and Compounds*, 1995. 225(1-2): p. 552-554.
34. King, C.N., *Journal of Vacuum Science and Technology A*, 1996. 14: p. 1729.

35. Barrow, W.A., R. C. Coover, E. Dickey, C. N. King, C. Laakso, S. S. Sun and R. T. Tuenge, SID 93 Digest, 1993: p. 761.
36. Weldon, V., J. Ogorman, J. J. PerezCamacho, M. McDonald, J. Hegarty, J. C. Connolly, N. A. Morris, R. U. Martinelli and J. H. Abeles, *Infrared Physics & Technology*, 1997. 38(6): p. 325-329.
37. Ronda, C.R., T. Justel, and H. Nikol, *Journal of Alloys and Compounds*, 1998. 277: p. 669-676.
38. Silveira, J.P. and F. Grasdepot, *Infrared Physics & Technology*, 1996. 37(1): p. 143-147.
39. Perdrotti, F.L., S.J. Leno, and S. Perdrotti, *Introduction to Optics*, 2<sup>nd</sup> ed., 1987, Englewood Cliffs, NJ: Prentice-Hall.
40. Haaranen, J., R. Tornqvist, J. Koponen, T. Pitanen, M. Surma-aho, W. Barrow and C. Laakso, SID 92 Digest, 1992. 23: p. 348.
41. Khormanei, R., S. Thayer, K. Ping, G. Dolney, A. Ipri, F. L. Hsueh, R. Stewart, T. Keyser, G. Becker, D. Kagey and M. Spitzer, SID 94 Digest, 1994. 25: p. 137.
42. Wu, X., EL, 1996. 96: p. 285.
43. Minami, T., *Display and Imaging*, 1999. 8, suppl.: p. 83-93.
44. Aguilera, M., B. Atchinson, D. Basham, S. Moehnke, K. Ping, Digest of the 1996 SID International Symposium, 1996: p. 125.
45. King, C.N., EL, 1996. 96: p. 375.
46. Wager, J.F. and P.D. Keir, *Ann. Rev. Mater. Sci.*, 1997. 27: p. 223-248.
47. Kobayashi, H., R. Tueta, and R. Menn, *IEEE Trans Electron Devices*, 1982. ED-29(10): p. 1626-1630.
48. Ohwaki, J., H. Kozawaguchi, and B. Tsujiyama, *Journal of the Electrochemical Society*, 1990. 137: p. 340.
49. Bringuier, E., *J. Appl. Phys.*, 1994. 75(9): p. 4291-4312.
50. Okamoto, S., E. Nakazawa, and Y. Tsuchiya, *Japanese Journal of Applied Physics Part 1-Regular Papers Short Notes & Review Papers*, 1989. 28(3): p. 406-409.
51. Sze, S.M., *Physics of Semiconductor Devices*, 2<sup>nd</sup> ed., 1981, New York: Wiley-Interscience.
52. Kittel, C., *Introduction to Solid State Physics*, 6<sup>th</sup> ed., 1986, New York: John Wiley and Sons, Inc.

53. Brennan, K., J. Appl. Phys., 1988. 64(8): p. 4024-4030.
54. Mach, R. and G.O. Mueller, Journal of Crystal Growth, 1990. 101: p. 967-975.
55. Bhattacharyya, K., S.M. Goodnick, and J.F. Wager, J. Appl. Phys., 1993. 73(7): p. 3390-3395.
56. Bringuier, E., J. Appl. Phys., 1991. 70(8): p. 4505-4512.
57. Baraff, G.A., Phys. Rev., 1962. 128(6): p. 2507-2517.
58. Blasse, G. and B.C. Grabmaier, *Luminescent materials*, 1994, Berlin: Springer-Verlag.
59. Mach, R. and G.O. Mueller, Physica Status Solidi (a), 1984. 81: p. 609-623.
60. Holloway, P.H. and S.L. Jones, Journal of Surface Anal., 1998. 3(2): p. 226-231.
61. Stevens, H. 2000, Dow Corning, Inc.
62. Keir, P.D., *Fabrication and characterization of ACTFEL devices*, Masters thesis, 1999, Oregon State University: Corvallis. p. 280.
63. Prazision Glass & Optics, [www.pgo-online.com](http://www.pgo-online.com), retrieved October 2003.
64. Kim, H. and C.M. Gilmore, J Appl Phys, 1999. 86(11): p. 6451-6461.
65. Honda, S., A. Tsujimoto, M. Watamori and K. Oura, J Vac Sci Tech A, 1995. 13(3): p. 1100-1103.
66. Suzuki, M., Y. Maeda, M. Muraoka, S. Higuchi and Y. Sawada, Mater Sci Eng B, 1998. 54: p. 43-45.
67. Jia, Q.X., J. P. Zheng, H. S. Kwok and W. A. Anderson, Thin Solid Films, 1995. 258: p. 260-263.
68. Kamei, M., Y. Shigesato, I. Yasui, N. Taga and S. Takaki, J Non-Crystalline Solids, 1997. 218: p. 267-272.
69. Laux, S., N. Kaiser, A. Zoller, R. Gotzelmann, H. Lauth and H. Bernitzki, Thin Solid Films, 1998. 335: p. 1-5.
70. Tominaga, K., T. Ueda, T. Ao, M. Kataoka and I. Mori, Thin Solid Films, 1996. 281-282: p. 194-197.
71. Utsumi, K., O. Matsunaga, and T. Takahata, Thin Solid Films, 1998. 334: p. 30-34.
72. Aduodija, F., H. Izumi, T. Ishihara and H. Yoshioka, Appl Phys Lett, 1999. 74(20): p. 3059-3061.

73. Paine, D.C., T. Whitson, D. Janiac, R. Beresford and C. Ow Yang, *J Appl Phys*, 1999. 85(12): p. 8445-8450.
74. Chopra, K.L., S. Major, and D.K. Pandya, *Thin Solid Films*, 1983. 102: p. 1.
75. Alt, P.M., *SID Digest*, 1984. 79.
76. Ono, Y., *Encyclopedia of Applied Physics*. ed. G.L. Trigg. 1993, New York, VCH publishers.
77. Ono, Y., *SID Seminar lecture notes, Volume II, F-1, F-1/1*, 1993.
78. Ono, Y. *Progress in information display technology*, ed. S. Kobayashi. Vol. 1. 1995, Singapore: World Scientific Publishing Co.
79. Howard, W.E., *IEEE Transactions on Electron Devices*, 1977. ED-24: p. 903.
80. Tiku, S.K. and G.C. Smith, *IEEE Transactions on Electron Devices*, 1984. ED-31.
81. Tanaka, S., V. Shanker, M. Shiiki, H. Deguchi and H. Kobayashi, *SID Digest*, 1985: p. 218.
82. Pickering, H.S., *The covalent bond*. 1978, London: Wykeham Publications Ltd.
83. Kale, A., N. Shepherd, D. DeVito, W. Glass, M. Davidson Paul H. Holloway, *Journal of Applied Physics*, 2003. 94(6): p. 3147-3152.
84. Wachtler, M., A. Speghini, K. Gatterer, H. P. Fritzer, D. Ajo and M. Bettilenni, *Journal of the American Ceramic Society*, 1998. 81(8): p. 2045-2052.
85. Georgobiani, A.N., A. N. Gruzintsev, C. Barthou, P. Benalloul, J. Benoit, B. G. Tagiev, O. B. Tagiev and R. D. Zhabborov, *Journal of the Electrochemical Society*, 2001. 148(11): p. H167-H170.
86. Ballato, J., J.S. Lewis, and P. Holloway, *MRS Bulletin*, 1999. 24(9): p. 51-56.
87. Ylilammi, M., *Acta Polytech. Scand. Appl. Phys. Ser.*, 1990. 170: p. 149-152.
88. Zeinert, A., P. Benalloul, J. Benoit, C. Barthou, J. Dreyhsig and H.E. Gumlich, *Journal of Applied Physics*, 1992. 71(6): p. 2855-2862.
89. Bringuier, E. and K. Bhattacharyya, *Semicond. Sci. Technol.*, 1995. 10: p. 1065-1075.
90. Lide, D.R. and H.P.R. Frederikse, eds. *CRC Handbook of chemistry and physics*. 78th ed., 1997, Boca Raton: CRC Press.
91. Sun, S.-S., E. Dickey, J. Kane and Y. N. Yocum, *International Display Research Conference*. 1997.

92. Troppenz, U., B. Huttli, U. Storz, P. Kratzert, K. O. Welthaus, S. S. Sun and R. T. Tuenge, *Photoluminescence and electroluminescence studies on Cu and Ag doped SrS ACTFEL devices*. Extended Abstracts of the Fourth Intl Conf on the Sci and Tech of Display Phosphors / the Ninth Intl Workshop on Inorg and Org Electroluminescence, 1998: p. 187-190.
93. Chen, Y.S. and D.C. Krupka, *Journal of Applied Physics*, 1972. 43: p. 4089-4096.
94. Smith, D.H., *J. Lumin.*, 1981. 23: p. 209-235.
95. Ono, Y.A., H. Kawakami, M. Fuyama and K. Onisawa, *Japanese Journal of Applied Physics*, 1987. 26: p. 1482-1492.
96. Myers, R. and J.F. Wager, *J. Appl. Phys.*, 1997. 81(1): p. 506-510.
97. Shih, S., P. D. Keir, J. Hitt and J. F. Wager, *Appl. Phys. Lett.*, 1996. 69(13): p. 1921-1923.
98. Douglas, A.A. and J.F. Wager, *SID Digest*, 1992. 91: p. 356-359.
99. Shih, S., P. D. Keir, J. F. Wager and J. Viljanen, *J. Appl. Phys.*, 1995. 78(9): p. 5775-5781.
100. McArthur, R.C., J. D. Davidson, I. Khormaei, J. F. Wager and C. N. King, *Applied Physics Letters*, 1990. 56: p. 1889-1891.
101. Davidson, J.D., I. Khormaei, J. F. Wager, C. N. King and R. Williams, *IEEE Trans Electron Devices*, 1992. ED-39: p. 1112-1128.
102. Keir, P.D., C. Maddix, B. A. Baukol, J. F. Wager, B. L. Clark and D. A. Keszler, *Journal of Applied Physics*, 1999. 86(12): p. 6810-6815.
103. Hummel, R., *Electronic properties of materials*. 3<sup>rd</sup> ed. 2001, New York: Springer.
104. Favennec, P.N., H. L'Haridon, M. Salvi, D. Moutonnet and Y. Le Guilou, *Electron. Lett.*, 1989. 25: p. 718.
105. Neuhalfen, A.J. and B.W. Wessels, *Appl. Phys. Lett.*, 1992. 60: p. 2657.
106. Choyke, W.J., R. P. Devaty, L. I. Clemen, M. Yoganathan, G. Pensl and Ch. Hassler, *Appl. Phys. Lett.*, 1994. 65: p. 1668.
107. Mears, P.J., L. Reekie, I. M. Jauncey and D. N. Payne, *Electron. Lett*, 1987. 23: p. 1026-1028.
108. Desurvire, E., *Scientific American*, 1992. 266: p. 96.
109. Glass, A.M., *Physics Today*, 1993. 46: p. 34.

110. Hoven, G.N.v.d., E. Snoeks, A. Polman, C. van Dam, J. W. M.. van Uffelen and M. K. Smith, *Journal of Applied Physics*, 1995. 79(3): p. 1258-1266.
111. Polman, A., *Appl. Phys. Rev*, 1997. 82: p. 1.
112. Brundle, C.R., J. C.A. Evans, and S. Wilson, *Encyclopedia of materials characterization*. Materials Characterization Series, ed. J. C.A. Evans. 1992, Boston: Butterworth-Heinemann.
113. Cullity, B.D., *Elements of x-ray diffraction*. 1978, Reading: Addison-Wesley.
114. Castaing, R., *Application of electron probes to local chemical and crystallographic analysis, Ph.D thesis*. 1951, University of Paris.
115. Goldstein, J.I., D. Newbury, P. Kchlin, D. C. Joy, C. E. Lyman, E. Lifshin, L. Sawyer, J. R. Michael and M. Staniforth, *Scanning Electron Microscopy and X-ray Microanalysis*. 1981, New York: Plenum.
116. Newbury, D.E., P. Kchlin, D. C. Joy, C. E. Fiori and J. I. Goldstein, *Advanced scanning electron microscopy and x-ray microanalysis*. 1986, New York: Plenum.
117. Zeinert, A., P. Benalloul, J. Benoit, C. Barthou, J. Dreyhsig and H.E. Gumlich, *Journal of Crystal Growth*, 1992. 117: p. 1016-1020.
118. Blackmore, J.M. and A.G. Cullis, *Thin Solid Films*, 1991. 199: p. 321.
119. Zhai, Q., *Effects of Co-Dopants on the Microstructure and Electroluminescence of ZnS:Mn Thin Film Phosphors, PhD.Thesis*, 1999, University of Florida: Gainesville.
120. Waldrip, K.E., M.R. Davidson, J.H. Lee, B. Pathangey, M. Puga-Lambers, K.S. Jones, P.H. Holloway, S.S. Sun and C.N. King, *Display and Imaging*, 1999. 8, suppl.: p. 73-82.
121. Jorgensen, C.K., *Progress Inorg. Chem*, 1962. 4: p. 73.
122. Jorgensen, C.K., R. Pappalardo, and E. Ritterhaus, *Z. für Naturforsch*, 1964. 19A: p. 424.
123. Jorgensen, C.K., R. Pappalardo, and J. Flahaut, *J. Chimie Phys*, 1965. 62: p. 444.
124. Moncorge, R., L.D. Merkle, and B. Zandi, *MRS Bulletin*, 1999. 24(9): p. 21.
125. Ohring, M.C., *The materials science of thin films*. 2002, San Diego: Academic Press.

## BIOGRAPHICAL SKETCH

Ajay Kale was born in Pune, India, on October 14, 1975, and grew up there. In June, 1993, he was admitted to the Department of Metallurgy in College of Engineering Pune at the University of Pune and received his bachelor's degree in June 1997.

After receiving his bachelor's degree, he received admission to the University of Central Florida in the Department of Mechanical, Aerospace and Materials Engineering in August 1997. He worked as a graduate research assistant with Dr. Sudipta Seal on the physical and chemical studies of novel magnetron sputtered nanocrystalline  $Ti_3Al$ ,  $TiAl$ ,  $TiAl_3$  and  $Ti-Al-N$  thin films and was awarded his master's degree in materials science and engineering in July 1999.

In August 1999 he was admitted to the University of Florida, Department of Materials Science and Engineering. In the summer of 2000, he joined Dr. Paul Holloway's research group and worked on the development of near infrared alternating current thin film electroluminescent (ACTFEL) phosphors. He received his Ph.D. from the Department of Materials Science and Engineering at the University of Florida under the advisement of Dr. Paul H. Holloway in December 2003.

Mr. Kale was awarded the "Austin L. Grogan Memorial Scholarship," for best student performance in Materials Science at UCF in 1998-99. In 2003, he also received a graduate research award from the American Vacuum Society.